UNIVERSITÀ POLITECNICA DELLE MARCHE

FACOLTÀ DI INGEGNERIA

Dipartimento di Ingegneria dell'Informazione

Master's degree in BIOMEDICAL ENGINEERING

Interaction between wearable devices and human tissues: electromagnetic characterization of a real heart rate monitor using high-resolution body models and FDTD technique

Supervisor:
Prof. Franco MOGLIE

Author:
Greta SILLA

Co-supervisor:
Prof. Valter MARIANI PRIMIANI

Academic year: 2020-2021

INDEX

Abstract

In the last decade, the market of wearable devices assists a rapid growth in daily activity, mainly due to the development of new technologies like smartwatches or smart glasses useful to monitor several physiological parameters. A specific type of wearables is the Heart Rate Monitor (HRM), a personal monitoring device that allows to measure and display in real-time heart rate. As external sources, these devices require the transmitting and receiving of electromagnetic waves near the body, which, at high enough exposure levels, may damage proximate tissues. The Specific Absorption Rate (SAR) is the quantity commonly used to evaluate exposure levels, used to verify if their exposure-induced biological effects are within the safety standard regulations.

For this reason, the purpose of this study is the characterization, through Finite-different Time-Domain (FDTD) simulation, of the electromagnetic interaction between a real heart rate monitor and human tissues. The use of the FDTD method allows to simulate the field distribution generated by the device's antenna and to determine the dissipated power on the high-resolution body model. In order to achieve this goal a real device has been simulated in the 3D space and its interaction has been visualized in terms of generated field magnitude and power distribution.

As reported in the results, the antenna generates a hot spot of the electric field in the feeding point of the monopole, and the power dissipates reaching not so high depth in the body. The tissues that absorbed the majority of the power are the skin, the muscle and subcutaneous fat, even if this quantity is a portion of non-reflected power, lowered by the dispersive material present in the device. Another aspect that emerged is the fact that the electric field and the distributed power are sensitive to the distance from the tissues and the difference in body masses, which suggests the need for statistical analysis to fully evaluate the exposure condition due to the device.

In conclusion, the field distribution and SAR values obtained through FDTD simulations are plausible and could be used to quantify the electromagnetic interaction of the real device under study.
Further studies could consider various exposure configurations, due to the strong dependence of the field distribution on the posture.

1. Introduction

1.1 Biotelemetry

The word telemetry is derived from the Greek words “tele” = “remote”, and “metron” = “measure”, and means data measurements made at a distance. In other words, it is the in-situ collection of measurements or other data at remote points, and further transmitted remotely to a receiving station for monitoring.

Biomedical telemetry refers to the application of telemetry in biology, medicine, and other health care to remotely monitor various vital signs and to permits the measurement of physiological signals at distance [1]. The principal purpose of biomedical telemetry is to take advantage of the recent advances in wired and wireless communication technologies and of the recent improvements in electronics and communications in order to develop a new generation of medical devices with incorporated biomedical telemetry functionalities.

Both commonly involve wireless data transfer mechanisms (e.g., using radio, ultrasonic, or infrared systems), it also incorporates data transferred over other media such as a telephone (mobile-Health, mHealth) or the Internet (electronic Health, eHealth), optical link, or other wired communications like power line carriers.

A typical biotelemetry system comprises:

- Sensors appropriate for the particular signals to be monitored
- Battery-powered, Patient worn transmitters
- A Radio Antenna and Receiver
- A display unit capable of concurrently presenting information from multiple patients

There exist three categories of medical devices, according to their location on or inside the patient’s body (Figure 1):

- *Wearable devices* can be worn by the patient as an accessory or embedded into clothing with the help of textile and flexible technologies. They can be used to monitor several physiological parameters (e.g., glucose or cardiac events), assist the movement of artificial limbs, and work as receivers for the collection and retransmission of various vital signals.
- *Implantable devices* can be implanted inside the patient’s human body by means of a surgical operation. Example of these kind of applications are heart rate control, artificial retina, cardiac

pacemakers, cochlear implants, hypertension monitoring, functional electrical stimulation, and intracranial pressure monitoring.

- *Ingestible devices* are integrated into capsules or pills and can be swallowed by the patient. Main focus is on their use for gastrointestinal track and drug use monitoring.

Since medical devices are used on human beings, with at least a theoretical potential for harmful side effects, the public needs to be convinced of their safety and for this reason they must meet the criteria established by government-operated regulations before they can be designated as medical devices and enter the market. People's perception of electromagnetic radiation is generally fearful and safety standards need to be established in order to quantify biological damages and preserve patient safety. The Specific Absorption Rate (SAR), which is defined as the rate of energy deposited per unit mass of tissue, is generally accepted as the most appropriate dosimetric measure and device manufacturers do not introduce higher SAR values than the specified limits in order to be use by the customer [2].
Biomedical telemetry has a particular application in telemedicine which refers to the use of information and communication technologies (ICTs) for the exchange of medical information (images, data, audio, etc.) between remote locations which are located far away from each other.
Telemedicine is characterized by a rapidly growing use of wireless technologies, giving a significant boost in the provision and improvement of health care services. The development of advanced ICTs allows the integration of biomedical telemetry with telemedicine, thus enabling the perfusion of biomedical telemetry into the entire health care supply network [1].
Biomedical telemetry data sensed by the medical device are obtained at the exterior monitoring or control unit and further forwarded to a remote patient care centre for decoding, storage, and analysis. The proliferation of smart devices, capable of high-quality video transmission, open up the possibility of delivering remote healthcare to patients in their homes, workplaces or assisted living facilities as an alternative to in-person visits for both primary and specialty care [1].

Figure 1: *Smartwatch heart rate monitor (left), Cardiac Resynchronization Therapy Defibrillators (CRT-D) for the management of heart failure (centre), ingestible medical devices (right)* [3].

1.1.1 Wearable device

Wearable technology, wearables, fashion technology, smart wear, tech togs, streetwear tech, skin electronics or fashion electronics are smart electronic devices (electronic device with micro-controllers) that are worn close to and/or on the surface of the skin, where they detect, analyse, and transmit information concerning body signals - such as vital signs - and/or ambient data and which allow in some cases immediate biofeedback to the wearer [4] .
Wearable technology has several applications that grows as the field expands:

- Wearable devices appear as *consumer electronics* with the increase of the smartwatches and activity tracker demand. They can collect biometric data such as the heart rate (ECG and HRV), muscle bio-signals (EMG) from human body to provide valuable information in the field of healthcare and wellness [5].
- Another field of application is as *monitoring systems* for assisted living and eldercare. Wearable sensors or smart wearables have a huge potential in generating big data, with a great applicability to biomedicine and ambient assisted living since they independently connect to the internet [6].
- Wearable technology can be incorporated into *navigation systems*.

While wearables can collect data in aggregate form, most of them are limited in their ability to analyse or make conclusions based on this data; thus, most are used primarily for general health information. Wearables can account for individual differences, although most just collect data which are transferred to connected devices where one-size-fits-all algorithms are applied with an eventually biofeedback notification.
The advantages of these wearable devices are that they are convenient to use, and various parameters are measured noninvasively. In addition, they allow the users to monitor their daily physical activities in a free-living environment instead of controlled laboratory settings, thanks to the short-range wireless system, such as Bluetooth or local Wi-Fi setups [7].
The number and availability of consumer wearable technologies for evaluating physical and psychological health, training emotional awareness, monitoring sleep quality, and assessing cognitive function has recently increased [8].
They are designed to be wear on a variety of body parts -such as wrist, waist, hands, fingers, legs - or incorporated on smart clothing, ranging from shirts, shorts, headbands to socks, but are commonly categorized by the parts on which must be worn (Figure 2) [9] [10].

Figure 2: *Summary of current technologies for monitoring health/performance and targeted physical measurements* [8].

1.1.2 Heart rate monitors

The Heart Rate Monitor (HRM) is a personal monitoring device that allows to measure/display heart rate in real-time or to record the heart rate for later study. It is largely used to gather heart rate data while performing various types of physical exercise. Measuring electrical heart information is referred to as Electrocardiography (ECG or EKG).

While medical heart rate monitoring used in hospitals is usually wired and uses multiple sensors (Holter monitor), consumer HRMs are designed for everyday use and do not use wires to connect. Modern HRMs commonly use one of two different methods to record heart signals (electrical and optical) but both types of signals can provide the same basic data, using fully automated algorithms to measure heart rate, such as the Pan-Tompkins algorithm [11].

The most important part of HRM systems is the non-invasive sensor technology, since sensors are responsible to detect, collect and then through short range connection, deliver information for the continuous remote monitoring of human physiological parameters. There are two kinds of non-invasive sensors for heart rate monitor:

- *Electrocardiography sensors*: Electrocardiogram (ECG or EKG) technology works by placing small metal disks called "electrodes" on the skin which pick up the electrical impulses produced by the heart. ECG technology in wearable devices is seen almost exclusively in thin chest straps and harnesses. The strap electrodes have to be placed in the approximately mid-chest, because the electrodes need to be nearest to the heart to pick up the electrical impulses given off by the heart [12].

  A typical ECG monitoring system consists of the electrodes, amplifier and transmitter, but recently wireless, mobile, and remote technologies have been applied to enhance the functionalities and usability of ECG. When a heartbeat is detected a radio signal is transmitted, which the receiver (smartphone or wristwatch) uses to display/determine the current heart rate. This signal can be a simple radio pulse or a unique coded signal from the chest strap (such as Bluetooth, ANT+, or other low-power radio links that works in the 2.4 GHz radio band) [1].
- *Photoplethysmogram (PPG) sensors*: PPG refers to as Optical Heart rate monitoring (OHRM) and is an optically measurement of the heart rate using LED lights. A PPG consists of the light-emitting diode (LED) usually of infrared light and the photodetector. The process begins with the optical emitter that transfers light waves into the skin. Next, the digital signal processor (DSP) captures the refracted LED light and translates those signals into binary code to be calculated into HR data. The accelerometer measures motion and is combined with the DSP signals to serve as two inputs to the algorithm. Finally, the algorithm translates these inputs into biometric data [1].

  PPG uses two possible modes: reflection and transmission. Transmission relies on placing perfuse tissue between the light source and the detector, while reflection relies on placing both the LED and the detector directly on the skin. In both modes, variation in the PPG signal relies upon path length between source and detector and the optical density of the blood [13].

Due to several interferences, such as optical noise, skin tone or low perfusion, the optical sensing technology is characterized by a reduced accuracy with respect to chest strap counterparts which involve the use of ECG technology. However, thanks to a proliferation of commercially available HR monitors and wearable fitness devices which targets a larger audience than athletes, companies have entered the market of population health, offering a variety of more and more accurate wearable HR and activity monitoring systems to the public. Newer heart rate monitor achieves identical or at least acceptable level of accuracy and can even simultaneously monitor heart rate, oxygen saturation, and other parameters [14].

1.2 Wireless medical sensors and RF communication

Recent advances in wireless and embedded computing systems have led to the emergence of wireless sensor networks consisting of small, battery-powered devices with limited computation and radio communication capabilities. Wireless biomedical telemetry systems performing in the RF bands attract significant scientific interest due to their promising applications in the field of patient care inside hospital, home, or even outside environments. Since smart wearable devices need the access to wireless data networks, antennas are an essential part in the wireless system that transmit and receive electromagnetic radiation in the free space (Figure 3) [15].

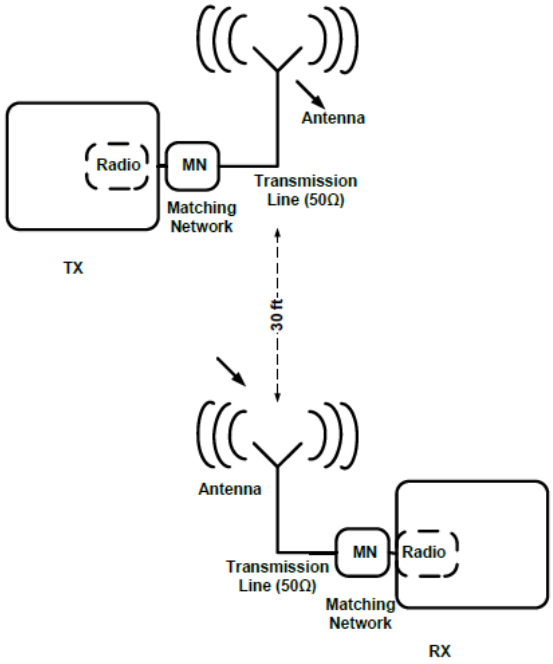

Figure 3: *Typical Short-Range wireless system both at the transmitter (TX) and receiver (RX)* [15].

1.2.1 Antenna

Antennas play an active role in everyday life. Cellular phones and other wireless communication, such as transmission of news from all part of the world, remote control, air travel with radio contact, global positioning satellite system, etc., are made possible by antennas.

The antenna is defined as “that part of a transmitting or receiving system which is designed to radiate or receive electromagnetic wave” and so is part of a system in which the electromagnetic energy is transmitted from some location and, propagating through some medium (typically air or space), is

acquired from the receiver. The receiving antenna then transforms the electromagnetic energy into some useful circuit-level voltages and currents which may then be modified to achieve some desired output. Moreover, it is also able to discriminate between a desired propagated signal and other energies in the electromagnetic environment that can decrease the signal to noise ratio [16].

1.2.1.1 Parameters of antenna

There are different parameters that are taken into consideration when assessing antenna performance, two of them are the *radiation pattern* and *antenna impedance*. The radiation pattern is the spatial distribution of the electric and magnetic field generated by the antenna useful to the signal discrimination based on the direction of the wave arrival. With antenna impedance is defined the lumped-circuit impedance sensed at the antenna terminals by the connected electronic circuitry. It is useful to determine the efficiency of the conversion of the received electromagnetic wave energy to circuit-level voltages and currents [16]. Another important parameter is the *bandwidth* which describes the frequency range over which the antenna can properly radiate or receive power. These radiated signals are electromagnetic waves consisting of electric and magnetic fields which characteristic varies with the distance from the antenna.
The space surrounding an antenna is usually divided into three concentric regions [17] [18]:

- *Reactive (or inductive) near-field region*: region closest to the antenna where the electric and magnetic fields are displayed by 90 degrees from each other. The electric and magnetic fields are strongest in the reactive fields and separate measurements of each field is possible. However, depending on the antenna type, one field dominates over the other.
- *Radiating near-field (Fresnel) region*: region where the electric and magnetic fields are perpendicular to each other with zero phase displacement. It lies between the reactive near-field and far-field regions where there is the transition of the electromagnetic field from reactive to radiative.
- *Far-field (Fraunhofer) region* is the furthest region from the antenna dominated by radiated electromagnetic fields. The far-field region can be defined by the following equation:

$$\text{Far-field exists at a region } > \frac{2D^2}{\lambda} \qquad (1.1)$$

In this region, the radiation pattern of an antenna is independent of the distance from the antenna. The radiation effect is greater in the far-field region, as the electric and magnetic fields are orthogonal to each other, and the direction of propagation is similar to plane waves.

Figure 4: *Field regions of an antenna* [17].

These regions are useful to identify the field structure in each zone, although the transitions between them are gradual, and there are no precise boundaries (Figure 4) [17].

Antenna gain is a measure that considers the efficiency of the antenna and quantifies the degree of directivity of the antenna's radiation pattern. It's defined as "the ratio of the intensity, in a given direction, to the radiation intensity that would be obtained if the power accepted by the antenna were iso-tropically radiated. The radiation intensity is equal to the power accepted by the antenna divided by 4π [18].

The *radiation efficiency* of an antenna is the ratio of power actually radiated (in all directions) to the power absorbed by the antenna terminals. A high-efficiency antenna is capable of radiating most of the accepted power. The radiation efficiency is a number between 0 and 1.

For an ideal loss-less antenna the radiation efficiency is 1 (0 dB) or, in percentage, 100%. Since real antennas are made of real materials with finite conductivity and therefore with conduction losses, part of the power accepted by the antenna is absorbed by it without being radiated. As a result, the radiation efficiency is less than 1 [17].

The *polarization* of an electromagnetic wave is defined as the orientation of plane in which the electric field resides. Antenna polarization is defined as the polarization of the wave that it transmits. The simplest polarization to envision is linear, which is usually either vertical or horizontal polarization (Figure 5). Another type of polarization is circular which is a special case of elliptical polarization which consists of the sum of two orthogonal, linearly polarized waves (usually vertical and horizontal) that are 90 degrees out of phase.

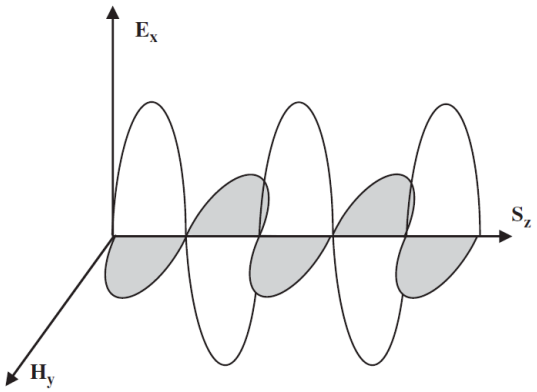

Figure 5: *Conceptual diagram of linear polarization*

The last parameter that has to be considered to assess the antenna performance is the *return loss*. In telecommunications, return loss is a measure in relative terms of the power of the signal reflected by a discontinuity in a transmission line. This discontinuity can be caused by a mismatch between the termination or load connected to the line and the characteristic impedance of the line. It is usually expressed as a ratio in decibels of the incident power and the reflected power (dB):

$$RL(dB) = \ 10\ log_{10}\frac{P_i}{P_r} \qquad (1.2)$$

Return loss is a measure of how well devices or lines are matched. A match is good if the return loss is high. The return loss is related to reflection coefficient (Γ) which is the ratio of the amplitude of the reflected wave to the amplitude of the incident wave. In particular the return loss is the negative of the magnitude of the reflection coefficient in dB, so defined as [18]:

$$RL(dB) = \ -20\log_{10}\left|\frac{V_r}{V_i}\right| = -20\log_{10}|\Gamma| \qquad (1.3)$$

Every wireless system must employ an antenna to radiate and receive electromagnetic energy. The antenna is the transducer between the system and free space and is sometimes referred to as the air interface. A fundamental principle of antennas, called reciprocity, states that antenna performance is the same whether radiation or reception is considered [19] . The implication of this principle is that antenna parameters may be measured either transmitting or receiving. The principle of reciprocity means that estimates of antenna gain, beamwidth, and polarization are the same for both transmit and receive [18].

Antennas can be classified by operating principles or by their application. For 2.4 GHz applications, most PCB antennas fall into the following types [15]:

- *Wire Antenna* is a piece of wire extending over the PCB in free space with its length matched to λ/4 over a ground plane. The wire can be a straight wire, helix, or loop as a three-dimensional (3D) structure, with the antenna over a height of 4-5 mm over the PCB plane, protruding into space.
- *PCB Antenna*: it is a trace drawn on the PCB. This can be a straight trace, inverted F-type trace, meandered trace, circular trace, or a curve with wiggles depending on the antenna type and space constraints. In a PCB antenna, the antenna becomes a two-dimensional (2D) structure in the same plane of the PCB. There are guidelines that must be followed as the 3D antenna exposed in free space is brought to the PCB plane as a 2D PCB trace. A PCB antenna requires more PCB area, has a lower efficiency than the wire antenna, but is cheaper.
- *Chip Antenna*: This is an antenna in a small form-factor IC that has a conductor packed inside. This is useful when there is limited space to print a PCB antenna or support a 3D wire antenna.

The PCB antenna is the more required small antenna in wireless communication, due to the easy manufacturability and the wireless range which is acceptable for Bluetooth Low Energy (BLE) application. The PCB antenna can be of different configurations: inverted-F, meandered inverted-F and planar inverted-F.

1.2.1.2 Inverted-F antenna – IFA

The *Inverted F Antenna* (IFA) typically consists of a rectangular planar element located above a ground plane, a short-circuiting plate or pin, and a feeding mechanism for the planar element.
The Inverted F antenna is a variant of the monopole where the top section has been folded down so as to be parallel with the ground plane. This is done to reduce the height of the antenna, while maintaining a resonant trace length. This parallel section introduces capacitance to the input impedance of the antenna, which is compensated by implementing a short-circuit stub. The stub's end is connected to the ground plane of the antenna which plays a significant role in its operation. Excitation of currents in the printed IFA causes excitation of currents in the ground plane (Figure 6) [15][20].

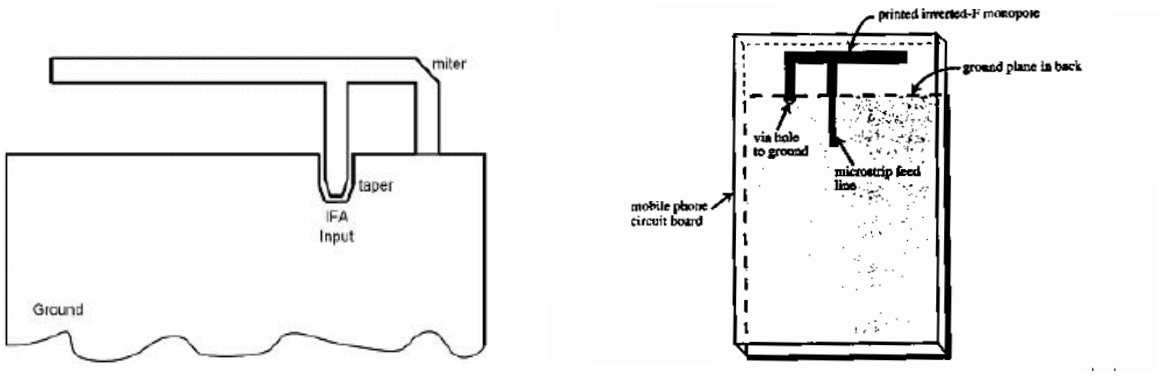

Figure 6: *Inverted-F antenna geometry schemes [20]*

Characteristics:

- The antenna/ground combination will behave as an asymmetric dipole, the differences in current distribution on the two-dipole arms being responsible for some distortion of the radiation pattern.
- In general, the required PCB ground plane length is roughly one quarter (λ/4) of the operating wavelength. If the ground plane is much longer than λ/4, the radiation patterns will become increasingly multilobed. On the other hand, if the ground plane is significantly smaller than λ/4, then tuning becomes increasingly difficult and the overall performance degrades.
- The optimum location of the IFA in order to achieve an omni-directional far-field pattern and 50 Ω impedance matching was found to be close to the edge of the PCB.
- The *miter* is used to avoid a right angle microstrip bend, which results in a poor current flow on the stub.
- IFA bandwidth increases with its thickness.

The taper is needed in order to compensate the abrupt step transition encountered between the microstrip line feed and the antenna.
The design of IFA has two main advantages over a simple monopole: the antenna is shorter and more compact, allowing it to be contained within the case of the mobile device, and it can be impedance matched to the feed circuit by the designer, allowing it to radiate power efficiently, without the need for extraneous matching components [21].

The *Meandered Inverted-F Antenna – MIFA* is a popular antenna also used in human interface devices (HIDs) because it occupies a small PCB area. It is a variation of IFA that may be used when there is

insufficient board space to extend an antenna to the full required length. The antenna may be meandered to reduce its height while retaining its designed electrical length (Figure7) [15].

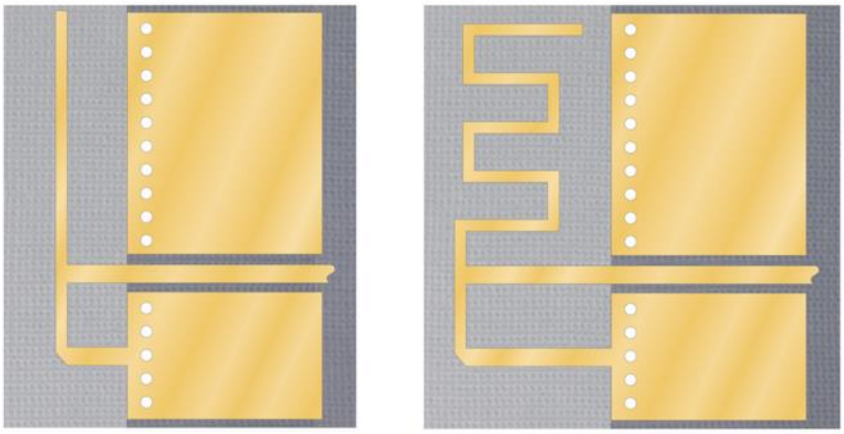

Figure 7: Inverted-F and Meandered Inverted-F antenna differences schemes

1.2.1.3 Planar Inverted F Antenna - PIFA

The most widespread use of IFA is as planar inverted-F antenna (PIFA) in mobile wireless devices for its space saving properties. PIFA can be considered as a kind of linear Inverted F antenna (IFA) with the wire radiator element replaced by a plate to expand the bandwidth [15].
PIFAs can be printed using the microstrip format, a widely used technology that allows printed RF components to be manufactured as part of the same printed circuit board used to mount other components (Figure.8) [20]. PIFA is characterized by the following advantages:

- One advantage is that can be hiding into the housing of the mobile when comparable to whip/rod/helix antennas.
- PIFA have reduced backward radiation toward the user's head, minimizing the electromagnetic wave power absorption (SAR) and enhance antenna performance.
- It exhibits moderate to high gain in both vertical and horizontal states of polarization. This feature is very useful in certain wireless communications where the antenna orientation is not fixed, and the reflections are present from the different corners of the environment. In those cases, the important parameter to be considered is the total field that is the vector sum of horizontal and vertical states of polarization.

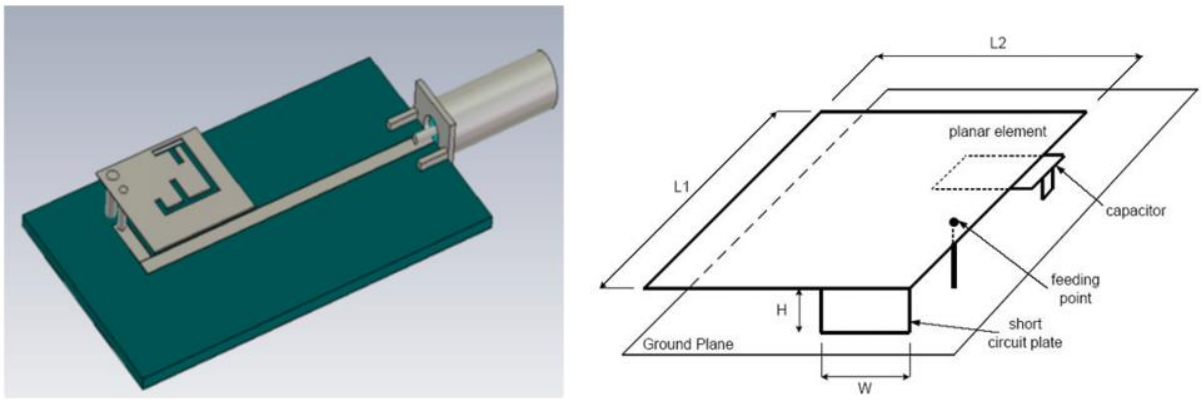

Figure .8: Planar Inverted-F antenna schemes [22]

Narrow bandwidth characteristic of PIFA is one of the limitations for its commercial application for wireless mobile. The shorting post near the feed probe point of usual PIFA types is a good method for reducing the antenna size, but this results into a narrow impedance bandwidth.
The size of the ground plane can be varied in order to increase the bandwidth, since it is affected by the size of the ground plane. For example, reducing its dimension can effectively increase the bandwidth of the antenna system [20].

PIFA dimensions are also important in order to be used for wireless circuitry implemented in microstrip. One method of reducing PIFA size is simply by shortening the antenna. However, this approach affects the impedance at the antenna terminals such that the radiation resistance becomes reactive as well. This can be compensated with *capacitive top loading*. In practice, the missing antenna height is replaced with an equivalent circuit, which improves the impedance match and the efficiency. The capacitive loading reduces the resonance length from λ/4 to less than λ/8 at the expense of bandwidth and good matching. The capacitive load can be produced by adding a plate (parallel to the ground) to produce a parallel plate capacitor [22].

PIFA is the most frequently used internal antenna in mobile phone designs since is characterized by a simple design, lightweight, low cost, compactness, conformable nature, and reliable performance. IFA instead, are widely used in compact hand-held wireless devices where space is important. This includes mobile phones and tablet computers using wireless transmissions such as GSM, Bluetooth, and Wi-Fi [23].

1.2.2 Smart device connectivity

In the communications field the terms LAN (Local Area Network) and WAN (Wide Area Network) are used to denote a network able to cover an area such as a house, a housing complex, a hospital, an institution, or a city; the terms BAN (Body Area Network) and PAN (Personal Area Network) are used to denote a network of a smaller scale, analogous to humans, their dimensions, and their personal area, that is a few meters or less [1].

The communication between the cell phone and the wireless sensors is implemented by forming a Bluetooth PAN which can offer wireless, restraint-free, simultaneous, real-time, long-term data gathering of physiological variable quantity.

The most appropriate wireless medical technology is selected according to different parameters:

a. Range over which the device needs to operate.
b. Amount of data that needs to be transferred.
c. Throughout speed needed to fulfil accurate estimations, the frequency of these transfers which is how often data need to be sent.
d. Power available: typically, whether the devices are battery operated or main supply powered.

Bluetooth is an open wireless technology standard for exchanging data over short distances from fixed and mobile devices by using short-length (100 m) radio waves and creating PANs. It can, in its current specification, connect several devices forming small short-range networks and allowing a person to have a phone conversation via a headset, use a wireless mouse and synchronize information from a mobile phone to a PC, all using the same core system. [24]

Bluetooth Low Energy (BLE) wireless technology (also called Smart Bluetooth) is a feature of the Bluetooth version 4.0 specification, special at new applications for wireless devices. Its chief advantage is enabling very low battery use within a short range (10-50 m). This facilitates a smaller form factor of devices and a wide range of applications in the health care, fitness, and home entertainment industries. BLE is designed with two implementation alternatives: single-mode and dual-mode. Small, highly integrated, and compact devices like watches and sports sensors based on a *single-mode BLE implementation* will benefit from the low-power consumption advantages. In *dual-mode implementations* BLE functionality is integrated into classic Bluetooth circuits. The architecture will share classic Bluetooth technology radio and antenna, enhancing classic Bluetooth chips with the new low-energy stack, and will be backward compatible with previous implementations of the protocol [24].

ANT + is another ultra-low-power, short-range wireless technology, similar to Bluetooth, that is predominantly used for sport and fitness wireless connectivity. This service allows the connection of ANT+ sensor networks to apps or compatible devices and as Bluetooth and BLE, enables hardware operating in the 2.4 GHz ISM band (between 2.400–2.4835 GHz, the same range of frequencies used by microwaves) [24].
Other type of wireless technology that can be used are Wi-Fi, light fidelity (LiFi), universal serial bus (USB), ZigBee, wireless universal serial bus (WUSB), Z-Wave, RFID (radio frequency identification), Infrared Data Association (IrDA), and near-field communication (NFC) [1].

Antennas are essential parts of RF biomedical telemetry systems. Their complexity highly depending on the surrounding tissue environment (proximity to the human body), electronics, communications, and medical requirements. The human body is a lossy material for electromagnetic waves, this means that the body converts electric fields into heat and absorbs energy from electromagnetic waves. Thus, when an antenna is placed near the body, the results is a large reduction of the antenna efficiency. An approach that can be extremely useful to model essentially arbitrary configurations of inhomogeneous, lossy dielectric materials is the finite different time domain technique (FDTD). When properly implemented, FDTD analyses of antennas produce, in a straightforward manner, wideband results for complex antenna structure even embedded within essentially arbitrary configurations of inhomogeneous materials.

1.3 Finite-Difference Time-Domain (FDTD)

The Finite-Difference Time-Domain (FDTD) is a numerical analysis technique used for modelling the interaction of electromagnetic fields with physical objects and the environment, also known as computational electrodynamics. This technique can be applied to several real-world electromagnetic problems – such as electromagnetic scattering, electromagnetic radiation, wave propagation problems, etc. – which are not analytically calculable for the multitude of irregular geometries found in actual devices. It represents an advantage as a simulation and analysis tool for complicated electromagnetic studies and involves the use of computer programs to find approximate solutions to the associated system of differential equation [25].

1.3.1 History of FDTD

James Clerk Maxwell formulated Maxwell's equations in 1873. Before the 1960s, exact analytical solutions of Maxwell's equations were limited to simple and symmetrical structures, find through *classical methods* such as *separations of variables* and *conformal transformations*. Despite the computational simplicity, analytical methods have different disadvantages and for this reason have limited usage on solving complex electromagnetic problems.

In 1960s, the advancement of computer technology prompted the researchers to investigate the use of *numerical methods* to overcome the limitations of classical ones, in particular, for the accurate characterization of complex geometry.

- *Finite element method* (FEM) is a widely used numerical method for solving partial differential equations in two or three space variables, that subdivides a large system into smaller, simpler parts that are called finite elements. This subdivision of the whole domain into simpler parts allows an accurate description of complex geometry and inhomogeneous materials and an easy representation of the total solution [26].
- *Method of Moments* (MoM) is a rigorous, full-wave numerical technique for solving open boundary electromagnetic problems. The MoM is an integral equation technique, and it solves the integral form of Maxwell's equations instead of their differential forms which are used in the finite element methods.
- *The Finite Difference Time Domain* (FDTD) method is an application of the finite difference method to solve Maxwell's equations. In FDTD, space is divided into small portions called cells. On the surfaces of each cell, there are assigned points and each point in the cell is required to satisfy Maxwell's equations. In this way, electromagnetic waves are simulated to propagate in a numerical space, almost as they do in real physical world.

The FDTD method is presented for the first time by Kana Yee in 1966 [27], while the name and acronym "FDTD" was coined by Allen Taflove in 1980 [28].
This method is arguably the simplest, both conceptually and in terms of implementation, of the full-wave numerical techniques and employs finite differences as approximations to both the spatial and temporal derivatives that appear in Maxwell's equations in order to solve electromagnetic field problems in many applications, ranging from the design of antennas to bio-photonics.

It can solve complicated problems and analyse electromagnetic phenomena at radio and microwave frequencies, but it is generally computationally expensive, in fact solutions may require a large amount of memory and computation time [29].
The advantages of FDTD can be summarized as its ability to work with a wide range of frequencies, objects, and environments, added to the advantage of computational efficiency for large problems in comparison with other techniques [25].

1.3.2 Yee's Algorithm

In 1966, K.S. Yee published his classic research paper "Numerical solution of initial boundary value problems involving Maxwell's equations in isotropic media.", in which introduced a way to solve both electric and magnetic fields in time and space using the coupled Maxwell's curl equations [27].
Starting from the time-dependent Maxwell's curl equations in an isotropic medium ($\sigma = 0$), Yee's algorithm define a set of finite-difference equations and a discretization of the structure geometry (grid of the space define as Δx, Δy, and Δz) to evaluate simultaneously the two fields.
The result is a system of linear equations ("update equations") where the values of the electric field vector components in a volume of space are solved at a given instant of time while, the magnetic field vector components in the same spatial volume are solved at the next instant in time. The process is repeated until the desired transient or steady-state electromagnetic field behaviour is obtained.
So, the FDTD algorithm provides a way to obtain the future fields from the past fields and this type of method, in which one field is advanced and then the other, and then the process is repeated, is known as a *leap-frog method* [29].

1.3.2.1 Transition from Maxwell's equations to a set of finite difference equations

Maxwell's equations in a linear, isotropic nondispersive medium are given by [27]:

$$\begin{aligned} \nabla \times \vec{E} &= -\frac{\partial \vec{B}}{\partial t} \\ \nabla \times \vec{H} &= \sigma \vec{E} + \frac{\partial \vec{D}}{\partial t} \end{aligned} \qquad (2.1)$$

$$\begin{cases} \vec{B} = \mu \vec{H} \\ \vec{D} = \varepsilon \vec{E} \end{cases} \qquad (2.2)$$

Here $\vec{E}$ is the electric field vector in volts per meter, $\vec{D}$ is the electric flux density vector in coulombs per square meter, $\vec{H}$ is the magnetic field vector in amperes per meter, $\vec{B}$ is the magnetic flux density vector in webers per square meter, μ is the magnetic permeability in henrys per meter and ε is the electric permittivity in farads per meter. Moreover, in order to account the electric loss mechanisms that can dissipate electromagnetic fields in materials, an equivalent electric current $\sigma\vec{E}$ is defined where σ is the electric conductivity in siemens per meter [16].

Assuming that: μ, σ and ε are all time-independent, it's possible to decompose the electric and magnetic fields into an equivalent system of scalar equations which are the vector components of the fields represented in the three-dimensional rectangular coordinate system (*x, y,* and *z*):

$$\begin{cases} \frac{\partial E_y}{\partial z} - \frac{\partial E_z}{\partial y} = \frac{\partial B_x}{\partial t} \\ \frac{\partial E_z}{\partial x} - \frac{\partial E_x}{\partial z} = \frac{\partial B_y}{\partial t} \\ \frac{\partial E_x}{\partial y} - \frac{\partial E_y}{\partial x} = \frac{\partial B_z}{\partial t} \end{cases} \quad (2.3)$$

$$\begin{cases} \frac{\partial H_y}{\partial z} - \frac{\partial H_z}{\partial y} = \sigma E_x + \frac{\partial D_x}{\partial t} \\ \frac{\partial H_z}{\partial x} - \frac{\partial H_x}{\partial z} = \sigma E_y + \frac{\partial D_y}{\partial t} \\ \frac{\partial H_x}{\partial y} - \frac{\partial H_y}{\partial x} = \sigma E_z + \frac{\partial D_z}{\partial t} \end{cases} \quad (2.4)$$

Starting from the system of six coupled partial differential equations (2.3) and (2.4), thanks to one space-time discretization, it will be possible to find the six finite difference equations, which forms the basis of the Finite-Difference Time-Domain method.

1.3.2.2 Spatial and temporal discretization

In FDTD simulations there are restrictions on how large a temporal step can be, if it is too large, the algorithm produces unstable results. Moreover, in most instances, even if when the specific region of interest may be small, in order to model magnetic problems that exist in an unbounded space, a spatial and temporal discretization is required [29].

So, the first step to use the FDTD algorithm is to identify the region affected by the problem, divide the structure geometry into cells of space having dimensions Δx, Δy and Δz and choose the temporal step in which the electromagnetic field have to be evaluated [27].

As illustrated in Figure .9, the Yee algorithm subdivides the space into a three-dimensional grid, called Yee cube or Yee space lattice, in which centres the $\vec{E}$ and $\vec{H}$ components. The vector components are positioned so that every $\vec{E}$ component is surrounded by four circulating $\vec{H}$ components, and every $\vec{H}$ component is surrounded by four circulating $\vec{E}$ components. Through the Yee cube is possible to obtain an approximation of the surface and internal geometry of the structure of interest with a space resolution set by the size of the lattice unit cell.

The algorithm also centres the $\vec{E}$ and $\vec{H}$ components in time in a leap-frog arrangement (Figure .10). All of the $\vec{E}$ computations in the three-dimensional space are completed and stored for a particular time point using $\vec{H}$ data previously stored in the computer memory. Then all of the $\vec{H}$ computations are completed and store using $\vec{E}$ data just computed. The cycle can begin again, and the process continues until time-step is concluded.

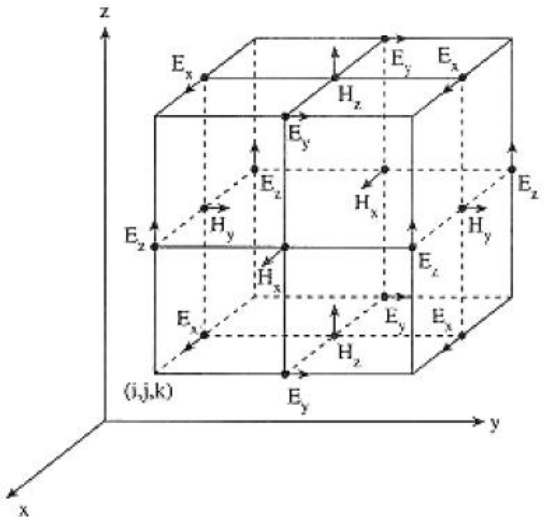

Figure 9: *Position of the electric and magnetic field vector components about a cubic unit cell of the Yee space lattice. The electric field components are placed along the cube edges, while the magnetic field components are on the cube face* [29].

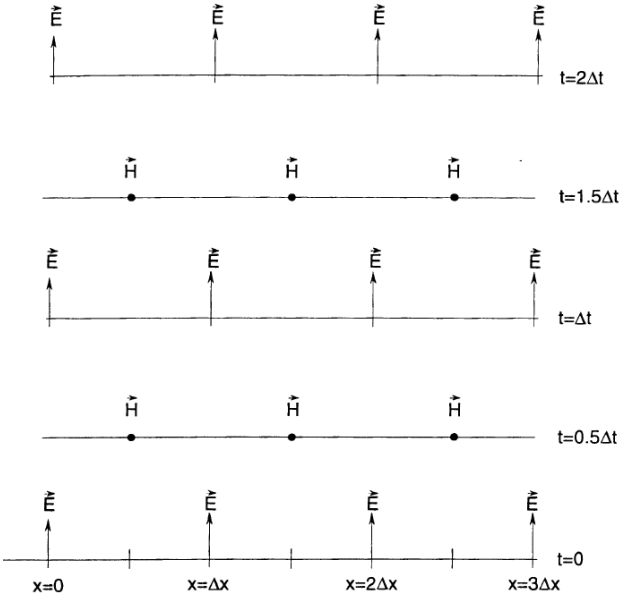

Figure 10: *Space-time chart of the Yee algorithm for a one-dimensional wave propagation. Initial condition for both electric and magnetic fields are zero everywhere in the grid* [16].

1.3.2.3 The system of finite difference equations

Once analysed the problem, it is possible to define the length of the edge of the cubes constituting the grid and the duration of a temporal step. Assume that a grid point in the space is denoted as:

$$(i, j, k) = (i\Delta x, j\Delta y, k\Delta z) \tag{2.5}$$

and that each space-time function is evaluated at a discrete point in the grid and at a discrete point in time as:

$$F(i\Delta x, j\Delta y, k\Delta z, n\Delta t) = F_n(i, j, k) \tag{2.6}$$

where $n\Delta t$ denote the instant of time in which F is considered.

It is possible, using the introduced notation, to replace the partial space derivative of F with the following incremental ratios:

$$\begin{cases} \frac{\partial F}{\partial x} = \frac{F|_{i+1,j,k}^{n} - F|_{i,k,j}^{n}}{\Delta x} + O((\Delta x)^2) \\ \frac{\partial F}{\partial y} = \frac{F|_{i,j+1,k}^{n} - F|_{i,k,j}^{n}}{\Delta y} + O((\Delta y)^2) \\ \frac{\partial F}{\partial z} = \frac{F|_{i,j,k+1}^{n} - F|_{i,k,j}^{n}}{\Delta z} + O((\Delta z)^2) \\ \frac{\partial F}{\partial t} = \frac{F|_{i,j,k}^{n+1} - F|_{i,k,j}^{n}}{\Delta t} + O((\Delta t)^2) \end{cases} \quad (2.7)$$

By means of relatively simple mathematical passages and observations, a numerical approximation of the Maxwell's curl equations in three dimensions, given by (2.3) and (2.4), is achieved.
Consider the first equation of the system (2.3), repeated for convenience:

$$\frac{\partial E_y}{\partial z} - \frac{\partial E_z}{\partial y} = \mu \frac{\partial E_x}{\partial t} + \sigma^* H_x \quad (2.8)$$

passing through the partial derivatives calculate in a point of the grid (i, j, k), we obtain:

$$\frac{1}{\mu_{i,j,k}} \left(\frac{E_y|_{i,j,k+\frac{1}{2}}^{n} - E_y|_{i,j,k+\frac{1}{2}}^{n}}{\Delta z} - \frac{E_z|_{i,j+\frac{1}{2},k}^{n} - E_z|_{i,j+\frac{1}{2},k}^{n}}{\Delta y} - \sigma_{i,j,k}^{*} H_x|_{i,j,k}^{n} \right) = \frac{H_x|_{i,j,k}^{n+\frac{1}{2}} - H_x|_{i,j,k}^{n-\frac{1}{2}}}{\Delta t} \quad (2.9)$$

All the quantities on the left-hand side are evaluated at the time step n, including the magnetic field in the right-hand side which is not assumed to be stored in the computer's memory (only its previous term), but is estimated through a semi-implicit approximation:

$$H_x|_{i,j,k}^{n+\frac{1}{2}} = \frac{H_x|_{i,j,k}^{n+\frac{1}{2}} - H_x|_{i,j,k}^{n-\frac{1}{2}}}{2} \quad (2.10)$$

substituting into the equation (2.9):

$$H_x\big|_{i,j,k}^{n+\frac{1}{2}} = \left(\frac{1-\frac{\sigma^*_{i,j,k}\Delta t}{2\mu_{i,j,k}}}{1+\frac{\sigma^*_{i,j,k}\Delta t}{2\mu_{i,j,k}}}\right) H_x\big|_{i,j,k}^{n-\frac{1}{2}} + \left(\frac{\frac{\Delta t}{\mu_{i,j,k}}}{1+\frac{\sigma^*_{i,j,k}\Delta t}{2\mu_{i,j,k}}}\right) \cdot \left(\frac{E_y\big|_{i,j,k+\frac{1}{2}}^{n} - E_y\big|_{i,j,k+\frac{1}{2}}^{n}}{\Delta z} - \frac{E_z\big|_{i,j+\frac{1}{2},k}^{n} - E_z\big|_{i,j+\frac{1}{2},k}^{n}}{\Delta y}\right) \quad (2.11)$$

With an analogue technique, the finite-difference expressions for the other field components are defined:

$$H_y\big|_{i,j,k}^{n+\frac{1}{2}} = \left(\frac{1-\frac{\sigma^*_{i,j,k}\Delta t}{2\mu_{i,j,k}}}{1+\frac{\sigma^*_{i,j,k}\Delta t}{2\mu_{i,j,k}}}\right) H_y\big|_{i,j,k}^{n-\frac{1}{2}} + \left(\frac{\frac{\Delta t}{\mu_{i,j,k}}}{1+\frac{\sigma^*_{i,j,k}\Delta t}{2\mu_{i,j,k}}}\right) \cdot \left(\frac{E_z\big|_{i+\frac{1}{2},j,k}^{n} - E_z\big|_{i+\frac{1}{2},j,k}^{n}}{\Delta x} - \frac{E_x\big|_{i,j,k+\frac{1}{2}}^{n} - E_x\big|_{i,j,k+\frac{1}{2}}^{n}}{\Delta z}\right) \quad (2.12)$$

$$H_z\big|_{i,j,k}^{n+\frac{1}{2}} = \left(\frac{1-\frac{\sigma^*_{i,j,k}\Delta t}{2\mu_{i,j,k}}}{1+\frac{\sigma^*_{i,j,k}\Delta t}{2\mu_{i,j,k}}}\right) H_z\big|_{i,j,k}^{n-\frac{1}{2}} + \left(\frac{\frac{\Delta t}{\mu_{i,j,k}}}{1+\frac{\sigma^*_{i,j,k}\Delta t}{2\mu_{i,j,k}}}\right) \cdot \left(\frac{E_x\big|_{i,j+\frac{1}{2},k}^{n} - E_x\big|_{i,j+\frac{1}{2},k}^{n}}{\Delta y} - \frac{E_y\big|_{i+\frac{1}{2},j,k}^{n} - E_y\big|_{i+\frac{1}{2},j,k}^{n}}{\Delta x}\right) \quad (2.13)$$

$$E_x\big|_{i,j,k}^{n+\frac{1}{2}} = \left(\frac{1-\frac{\sigma^*_{i,j,k}\Delta t}{2\varepsilon_{i,j,k}}}{1+\frac{\sigma^*_{i,j,k}\Delta t}{2\varepsilon_{i,j,k}}}\right) E_x\big|_{i,j,k}^{n-\frac{1}{2}} + \left(\frac{\frac{\Delta t}{\varepsilon_{i,j,k}}}{1+\frac{\sigma^*_{i,j,k}\Delta t}{2\varepsilon_{i,j,k}}}\right) \cdot \left(\frac{H_z\big|_{i,j+\frac{1}{2},k}^{n+\frac{1}{2}} - H_z\big|_{i,j+\frac{1}{2},k}^{n+\frac{1}{2}}}{\Delta y} - \frac{H_y\big|_{i,j,k+\frac{1}{2}}^{n+\frac{1}{2}} - H_y\big|_{i,j,k+\frac{1}{2}}^{n+\frac{1}{2}}}{\Delta z}\right) \quad (2.14)$$

$$E_y\big|_{i,j,k}^{n+\frac{1}{2}} = \left(\frac{1-\frac{\sigma^*_{i,j,k}\Delta t}{2\varepsilon_{i,j,k}}}{1+\frac{\sigma^*_{i,j,k}\Delta t}{2\varepsilon_{i,j,k}}}\right) E_y\big|_{i,j,k}^{n-\frac{1}{2}} + \left(\frac{\frac{\Delta t}{\varepsilon_{i,j,k}}}{1+\frac{\sigma^*_{i,j,k}\Delta t}{2\varepsilon_{i,j,k}}}\right) \cdot \left(\frac{H_x\big|_{i,j,k+\frac{1}{2}}^{n+\frac{1}{2}} - H_x\big|_{i,j,k+\frac{1}{2}}^{n+\frac{1}{2}}}{\Delta z} - \frac{H_z\big|_{i+\frac{1}{2},j,k}^{n+\frac{1}{2}} - H_z\big|_{i+\frac{1}{2},j,k}^{n+\frac{1}{2}}}{\Delta x}\right) \quad (2.15)$$

$$E_z\big|_{i,j,k}^{n+\frac{1}{2}} = \left(\frac{1-\frac{\sigma^*_{i,j,k}\Delta t}{2\varepsilon_{i,j,k}}}{1+\frac{\sigma^*_{i,j,k}\Delta t}{2\varepsilon_{i,j,k}}}\right) E_z\big|_{i,j,k}^{n-\frac{1}{2}} + \left(\frac{\frac{\Delta t}{\varepsilon_{i,j,k}}}{1+\frac{\sigma^*_{i,j,k}\Delta t}{2\varepsilon_{i,j,k}}}\right) \cdot \left(\frac{H_y\big|_{i+\frac{1}{2},j,k}^{n+\frac{1}{2}} - H_y\big|_{i+\frac{1}{2},j,k}^{n+\frac{1}{2}}}{\Delta x} - \frac{H_x\big|_{i,j+\frac{1}{2},k}^{n+\frac{1}{2}} - H_x\big|_{i,j+\frac{1}{2},k}^{n+\frac{1}{2}}}{\Delta y}\right) \quad (2.16)$$

With the system of equations (2.11), (2.12), (2.13), (2.14), (2.15) and (2.16), obtained from Yee notation, is possible to find the electric and magnetic field components in any point of the grid and analyse the evolution of the electromagnetic field at each point of the chosen volume, based on the values assumed in the previous instants and on the components of the field of adjacent cells.

1.3.3 Numerical dispersion and stability

In the FDTD algorithm, numerical dispersion and stability are the two main factors that affect the choice of time step, Δt and lattice space increments, Δx , Δy and Δz. In a uniform one-dimensional grid, numerical dispersion is reduced to ideal and the solution of a continuous one-dimensional wave equation, given by the Yee algorithm, is exact. Instead, for two-or three-dimensional Yee space lattice, the direction of wave propagation affects the numerical dispersion, which means that the phase velocity of the numerical wave differs from the vacuum speed of light. This variation depends on the modal wavelength, the direction of the wave propagation in the grid, and the grid discretization [16]. The numerical dispersion error can be quantified by the physical phase-velocity error and the velocity-anisotropy error, where the physical phase-velocity error measures the amount of phase lead

or lag, while the velocity anisotropy error measures the wavefront distortion due to the anisotropy of the space lattice.

Physical phase-velocity error can be reduced by proper choice of grid discretization, under the condition of maintain the geometry of the problem the simpler as possible. Therefore, discretization must guarantee two requirements: computational stability and accuracy.

Meaningful results are obtained through proper size selection of the cells, which is satisfy if the linear dimension of the grid is a fraction of the wavelength present in the problem under consideration. Assuming a cubic grid in which $\Delta x = \Delta y = \Delta z$, the accuracy improves under the condition:

$$\Delta x < \frac{\lambda_{min}}{10} \qquad (2.17)$$

In time instead, for computational stability, the *Courant–Friedrichs–Lewy condition* must be satisfied. Thus, the stability of the associated numerical system, in case of cubic cell, is maintained if the temporal step is:

$$\Delta t \leq \frac{1}{c_0\sqrt{\frac{1}{(\Delta x)^2}+\frac{1}{(\Delta y)^2}+\frac{1}{(\Delta z)^2}}} = \frac{1}{c_0\frac{\sqrt{3}}{(\Delta x)}} = \frac{\Delta x}{c_0\sqrt{3}} \qquad (2.18)$$

$$S = \frac{c_0 \Delta t}{\Delta_x} = \frac{1}{\sqrt{3}} \qquad (2.19)$$

where the dimensionless number S is called the *Courant number*, commonly defined as stability factor.

So, according to the two equations (2.18) and (2.19), the stability condition is satisfied if the FDTD algorithm is faster than the propagation wavelength. Exceeding the S value, brings to the divergence of results after few iterations and a failure of the program as the results cannot be longer represented. The stability of the overall FDTD solution procedure for Maxwell's equations depends upon more than the stability of the Yee algorithm.

Up until now, the discussion on the stability focused on the numerical stability of the basic Yee algorithm in Cartesian coordinates. However, the stability of the overall FDTD procedure depends upon more than this factor. A *generalized stability problem* arises due to interactions between the Yee algorithm and any augmenting algorithms used to model boundary conditions, variable meshing and complex materials. [30]

1.3.3.1 Boundary conditions

To model numerically wave propagation phenomena in a domain which extends to infinity, it is common practice to truncate the computational domain to a finite domain.
The newly formed external boundary is somewhat artificial thus to reduce undesired numerical reflections, there is a need for a special treatment at these boundaries.
In FDTD, in order to extend the solutions obtained from the Yee algorithm at an infinite domain, it is possible to use suitable boundary conditions on the outer perimeter of the domain once the electric and magnetic fields on the external surface of the region of interest are known [30].
There are two types of boundary conditions depending upon the theoretical basis: RBCs or Radiation Boundary Condition and the ABCs or Absorbing Boundary Conditions. Of the two classes of solutions, the ABCs ones are the most used with the FDTD method, even though both introduce errors, spurious reflections.
The initial studies to search for suitable boundary conditions were addressed by Gerrit Mur in 1981. Mur's solution represents the first valid answer to the boundary condition problem for methods that exploit a spatial grid in order to solve the Maxwell's equations and result a good choice for problems that do not require a high precision solution due to its simplicity and computational efficiency.
All the ABCs results obtained from Mur and others who published their works before 1994 provide effective outer-boundary reflection coefficient around -35 and -45dB although to obtain simulations having good dynamic range a 40 dB reduction of the effective reflection coefficient is needed [30]. Moreover, they present a limitation in condition of oblique incident wave since, in particular for the first order Mur's solution, oblique wave cannot be absorbed and so are reflected inside the boundary.
The perfectly matched layer (PML) introduced by J.P. Berenger for Maxwell's equations represent the alternative that allows to overcome these limitations. It consists in splitting the electric or magnetic field's components in the absorbing boundary region into a subcomponent that can be perfectly absorbed by the perfectly matched layer material. The net effect of this is to create a non-physical absorbing medium adjacent to the outer FDTD mesh boundary that has a wave impedance independent of the angle of incidence and frequency of outgoing scattered waves. Therefore, when a wave crosses the edge of the region of interest it is not reflected and is attenuated according to exponential decay. This approach allows for an increase in the maximum dynamic range to a value greater than 80 dB [30].
The PML ABC provides a combination of broadband effectiveness, robustness, and computational efficiency that is unmatched by any previous ABC, nevertheless, it is important to remember that the absorbing boundary condition has no real equivalent; they are mathematical schemes applied at the

artificial numerical boundaries of a computational domain to minimize or eliminate the spurious reflections at these boundaries which occur in the simulations of wave propagation phenomena [31].

1.3.3.2 Variable and unstructured meshing

FDTD algorithm is based on an orthogonal regular Cartesian lattice. Due to the orthogonality of the grid and the uniform spacing between grid points, the first-order derivatives of Maxwell's equations can be approximated using central-difference operators [30]. This leads to a second-order accurate solution in space and time and a discrete approximation for the fields based on a uniform orthogonal lattice.

Unfortunately, structures with fine geometrical features cannot always conform to the edges of the uniform lattice. In studies where the field interaction is highly dependent on the shape of the boundary and the grid does not conform to the shape of the boundary - such as a curved or a planar boundary- a substantial error can occur in the calculation . This is the reason why the boundary conditions cannot be enforced directly on the boundary, but rather on an auxiliary boundary, which is a staircase approximation of the physical boundary.

The use of non-uniform grids and the reduction of the actual cell size is sometimes necessary to model accurately the local fields. A quasi-uniform grid FDTD algorithm was introduced by Sheen in 1991. This method is based on reducing the grid size by exactly one-third, thus the spatial derivatives of the fields at the interface between the two regions can be expressed using central-difference approximations, resulting in a second order accurate formulation. The method is limited to specific geometries that conform to this specialized grid but for complex and highly detailed circuits having rectangular geometries, the nonuniform FDTD algorithm represent a powerful and versatile technique [30].

1.3.3.3 Lossy, dispersive, nonlinear, and gain materials

The control or processing of short electromagnetic pulses necessarily involves understanding the nature of pulses interactions with materials over wide bandwidths. Generally, the key factor in short-pulse physics are material dispersion, nonlinearity, and gain [16].

- Linear dispersion: a material's permittivity and/or permeability varies with frequency at low intensities of the electromagnetic wave.

- Nonlinearity: the material's dielectric permittivity and/or permeability varies with the local intensity of the interaction electromagnetic wave, especially at high intensities.
- Nonlinear dispersion: the strength of a material's nonlinear characteristics varies with the sinusoidal frequency content of the interacted electromagnetic wave.
- Gain: provides an exponential increase of the interacting wave with propagation distance in the material, as opposed to an exponential loss as in conventional materials. Gain is generally a function of the frequency and intensity of the interacting wave and can also be frequency-dispersive and nonlinear [30][32].

There are two approaches of FDT computational technology that permit effective modelling of the material properties at the macroscopic level. The first is the recursive convention (RC) method, a highly efficient approach to model complicated linear dispersions; the second method, instead, is the auxiliary differential equation (ADE) methods, which permits modelling of nonlinearities and dispersive nonlinearities in addiction to linear dispersions, at the cost of an increase in computational complexity.
This FDTD approach achieves robustness by directly solving for the electric and magnetic field fundamental quantities in time and space and enforces the vector field boundary conditions at all interfaces of dissimilar media, whether or not the media are dispersive or nonlinear. As a result, it allows an accurate modelling of a broad variety of dispersive, nonlinear and gain materials.

1.3.4 Analysis of the strong and weak points of method

In order to evaluate the efficiency and the validity of the approach, the strong and weak points of method need to be highlighted:

1. The FDTD method *uses no linear algebra*. It is a relatively simple computational technique, characterize by not complex calculation.
2. It *is very accurate and robust*: errors are easy to individuate and can be limited.
3. The FDTD technique is a *time domain method* so allows to obtain solutions for broadband system with a single simulation, *deal with non-linear behaviours* and *compute the impulse response* of an electromagnetic system.
4. Since electric and magnetic fields are calculated instant by instant, it is possible to follow their evolution step by step over time.

5. It is a *systematic approach*: the subdivision of the space into small cubes allows the specification of the characteristic of the materials for each cell. Moreover, smaller the cell, more precise the results obtained will be, but this will mean the increase of the computational effort.

On the other hand:

1. The accuracy of the results, obtains from very small space-time discretization, comes with a very high computational cost.
2. The space discretization and the representation of the objects contained in the region of interest of the problem, introduces systematic errors that cause inaccuracy in the results.
3. Since the stability condition requires a grid cell to be large at most 1/10 of the wavelength, to have acceptable computational costs, it is necessary to deal with very small spatial domains.
4. The results of FDTD technique are define on a finite domain which brings to an approximation error. With the boundary condition is possible to extend the solution to an infinite domain and so overcome this limitation.

1.3.5 Excitation

In order to study the dynamic properties and the responses (output) of systems in the frequency domain through FDTD simulation, excitation signals are applied as input of the system under consideration [16].
The type of excitation signal, used to estimate frequency response functions, depends upon several factors. Generally, the excitation signal is chosen in order to minimize noise while estimating the most accurate frequency response function in the least amount of time. The excitation that has to be modelled for a system depends upon the particular application:

- When the system has to be analysed over a *band of frequencies*, it is efficient to excite with a Gaussian pulse and then use the Fourier transform to obtain the response in the frequency domain over the desire band. However, its spectrum has significant low-frequency content and for some problems, this can produce an unacceptably long settling time for the solution. An alternative is to use the Differentiated Gaussian pulse (Figure 11) [16][33].

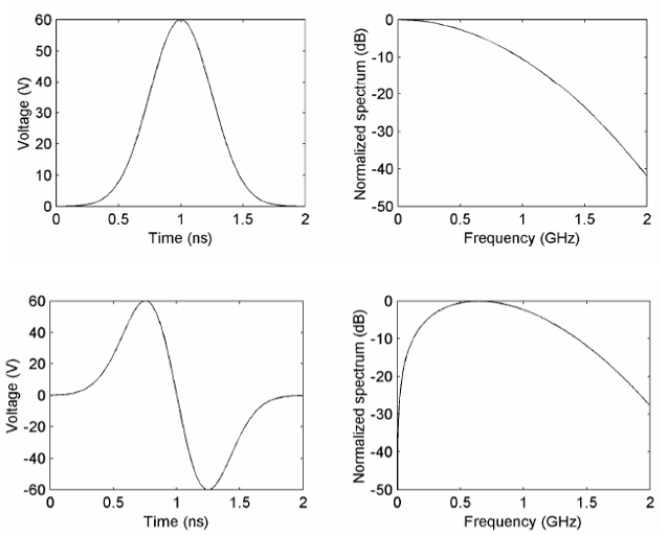

Figure 11: *Gaussian pulse (top) and Differentiated Gaussian pulse (bottom) with their respective spectrum* [16].

- When the system has to be analysed at *a single frequency*, sinusoid input is used. In order to obtain the sinusoidal signal in the FDTD simulation a starting point have to be defined, which is equivalent to the product of the sinusoidal function for the step function. The spectrum of the obtained function is characterized by the presence of spurious frequency around the frequency of interest. To avoid introducing energy at surrounded frequencies, the *erf function* is used (Figure 12) and from the sigmoid function, the *Ramped Sinusoid impulse* is obtained defined as:

$$\frac{\operatorname{erf}\left(\frac{\omega t \cdot 4}{2\pi \cdot n_{erf}} - 2\right) + 1}{2} \qquad (2.20)$$

which amplitude is ramped from 0 to 1 over n_{erf} periods (e.g. the Figure .13 reports the function ramped between 0 to 1 over three period) [16].

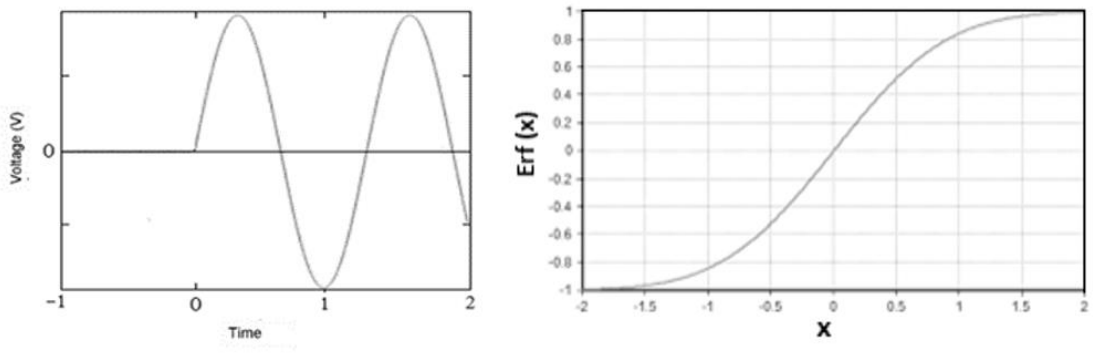

Figure 12: *Sinusoid input started at t=0 (left) erf function (right).*

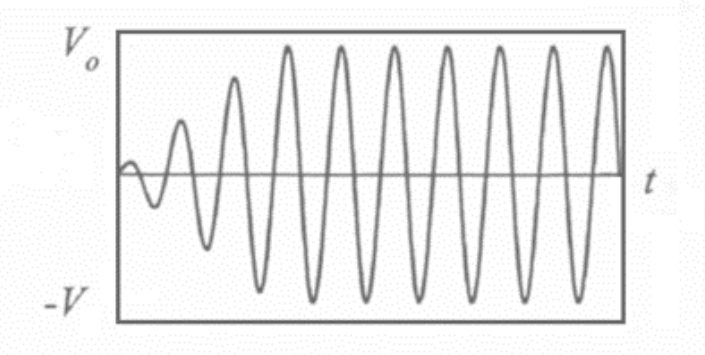

Figure 13: *Ramped sinusoid excitation* [16]

1.3.6 FDTD and antenna analysis

The FDTD method was initially used mainly to model the scattering of electromagnetic waves from objects. Later, after techniques were developed for including sources within the computation lattice, the method started to model radiating structures.

In particular, the impedance of an antenna is calculated at its terminals and is the ratio between voltage and current. These latter have a direct correspondence to the E and H fields which are computed by the FDTD algorithm. FDTD technique provides accurate results, incorporate complex antenna geometries and structures, and can model virtually any type of important material to electromagnetic technology, including conductors, dielectric, anisotropic media, and dispersive and nonlinear materials. The FDTD method yields near-field details and gives model details across a broad frequency spectrum in a single FDTD run.

The application of FDTD to antennas problems provides a powerful and accurate tool to explore critical design issues and no better results have been achieved using any other theoretical or numerical techniques [30].

1.3.7 Phantom models of the human body

As previously said, numerical modelling provides an effective way of assessing and predicting the EM performance of biomedical telemetry systems in terms of radiation, propagation, and interaction with body tissues. To obtain more accurate simulation results, it is necessary to use realistically shaped numerical phantoms consisting of several types of tissues, known as anatomical models [1].

The human body (or parts of it) is modelled by cubic cells (voxels) in which tissue electrical properties (relative permittivity and conductivity) are considered constant. The corresponding electrical properties are later assigned to each voxel to model the anatomical tissues and organs and to obtain standardized models of the human body that are employed to describe and predict the radiation doses received by various tissues in the body [34].

Early models representing the human body were mostly homogeneous slabs, cylinders, and spheres obtained through mathematical functions or by digital (voxel-based) volume arrays. However, realistically designed complex human anatomy models cannot be obtained with mathematical models due to difficulties in representing anatomical details with a limited set of equations. Thus, new models with higher spatial resolution were needed which were achieved by the progress in medical imaging technologies and the increase in computing power that was allowed the development of more and more detailed anatomical structures.

Data for designing the anatomical body models are taken from magnetic resonance imaging (MRI) or computed tomography (CT) scans which provide grey-scale image data of the human body at several transverse slices at a designated spacing. The resolution in each slice is on the order of millimetres and several tissues can be distinguished. Nevertheless, image segmentation is further required to convert the density mappings into tissue maps, which is generally a complex a time-consuming activity [1].

Another consideration regards the development of anatomical models of younger people. Due to the lack of children images, the first anatomical children's models in the literature were based on uniform downscaling of adult models. Even if this approach is easier to apply does not consider the different growth patterns of certain parts of the body. However, a child's head is not a reduced adult head.

To overcome these limitations and since only a few magnetic resonance imaging (MRI)-based models were available, other studies were performed with child head models based on adult head models downscaled through a nonuniform downsizing taking into account the variation of the head shape with age.

Only recently, whole-body child models have been developed based on MRI or CT databases of children. In 2008 several MRI data sets of children at different ages taken from different hospitals were used by Wiart [35] to provide segmented versions of children's head models. Six child head models at different ages (5, 6, 8, 9, 12, and 15 years old) were built using this approach.

In contemporary models, the highest complexity used for modelling the whole human body is about 50 tissue types, and the finest resolution is about 1mm; advanced computer graphics techniques can be employed to pose such models in virtually any position.
The most famous phantom file of a human body is the 67-biological-tissue Voxel-Man Phantom produced at Yale University by Dr. Zubal in1994. This original phantom was complete only from head-to-torso, and was designed specifically for improving nuclear medicine [36].

1.4 Specific absorption rate (SAR)

From a RF electromagnetic point of view the body can be seen as a lossy, dielectric object with magnetic permeability equal to that of free space. At a microwave and radio frequencies, electromagnetic fields penetrate into the human body and interact with the biological tissue in several ways, the most important of which can be explained in terms of energy transfer from the electromagnetic field to the tissue material. A quantity usually used to describe the electromagnetic field interaction with biological tissue, is the specific absorption rate (SAR) [37].
The SAR value - defined by the International Electrotechnical Commission (IEC) standard as units of power per mass of tissue (W/kg) - is the measure of the rate at which energy is absorbed per unit mass by a human body, or by a small sample volume, when exposed to a radio frequency (RF) electromagnetic field [38].
When human body is exposed to low frequency (1Hz - 100KHz) electromagnetic waves, the current induced in the body irradiates the nerves. Exposure to high frequency (100Hz – 10GHz) electromagnetic wave instead, such as the one emitted by mobile phones, causes heating reaction, thus capable to increase body temperature. SAR represents the current national and international dosimetry term used to characterize the thermogenic aspects of the electromagnetic field and also to provide an indirect quantitative measure of RF energy to ensure that they meet the safety recommendation guidelines set by FCC and CENELEC [39].
The SAR is formally defined as the time derivative of the incremental energy absorbed by (dissipated in) an incremental mass contained in a volume of a given density. While at a particular point in the tissue material it is related to electric fields by [40]:

$$SAR = \frac{\sigma |E|^2}{\rho} \qquad (3.1)$$

where $\sigma\ and\ \rho$ are, respectively, the sample electrical conductivity (S/m) and the sample density (kg/m^3) and E is the effective value of the electric field induced in the body.

Through this definition, is possible to see that the SAR is an appropriate indirect non-thermal measure for the interaction of electromagnetic fields with human tissue because it is directly related to the fields inside the body. This statement is valid under the assumption that any biological effects (thermal or non-thermal) are related directly to the internal electric field. Moreover, SAR does not measure the emission from a source of electromagnetic energy but rather evaluate the power absorbed by a spatial region (sample volume) exposed to the emission of the source.

A more practical quantity for biological interaction considerations is the average SAR, which is obtained from (1.1) by integrating over the entire exposed volume V of the body or body part under consideration[37]:

$$SAR = \frac{1}{V}\int_{sample} \frac{\sigma(r)\left|\vec{E}(\vec{r})\right|^2}{\rho(r)}\mathrm{d}r \qquad (3.2)$$

Since the tissue of the human body are very different from each other for geometric characteristic as well as for density, SAR values will not be uniform over the entire region in which the power emitted by the electromagnetic field will be absorbed but will change significantly between one tissue and another [38].

SAR value is directly proportional to the electrical conductivity of the material under examination, and therefore, strictly depends on the geometric characteristic of the part of the body involved in the emission of the electromagnetic waves. In fact, the electrical conductivity is described as the electrical resistance of the material multiply for the ratio of the cross-sectional area and length of the section considered, and so dependent on the geometry of the specimen.

In addition, SAR is directly proportional to the Root Mean Square of the intensity of the electric field and inversely proportional to the density of the material that the field radiates [39]. There are other parameters that can influence the SAR value:

- the incident field characteristics, which are intensity, frequency, polarization and configuration of the irradiated subject and conditions of the near and far field.
- SAR distribution varies with the antenna location on the body.
- The dielectric properties of the various tissue's thicknesses and the reflection of other objects present in the irradiation field.

SAR testing uses standardized models of the human head and body that are filled with liquids that simulate the RF absorption characteristics of the different human tissues. The simulations must include the most severe, worst-case (and highest power) operating conditions for all the frequency bands used, thus SAR values reported for the devices tend to significantly overstate real-life exposure levels. Standard approval means that the device will never exceed the maximum level of consumer RF exposure permitted by the safety guidelines, but it does not indicate the amount of RF exposure during the normal use of the device. In dosimetry studies, the SAR is treated as a linear quantity. The SARs obtained at high intensities and short exposures can be extrapolated to low-power exposure. Because the thresholds for biological effects maybe frequency and modulation dependent, these parameters must also be specified in addition to the SAR data [40].

1.4.1 Types of SAR calculations

The calculation of the specific absorption rate is not a unique procedure but can be performed in different conditions. Considering the human exposure to RF fields, the most important SAR quantities are [40]:

- The *whole-body average* SAR analysed on the whole human body –is used as basic restriction for far-field RF exposure by various regulatory bodies and is the quantity that must be evaluated when considering limiting exposure.
- The *body-part* or *organ-average* SAR – the SAR analysed on specific anatomical parts – is evaluated when considering the exposure to a far-field source, with respect to precise areas and especially when considering a near or intermediate field source and the body partially exposed.
- The *local-average* SAR is evaluated when the RF source is in very close proximity to the body, and so considering the exposure of a specific part of the body to a near-field source. So, it can be defined as the average SAR in a specified volume or mass of finite extent in the exposed body, body part or sub-body part.

Related to local-average-SAR is:

- The *punctual SAR* calculates the rate of each single Yee cell contained in the computation space.

- The *averaged SAR* instead calculates the average absorption rate of a set of Yee cells such as to reach the total weight of 1 gram (SAR averaged over 1 gram) or 10 grams (SAR averaged over 10 grams) and it is done for each group of contiguous cells belonging to the examined space.
- And the *averaged spatial peak* SAR: this quantity is just the maximum (or peak) local-average-SAR in an exposed body. The averaged spatial peak SAR is obtained by evaluating the local SAR at different spatial positions in the exposed body and recording the position and value where the local-average-SAR peaks.

The necessity to use local-average-SAR as a measure of field-tissue interaction originates from the highly non-uniform exposure, and associated non-uniform energy absorption, that results from partial body exposure. The maximum allowable local-average-SAR is much higher than the maximum allowable whole-body SAR due to the body capability to act like a heat-sink, absorbing the energy locally but compensating for the local temperature rise by distributing the heat throughout the body - using thermoregulatory mechanisms, such as blood flow [41].

1.4.2 Dosimetry

Radio waves in free space are characterized by the frequency, intensity of the electric (E) and magnetic (H) fields, their direction, and orientation. However, only the electromagnetic fields inside the tissues can interact with biological systems, and therefore it is necessary to determine these fields for any meaningful and general quantification of biological data obtained experimentally.
Dosimetry - defined as the measure or quantification of energy absorbed in the human body due to exposure to radiofrequency electromagnetic fields - attempt to quantify these interactions [41].
This word derives from the dosimetric concept where the dose is the energy per unit mass and in bioelectromagnetic research has been developing in two parallel but interacting and complementary streams: theoretical and experimental [38].

1.4.2.1 Theoretical Dosimetry

Theoretical dosimetry deals with the predictions of whole body and localized SAR distributions in complex models that are close approximations of the actual human or animals by mathematical methods. Theoretical dosimetry is the identification of the dependence of predicted SAR in relation

to the variability in permittivity values for different tissue types (muscle, fat, skin, bone, marrow) when using different numerical anatomical models. Whole body SAR is not particular sensitive to variations in permittivity values, while localized SAR values have a great dependence on them.
Since the interactions between permittivity and predicted SAR values in different anatomical models are very complex, there is no universal approach to predicting the relative influence on SAR values. Thus, the relationship between permittivity values and SAR for each case (anatomical model, orientation, frequency, tissue type, voxel size) must be evaluated. The development of theoretical dosimetry modelling techniques and powerful computer hardware represents the principal tool in determining EMF exposure and the estimation of energy absorption values in tissue material using numerical simulation technique is defined as numerical dosimetry [38].

1.4.2.2 Experimental Dosimetry

Experimental dosimetry concerns the development of methods and instruments suitable for measurements of the internal electric fields, whole body or localized SAR values, or related variables. Carefully performed experiments are crucial in verification of theoretical predictions and delineation of their limitations. The disparity between the empirical and theoretical methods is greater when predicted localized SAR values are very different ("hot or cold" spots) from whole body average SAR and when using heterogeneous digital anatomical models.
Furthermore, this incongruity reflects the fact that SAR alone does not provide an adequate description of the regional thermal environment and does not account for the thermoregulatory parameters (convection by blood flow, and conduction) [38].
Overall, the two approaches (theoretical and empirical) to RF dosimetry are complementary, and as both have certain advantages and limitations, these should be considered in selecting one or the other or both approaches to solve a certain dosimetric problem.

1.4.3 Regulations

The Regulators that define the limits of exposure to electromagnetic fields vary in different parts of the world. Currently, several international safety committees have developed exposure guidelines to time-varying electric, magnetic and electromagnetic fields: the International Commission on Non-Ionizing Radiation Protection (ICNIRP), European Committee for Electrotechnical Standardization (CENELEC) and the Federal Communications Commission (FCC) [42][43].

All of the safety guidelines are based on a detailed assessment of the available scientific evidence and will provide knowledges and protection against adverse health effect due to EMG exposure.

- The International Commission on Non-Ionizing Radiation Protection (ICNIRP) is an independent committee of scientific experts established in the European Union to evaluate the state of knowledge and guidance on protection against adverse effects of non-ionizing radiation (NIR) on human health and on the environment [42].
- The Federal Communications Commission (FCC) is an independent agency of the United States federal government that regulates communications by radio, television, wire, satellite, and cable across the United States. While CENELEC (European Committee for Electrotechnical Standardization) is responsible for European standardization in the area of electrical engineering. They adopted guidelines for evaluating human exposure to RF fields using the specific absorption rate (SAR) limits for transmitting devices operating within close proximity to the body [44][45].

The FCC limit for public exposure from cellular handsets is an SAR level of 1.6 watts per kilogram (1.6 W/kg). This limit that needs to meet the FCC's RF exposure standard are set below the level of radiation that at which the laboratory testing indicates and that would endanger a user's health [44].
CENELEC specify SAR limits within the EU for mobile phones, and other such hand-held devices of 2 W/kg which is calculated over a period of 6 minutes and averaged over 10 grams of tissue absorbing the most signal.
ICNIRP instead, specify basic restriction of:

- 0.08 W/kg for a period of 30 min over the whole-body average.
- 2 W/kg for a period of 6 min averaged over 10 grams if the measure is referred to head and torso.
- 4.0 W/kg for a period of 6 min averaged over 10 grams if the measure is referred to limbs.

All these guidelines are developed using worst-case scenarios and include added safety margins to ensure everyone in the community including the elderly, children or pregnant women are protected.

1.5 Electrical Properties of Tissues and Cole-Cole Equation

Dielectric properties are intrinsic parameter that determine the effects of electromagnetic (EM) fields on human tissues. They represent an important theoretical aspect in dosimetry studies, in particular when deals with digitized 2D or 3D human models, in which each element has to be recognized as being constituted by a given, well defined tissue with unique dielectric properties, consisting of a pair of values, one for the relative permittivity and one for the electrical conductivity at each frequency of interest [46].

1.5.1 Overview of dielectric properties: terms and definitions

The most important effect arising from the interaction of an electric field with a dielectric material is polarization; a phenomenon that occurs when internal charge in the material moves in response to an external electric field. Molecules with permanent, induced, or transient induced dipoles exhibit their own specific polarization. The effect of an electric field is twofold: to trigger several polarization mechanisms, each governed by its own time constants, and to cause ionic drift.
The net result is the establishment of both displacement and conduction currents. For this reason, biological materials are classified as lossy dielectric materials[46].
At any time, the total polarization is the vector sum of all contributions such as:

$$P = \sum_{i}^{n} P_i \qquad (4.1)$$

The polarization P is related to the dielectric displacement D, the internal electric field strength E and the dielectric properties as follows:

$$D = \varepsilon_0 E + P \qquad (4.2)$$

where ε is the permittivity of the medium and ε_0 is the permittivity of the free space. From this expression, the dependence of P on E can be defined as:

$$P = \varepsilon_0(\varepsilon - 1)E \qquad (4.4)$$

which describe the polarisation P as a material-specific displacement vector and the medium permittivity as:

$$\varepsilon = \frac{P}{\varepsilon_0 E} + 1 \qquad (4.5)$$

Since the relative permittivity can be a tensor, a complex parameter or simply a real number depending on the directionality of the response and the phase difference between the displacement vector and the electric field. Assuming a linear isotropic behaviour, the relative permittivity of biological materials ε^* is a complex parameter expressed as follows:

$$\varepsilon^* = \varepsilon' - j\varepsilon'' \qquad (3.6)$$

where ε' is the real part and determines the component of the displacement current which is out-of-phase with the driving field, while the imaginary part ε''relates to the in-phase or power loss component and is referred to as loss factor [46].

Considering displacement and ionic currents, a biological material is characterized by an effective loss factor defined as:

$$\varepsilon'' = \frac{\sigma}{\omega\varepsilon_0} \qquad (4.7)$$

where σ is the total conductivity of the material which, depending on the nature of the sample and ω the angular frequency of the field. The SI unit of conductivity is siemens per metre ($S \cdot m^{-1}$) which presumes that in the above expression ε_0 is expressed in farads per metre ($F \cdot m^{-1}$) and ω in radians per second. So, the electrical properties of tissues can be present in terms of complex dielectric permittivity defined as *effective complex relative dielectric permittivity*:

$$\varepsilon^*_{r_{eff}}(\omega) = \varepsilon'_r(\omega) - j\left(\varepsilon''_r(\omega) + \frac{\sigma_{dc}}{\omega\varepsilon_0}\right) = \varepsilon'_r(\omega) - j\left(\frac{\sigma_{ac}(\omega) + \sigma_{dc}}{\omega\varepsilon_0}\right) \qquad (4.8)$$

and the *electrical conductivity* of the medium is identified by the following quantity:

$$\sigma(\omega) = \sigma_{ac}(\omega) + \sigma_{dc} = \omega\varepsilon_0\varepsilon''_r(\omega) + \sigma_{dc} \qquad (4.9)$$

where σ_{dc} (continuous) which represents the ohmic conductivity deriving from the mobility of the ionic species present in a specific tissue and σ_{ac} (alternating) which represent losses due to dielectric relaxation. [47][48]

The dielectric properties of a biological tissue result from the interaction of electromagnetic radiation with its constituents at the cellular and molecular level.

The main features of the dielectric spectrum of a biological tissue are:

- The relative permittivity of a tissue may reach values of up to 10^6 or 10^7 at frequencies below 100 Hz.
- It decreases at high frequencies in three main interaction mechanism known as the α, β and γ dispersions.
- Tissues have finite ionic conductivities commensurate with the nature and extent of their ionic content and ionic mobility

The *γ dispersion*, in the microwave frequency region (frequencies greater than 1 GHz), is due to the polarization of water molecules which present permanent dipoles that are casual oriented when there is the absence of the external field, while field-oriented when the external field is applied.
The *β dispersion*, in the radio frequency region (from 20 kHz to around 300 GHz), is due mainly to the polarization of cellular membranes which act as barriers to the flow of ions between the intra and extra cellular media. Other contributions to the β dispersion come from the polarization of protein and other organic macromolecules.
The low frequency *α dispersion* (below 10 kHz) is associated with ionic diffusion processes at the site of the cellular membrane[46].
In its simplest form, each dispersion is characterized by a single time constant τ (*dielectric relaxation constant*) and exhibits the following frequency dependence:

$$\varepsilon_r^* = \varepsilon_\infty + \frac{\varepsilon_s - \varepsilon_\infty}{1 + j\omega\tau} \qquad (4.10)$$

This expression is the *Debye equation* in which ε_∞ is the permittivity at field frequencies where $\omega\tau \gg 1$, and ε_s the permittivity at $\omega\tau \ll 1$. The magnitude of the dispersion is described as $\Delta\varepsilon = \varepsilon_s - \varepsilon_\infty$.
In most biological tissues there are more polarization phenomena and each one is characterized by its own relaxation time. The presence of this several mechanisms with relaxation times distributed around τ can be described in terms of a deviation from Debye behaviour, defined as *semi-empirical expression of Cole-Cole equation* and expressed as:

$$\varepsilon_r^*(\omega) = \varepsilon_\infty + \frac{\Delta\varepsilon}{1 + (j\omega\tau)^{(1-\alpha)}} \qquad (4.11)$$

in which the α parameter is introduced to describe the broadening of the dispersion.
The spectrum of a tissue can be described mathematically in terms of multiple Cole-Cole dispersion and ionic conductivity σ_{dc} such that [46]:

$$\varepsilon_r^*(\omega) = \varepsilon_\infty + \sum_n \frac{\Delta\varepsilon_n}{1 + (j\omega\tau_n)^{(1-\alpha_n)}} + \frac{\sigma_{dc}}{j\omega\varepsilon_0} \qquad (4.12)$$

which, with a choice of parameters appropriate to each tissue, can be used to predict the dielectric behaviour over the desired frequency range.

1.6 Aim of the study

Wearable devices represent at the same time a huge market potential and an interesting research topic due to the remarkable growth of consumers' interaction with this technology in everyday life.
From sport to health care, wearable systems with embedded sensors - such as smartwatches, headphones, garments, and heart rate monitors (HRM) – allow to monitor different physical parameters during several daily activities and thus improve personal health.

The majority of electromagnetic studies on HRM devices did not focus the research subject on the specific types of smart wearable devices but instead try to determine the accuracy of these devices and if they can be compared to the ones used for standard measurements. As electromagnetic external sources, they continuously emit a small amount of EMF radiations in the proximity of the human body [49], thus they need to be analysed in order to verify if their exposure-induced biological effects are within the International Commission on Non-Ionizing Radiation Protection (ICNIRP) guidelines.

Thus, the purpose of this study is the electromagnetic characterization, through FDTD simulation, of the interaction between a real heart rate monitor device and human tissues.
The use of the FDTD method allows to simulate the field distribution generated by the device's inverted-F antenna and to determine the dissipated power on the high-resolution virtual body model in terms of SAR values.

2. Materials and methods

For this work, a real heart rate monitor (HRM) has been found in the literature and through FDTD simulation its interaction with the human body has been studied.

In order to understand the methods that have been applied, a summary block diagram has been created which describe in detail the process used (Figure 14): the light orange rectangles represent the procedure applied to obtain the virtual human body model, while the light blue ones the procedure followed to design the model of the real inverted-F antenna (IFA). For both the processes the first step is the *Model Choice*; for the human model, the choice depends on the spatial resolution of the map whereas for the antenna, the selection takes a bit longer time since the real device found in the literature must also include all the hardware components with the presence of an antenna. Once the human body and antenna model has been chosen the next step involves the use of the FDTD algorithm to simulate the generated field by the antenna isolated (*Test simulation*) and in an embedded condition (*Final simulation*).

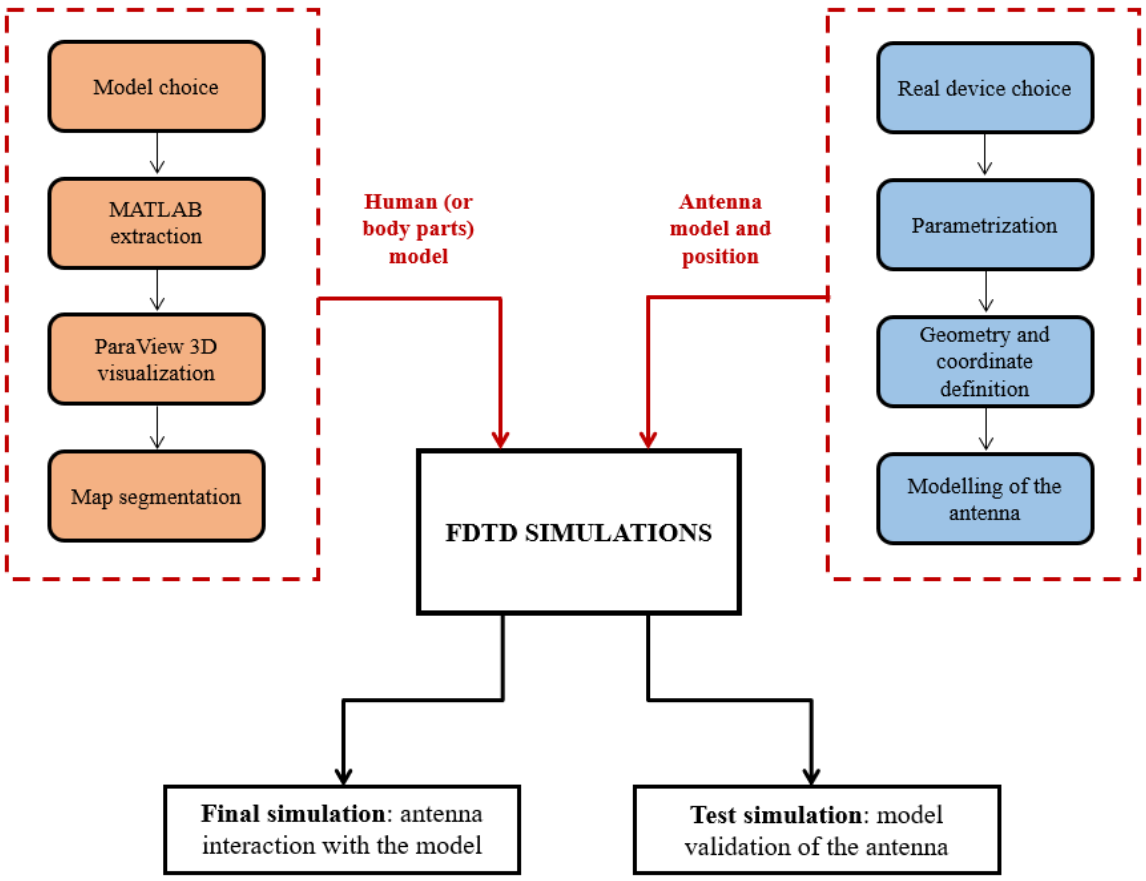

Figure 14: *Methods Block Diagram*

2.1 Human body model design

The virtual human body model used in the simulation has been taken from the first generation (V1.0) of detailed whole-body virtual models developed by the Foundation for Research on Information Technologies in Society (IT'IS).

IT'IS is a Swiss research foundation that creates body models from magnetic resonance image data of volunteers in order to perform electromagnetic exposure evaluations. There are different types of virtual family models: V1.x, V2.x, V3.x and V4.x.

- The V1.x is the first generation of models that is characterized by an high level of detail and accuracy with a spatial resolution of 1.0x1.0x1.0 mm^3.
- V2.x models are a simplified version in which approximately 300 tissues are combined into 22 tissue groups (identical in all the four maps, except for the reproductive system, which is gender-specific). The simplification involves the tissue number, but not the tissue resolution (the whole-body cell count ranges between 3.6 - 7.7 million cells).
- V3.x is the high-resolution generation of human models. Each including more than 300 anatomical features, a re-segmentation at higher resolution (0.5 × 0.5 × 0.5 mm^3) and an enhanced surface processing method. V3.x are static models and so their posture cannot be modified.
- V4.x is based on the V3.x generation of models. They include more than 1000 anatomical features, and the segmentation is performed at an increased resolution (01 x 0.1 x 0.2 mm) allowing for more detail in objects and segmentation of small structures. The higher resolution yields an extended cardiovascular system and a peripheral nerve network (from the cranium and spinal cord to internal organs and major muscles). Muscles, nerves, and blood vessels have been named and meshed as separate objects.

The DVD with the Virtual Family V1.0 includes both the CAD and voxel format compatible with different simulation platforms. For the study simulation, which involves the use of an FDTD algorithm software, only the voxel models (.raw) are required since the CAD files are used to study different exposure configurations using posture simulation platforms.
The whole-body human models include four subjects of study: Duke, Ella, Billie and Thelonious (Table 1).

Table 1: *General information about V1.0 human models*

General information	Sex	Type	Age [Years]	Height [m]	Weight [kg]
Thelonious	male	Child	6	1.16	18.6
Billie	female	Pre-teenager	11	1.49	34
Ella	female	young adult	26	1.63	57.3
Duke	male	Young adult	34	1.77	70.2

Together with the RAW file, a file text containing all the necessary information relating to the model has been found with the specific tissue identification number, the cells' spatial resolution and the number of the cell in x, y, and z coordinates which define the total dimensions of the file.

Eventually, from the section "*tissue properties*" of the IT'IS webpage, it's possible to download other information files, in particular, an excel file with the thermal and dielectric properties of the various tissues (*Table 1*), an explanatory notes file and a database on tissue morphometry.

Since the list order of the tissues in the text file for the different human models is not the same, to use the general dielectric properties reported in Table 2, another file has been created with the correspondences with respect to the tissues of each map; this file has been used as a pointer vector during the FDTD simulation to read and used the respective tissues dielectric parameter in the Cole-Cole equation.

Table 2: *Dielectric properties of V1.0 tissues*

Tissue	Dielectric Properties													
Name	ε_0	$\Delta\varepsilon_1$	τ_1 (ms)	α_1	$\Delta\varepsilon_2$	τ_2 (ms)	α_2	σ (S/m)	$\Delta\varepsilon_3$	τ_3 (µs)	α_3	$\Delta\varepsilon_4$	τ_4 (ms)	α_4
Adrenal Gland	4	55	7,958	0,1	2500	159,155	0,1	0,5	100000	159,155	0,2	40000000	15,915	0
Air	1	0	0	0	0	0	0	0	0	0	0	0	0	0
Bile	4	66	7,579	0,05	50	1,592	0	1,4	0	159,155	0,2	0	15,915	0,2
Blood	4	56	8,377	0,1	5200	132,629	0,1	0,7	0	159,155	0,2	0	15,915	0
Blood Vessel Wall	4	40	8,842	0,1	50	3,183	0,1	0,25	100000	159,155	0,2	10000000	1,592	0
Bone	2,5	10	13,263	0,2	180	79,577	0,2	0,02	5000	159,155	0,2	100000	15,915	0
Bone (Cancellous)	2,5	18	13,263	0,22	300	79,577	0,25	0,07	20000	159,155	0,2	20000000	15,915	0
Bone (Cortical)	2,5	10	13,263	0,2	180	79,577	0,2	0,02	5000	159,155	0,2	100000	15,915	0
Bone Marrow (Red)	2,5	9	14,469	0,2	80	15,915	0,1	0,1	10000	1591,549	0,1	2000000	15,915	0,1
Bone Marrow (Yellow)	2,5	3	7,958	0,2	25	15,915	0,1	0,0005	5000	1591,549	0,1	2000000	15,915	0,1
Brain	4	40	7,958	0,1	700	15,915	0,15	0,04	200000	106,103	0,22	45000000	5,305	0
Brain (Grey Matter)	4	45	7,958	0,1	400	15,915	0,15	0,02	200000	106,103	0,22	45000000	5,305	0
Brain (White Matter)	4	32	7,958	0,1	100	7,958	0,1	0,02	40000	53,052	0,3	35000000	7,958	0,02
Breast Fat	2,5	3	17,68	0,1	15	63,66	0,1	0,01	50000	454,7	0,1	20000000	13,26	0
Breast Gland	4	55	7,958	0,1	2500	159,155	0,1	0,5	100000	159,155	0,2	40000000	15,915	0
Bronchi	2,5	38	7,958	0,1	400	63,662	0,1	0,3	50000	15,915	0,2	1000000	15,915	0
Bronchi lumen	1	0	0	0	0	0	0	0	0	0	0	0	0	0
Cartilage	4	38	13,263	0,15	2500	144,686	0,15	0,15	100000	318,31	0,1	40000000	15,915	0
Cerebellum	4	40	7,958	0,1	700	15,915	0,15	0,04	200000	106,103	0,22	45000000	5,305	0

Cerebrospinal Fluid	4	65	7,958	0,1	40	1,592	0	2	0	159,155	0	0	15,915	0
Cervix	4	45	7,958	0,1	200	15,915	0,1	0,3	150000	106,103	0,18	40000000	1,592	0
Commissural Anterior	4	32	7,958	0,1	100	7,958	0,1	0,02	40000	53,052	0,3	35000000	7,958	0,02
Commissural Posterior	4	32	7,958	0,1	100	7,958	0,1	0,02	40000	53,052	0,3	35000000	7,958	0,02
Connective Tissue	4	42	12,243	0,1	60	6,366	0,1	0,25	60000	318,31	0,22	20000000	1,326	0
Diaphragm	4	50	7,234	0,1	7000	353,678	0,1	0,2	1200000	318,31	0,1	25000000	2,274	0
Ductus Deferens	4	40	8,842	0,1	50	3,183	0,1	0,25	100000	159,155	0,2	10000000	1,592	0
Dura	4	40	7,958	0,15	200	7,958	0,1	0,5	10000	159,155	0,2	1000000	15,915	0
Epididymis	4	55	7,958	0,1	5000	159,155	0,1	0,4	100000	159,155	0,2	40000000	15,915	0
Esophagus	4	60	7,958	0,1	2000	79,577	0,1	0,5	100000	159,155	0,2	40000000	15,915	0
Esophagus Lumen	1	0	0	0	0	0	0	0	0	0	0	0	0	0
Eye (Cornea)	4	48	7,958	0,1	4000	159,155	0,05	0,4	100000	15,915	0,2	40000000	15,915	0
Eye (Lens)	3	32	8,842	0,1	100	10,61	0,2	0,2	1000	15,915	0,2	5000	15,915	0
Eye (Sclera)	4	50	7,958	0,1	4000	159,155	0,1	0,5	100000	159,155	0,2	5000000	15,915	0
Eye (Vitrous Humor)	4	65	7,234	0	30	159,155	0,1	1,5	0	159,155	0	0	15,915	0
Eye Lens (Cortex)	4	42	7,958	0,1	1500	79,577	0,1	0,3	200000	159,155	0,1	40000000	15,915	0
Eye Lens (Nucleus)	3	32	8,842	0,1	100	10,61	0,2	0,2	1000	15,915	0,2	5000	15,915	0
Fat	380	0	1	380	380	5,89	0,00	1	5,89	5,89	4	50	7,958	0,1
Fat (Average Infiltrated)	0	0	1	0	0	0,00	0,00	1	0,00	0,00	4	65	7,234	0
Fat (Not Infiltrated)	0	0	1	0	0	0,00	0,00	1	0,00	0,00	4	42	7,958	0,1
Gallbladder	0	0	1	0	0	0,00	0,00	1	0,00	0,00	3	32	8,842	0,1
Heart Lumen	33	13	12	20	63	0,51	0,20	12	0,31	0,98	2,5	9	7,958	0,2
Heart Muscle	33	13	12	20	63	0,51	0,20	12	0,31	0,98	2,5	9	7,958	0,2
Hippocampus	0	0	1	0	0	0,00	0,00	1	0,00	0,00	2,5	3	7,958	0,2
Hypophysis	30	0	1	30	30	0,46	0,00	1	0,46	0,46	4	55	7,579	0,05
Hypothalamus	10000	0	1	10000	10000	0,00	0,00	1	0,00	0,00	4	56	8,377	0,1
Intervertebral Disc	1024	310	24	609	1719	39,36	11,92	24	23,42	66,08	4	50	7,958	0,1
Kidney	763	86	3	670	840	15,53	1,75	3	13,63	17,09	4	45	7,958	0,1
Kidney (Cortex)	885	304	2	670	1100	13,71	4,71	2	10,38	17,04	4	55	7,958	0,1
Kidney (Medulla)	885	0	1	885	885	18,01	0,00	1	18,01	18,01	4	55	7,958	0,1
Large Intestine	35	0	1	35	35	0,54	0,00	1	0,54	0,54	4	38	13,263	0,15
Large Intestine Lumen	4161	541	43	2607	5571	19,79	2,57	43	12,40	26,50	4	47	7,958	0,1
Larynx	3953	914	8	2750	5060	18,80	4,35	8	13,08	24,07	4	47	7,958	0,1
Liver	599	191	4	350	770	2,85	0,91	4	1,66	3,66	4	47	7,958	0,1
Lung	765	232	20	335	1236	11,85	3,59	20	5,19	19,14	4	50	7,958	0,1
Lung (Deflated)	0	0	1	0	0	0,00	0,00	1	0,00	0,00	4	50	7,234	0,1
Lung (Inflated)	35	0	1	35	35	0,54	0,00	1	0,54	0,54	4	38	13,263	0,15
Lymphnode	902	228	43	212	1273	10,41	2,63	43	2,45	14,69	4	39	8,842	0,1
Mandible	401	358	8	71	1083	6,21	5,55	8	1,10	16,78	2,5	18	7,958	0,1
Medulla Oblangata	401	358	8	71	1083	6,21	5,55	8	1,10	16,78	4	45	7,958	0,1
Meniscus	401	358	8	71	1083	6,21	5,55	8	1,10	16,78	2,5	18	7,958	0,1
Midbrain	453	49	3	402	500	7,01	0,76	3	6,23	7,74	4	55	7,958	0,1
Mucous Membrane	10	0	1	10	10	0,15	0,00	1	0,15	0,15	2,5	10	13,263	0,2
Muscle	559	99	43	412	976	11,37	2,01	43	8,37	19,87	4	40	7,958	0,1
Nerve	35	0	1	35	35	0,54	0,00	1	0,54	0,54	4	38	13,263	0,15
Ovary	559	99	43	412	976	11,37	2,01	43	8,37	19,87	4	40	7,958	0,1
Pancreas	594	497	3	270	1166	9,19	7,70	3	4,18	18,06	4	39	7,958	0,1
Patella	39	13	43	19	94	0,96	0,32	43	0,46	2,32	4	50	7,234	0,1

Penis	160	30	3	130	189	2,48	0,46	3	2,01	2,93	4	26	7,958	0,1
Pharynx	236	0	1	236	236	3,65	0,00	1	3,65	3,65	4	40	8,842	0,15
Pineal Body	767	357	13	469	1640	11,89	5,53	13	7,26	25,40	4	55	7,958	0,1
Placenta	10	0	1	10	10	0,15	0,00	1	0,15	0,15	2,5	10	13,263	0,2
Pons	12	5	3	7	16	0,19	0,07	3	0,11	0,25	4	40	8,842	0,1
Prostate	0	0	1	0	0	0,00	0,00	1	0,00	0,00	1	0	0	0
Salivary Gland	885	304	2	670	1100	13,71	4,71	2	10,38	17,04	4	55	7,958	0,1
SAT (Subcutaneous Fat)	1700	423	3	1250	2090	26,33	6,55	3	19,36	32,37	4	56	8,377	0,1
Seminal vesicle	559	99	43	412	976	11,37	2,01	43	8,37	19,87	4	40	7,958	0,1
Skin	394	0	1	394	394	6,10	0,00	1	6,10	6,10	4	55	7,958	0,1
Skull	383	10	3	378	394	5,93	0,15	3	5,85	6,10	4	55	7,958	0,1
Small Intestine	33	13	12	20	63	0,51	0,20	12	0,31	0,98	2,5	9	7,958	0,2
Small Intestine Lumen	394	0	1	394	394	6,10	0,00	1	6,10	6,10	4	55	7,958	0,1
Spinal Cord	106	37	12	49	175	1,65	0,57	12	0,76	2,70	4	32	7,234	0
Spleen	10	0	1	10	10	0,15	0,00	1	0,15	0,15	2,5	10	13,263	0,2
Stomach	1026	337	11	560	1528	15,89	5,21	11	8,67	23,67	4	50	7,958	0,1
Stomach Lumen	0	0	1	0	0	0,00	0,00	1	0,00	0,00	4	50	7,234	0,1
Tendon\Ligament	160	30	3	130	189	2,48	0,46	3	2,01	2,93	4	26	7,958	0,1
Testis	1557	723	14	931	3600	24,11	11,20	14	14,41	55,75	4	48	7,958	0,1
Thalamus	460	256	8	106	882	7,13	3,96	8	1,64	13,65	4	60	7,958	0,1
Thymus	0	0	1	0	0	0,00	0,00	1	0,00	0,00	4	50	7,234	0,1
Thyroid Gland	29	0	2	29	29	0,45	0,00	2	0,45	0,45	4	42	12,243	0,1
Tongue	200	24	3	186	228	3,09	0,38	3	2,88	3,53	4	55	7,958	0,1
Tooth	685	289	2	480	889	13,93	5,88	2	9,77	18,09	4	45	7,958	0,1
Tooth (Dentine)	243	0	1	243	243	3,76	0,00	1	3,76	3,76	4	55	7,958	0,1
Tooth (Enamel)	5624	1403	7	3350	7370	87,10	21,73	7	51,88	114,14	4	55	7,958	0,1
Trachea	78	0	1	78	78	1,21	0,00	1	1,21	1,21	4	50	7,958	0,1
Trachea Lumen	0	0	1	0	0	0,00	0,00	1	0,00	0,00	2,5	10	13,263	0,2
Ureter\Urethra	0	0	1	0	0	0,00	0,00	1	0,00	0,00	2,5	10	13,263	0,2
Urinary Bladder	0	0	1	0	0	0,00	0,00	1	0,00	0,00	2,5	10	13,263	0,2
Urinary Bladder Wall	35	0	1	35	35	0,54	0,00	1	0,54	0,54	2,5	38	7,958	0,1
Uterus	0	0	1	0	0	0,00	0,00	1	0,00	0,00	1	0	0	0
Vagina	188	0	1	188	188	2,91	0,00	1	2,91	2,91	4	40	8,842	0,1
Vertebrae	39	0	1	39	39	0,60	0,00	1	0,60	0,60	2,5	16	8,842	0,1

2.1.1 MATLAB extraction

The first step to visualize the 3D human model and to eventually segment the different body parts is the correctly extraction of the data, carried out in MATLAB environment through the "*Read Medical Data 3D*" function from Dirk-Jan Kroon. This function allows the user to open medical 3D files of different file format and assign it to an output, using the following command:

[V,info]= ReadData3D('FileDirectory\Filename.raw')

where the variable *V* is the 3D volume and *info* the struct with the information about the data which always includes the following fields:

- Info.Filename : Name of the file.
- Info.Dimensions : Dimensions of Volume.
- Info.PixelDimensions : Size of one pixel / voxel.

The image dimensions equal to the number of the cells in x, y, and z and reported in the text file have to be specified in the pop-up window that appears (Figure 15) in order to match the input file dimensions.

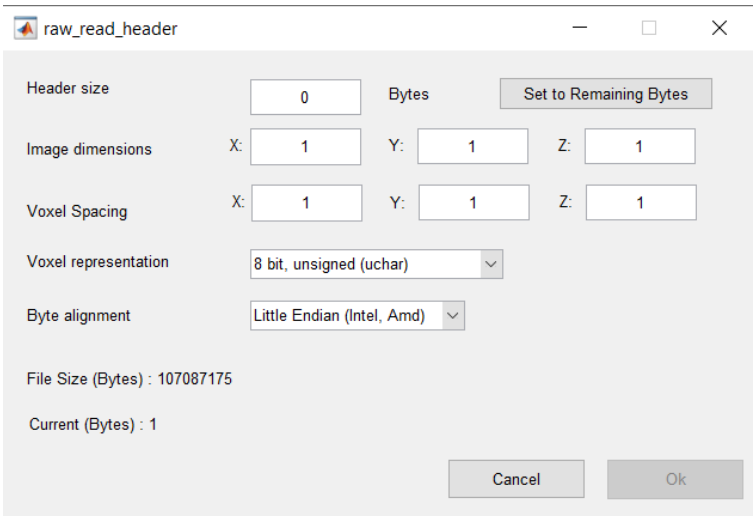

Figure 15: *Pop-up window to read the raw file*

The grayscale slice (Figure 16) of the model can be visualized through the command:

imshow(V(: , : ,1), [ ])

Figure 16: *Grayscale images of head and chest*

Then, to obtain the 3D representation of the model, three for-loops have been implemented, which read the data inside the *V* variable and create a ".vtk" file of x*y*z dimension (where x, y and z correspond to the counter variables of the for-loops). This type of format is compatible with the *ParaView software* for three-dimensional representation.

2.1.2 ParaView Software: body model visualization and segmentation

As previously mentioned, to visualize the model in a 3D space, the ParaView software has been used. ParaView is an open-source, multi-platform data analysis application for interactive, scientific visualization, released in 2002 by Kitware software company. This application is suitable for different kinds of simulations, from academic to research purposes and it's characterized by an intuitive and compact design user interface where all the important tools are located in the main window (Figure 17) [50][51].

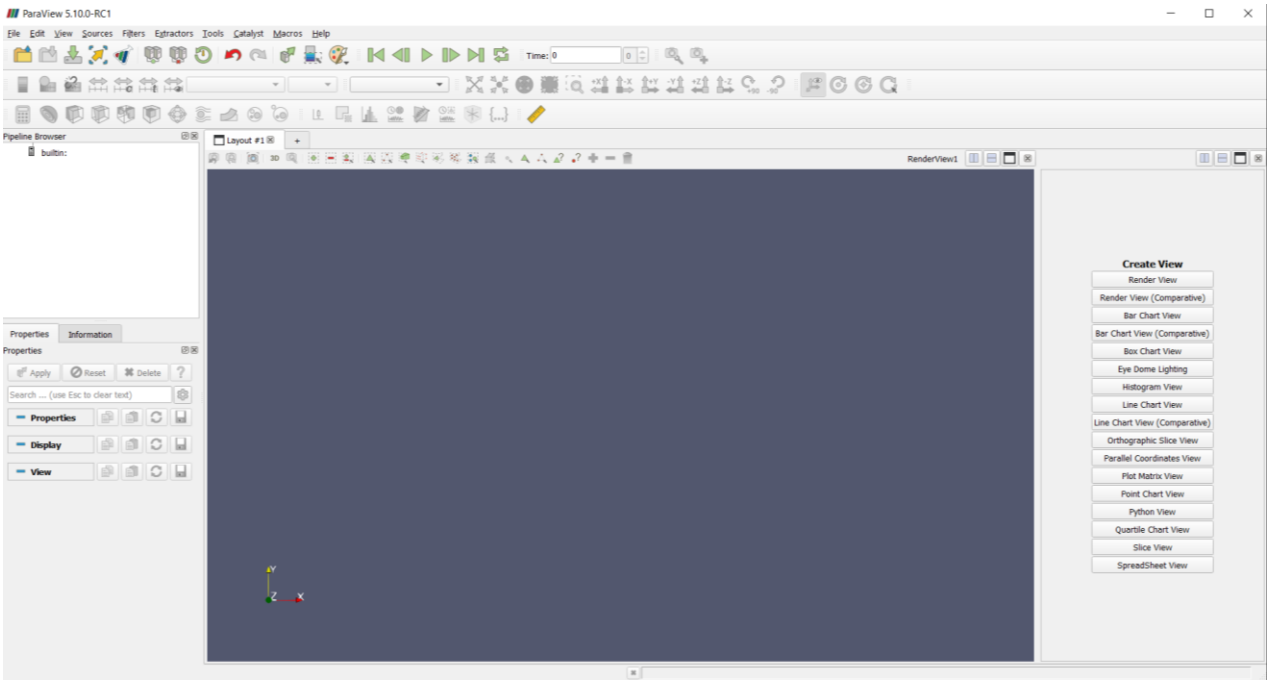

Figure 17: *ParaView user interface*

From here is possible to load the VTK file previously created to visualize the 3D map of the four human models on the three-dimensional coordinate (Figure 18 and 19). On the program is also possible to set different range scale and to change the pre-set for the colour map; with the option "*shade*" and the "*x ray pre-set*" the x ray image can be visualized (Figure 18).

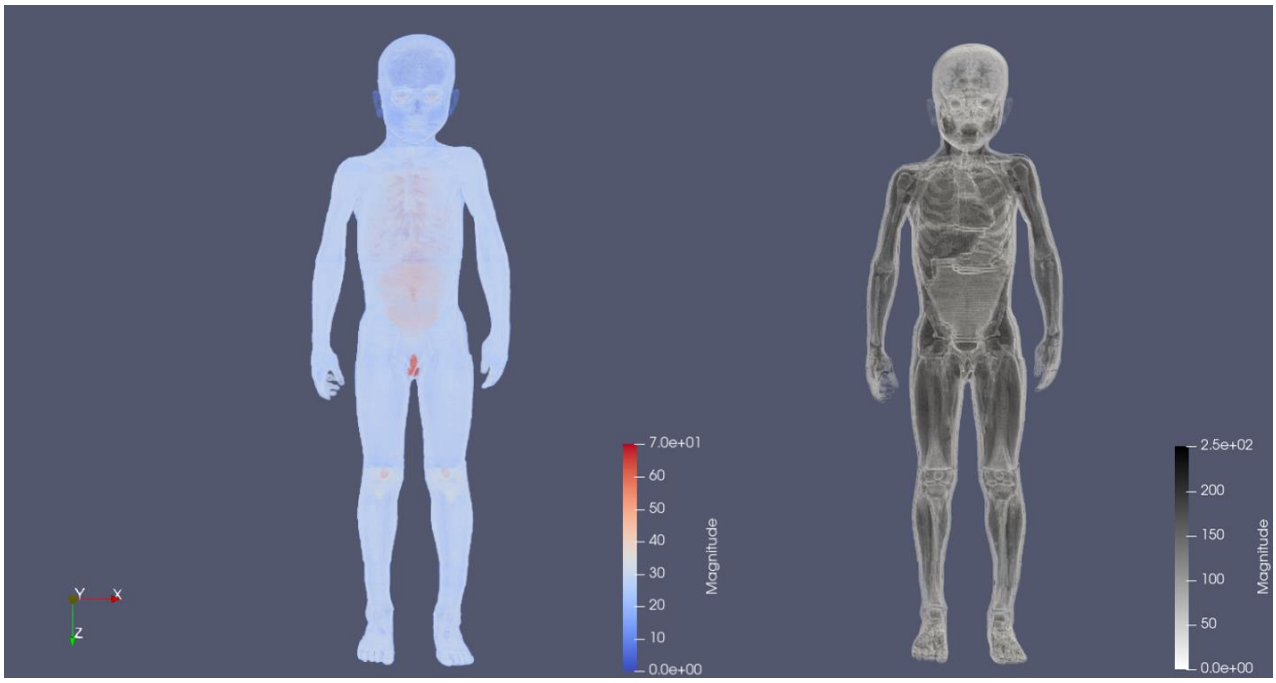

Figure 18: *3D representation of Thelonious body: in the left in basic visualization (standard pre-set in scale range between [0 – 70]) and in the right in x-ray visualization (x-ray pre-set with "shade" option in scale range between [0 – 250])*

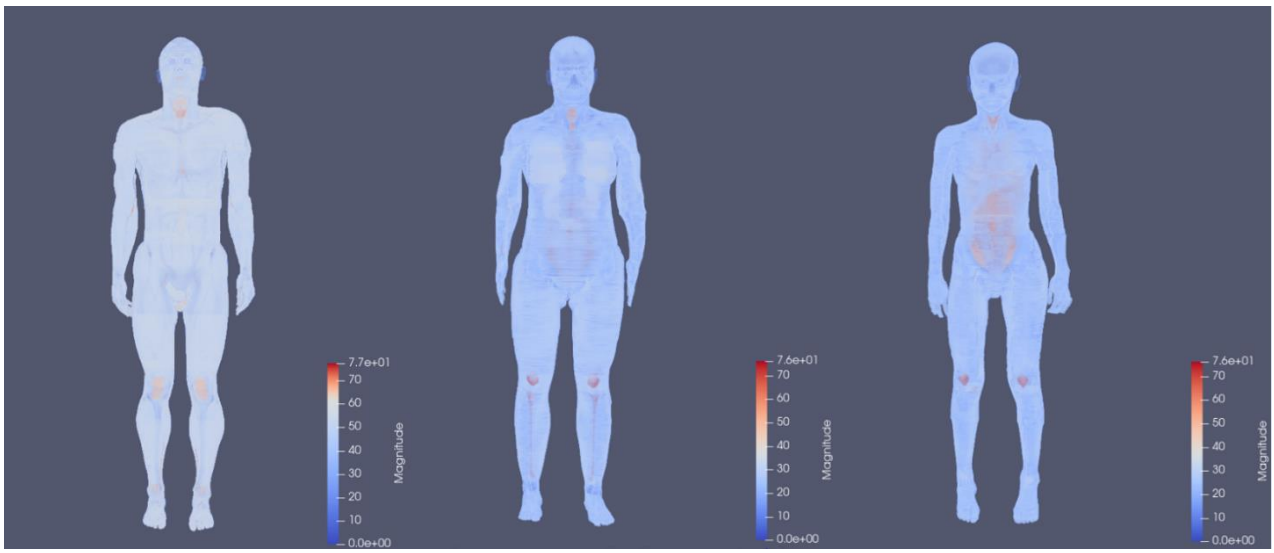

Figure 19: *3D representation of respectively Duke, Ella and Billie in basic visualization (standard pre-set in scale range between [0 – 76])*

For a small simulation on single body parts, the segmentation of the model is needed. So, starting from the entire map of the body on ParaView the desired dimensions have been identified for x, y, and z. The corresponding cell number has been used in the MATLAB environment to replace the number of the for-loop counter variables and create a new VTK file (Figure 20).

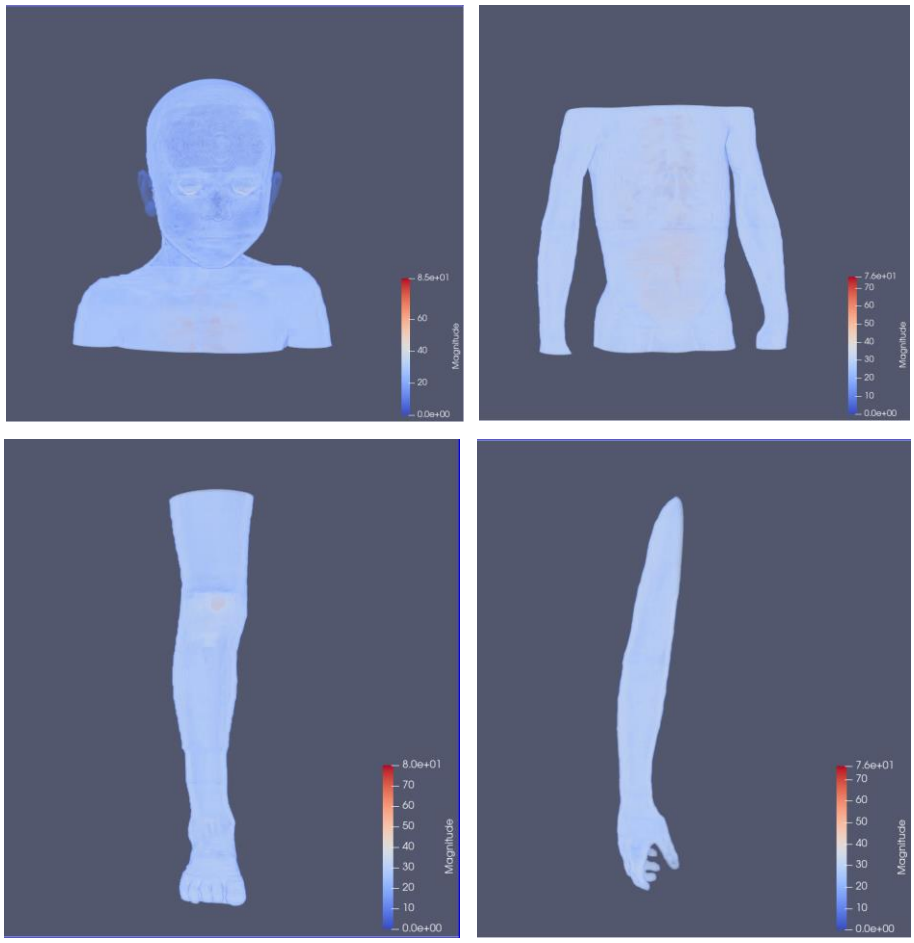

Figure 20: *Segmentation of Thelonious body model*

2.2 Antenna model design

Once extracted the human model, the second part of the procedure for the electromagnetic characterization of an HRM device consists in the modelling of the real antenna.

2.2.1 Choice of the device

Since on the market there is a huge presence of heart rate sensor strap, in order to simulate in a real possible manner, the interaction with the human body, the choice of the model is based on the possibility to find in literature the internal components, in particular the antenna characteristic geometry. The HRM device reference model chosen to perform the simulation is the *Garmin Soft Strap Premium Heart Rate Monitor* (Figure) [52] found in the Federal Communication Commission (FCC) ID Database, which is an information database used for storing all the devices conform to US FCC standards using a unique identifier (ID).

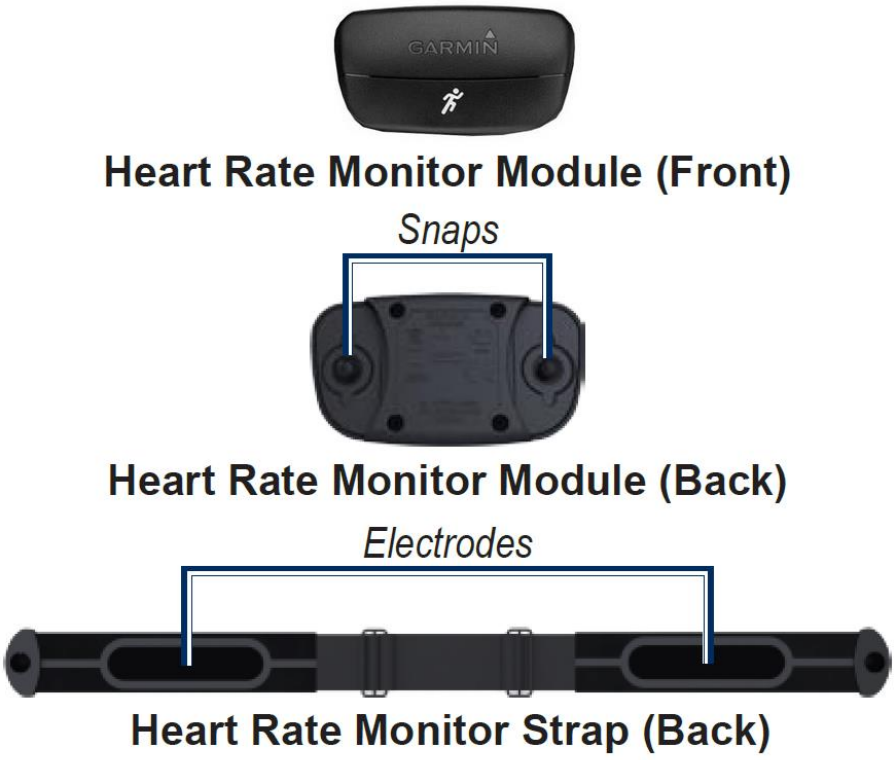

Figure 21: *Garmin Soft Strap Premium Heart Rate Monitor components* [52].

The HRM specifications are reported in the following table (Table 3) [52]:

Table 3: *Technical specifications of the Garmin Soft Strap Premium Heart Rate Monitor*

FCC ID	IPH-F3ARNA
Module	2.4" W x 1.3" H x 0.4" D (62 mm x 34 mm x 11 mm)
Strap Length	Adjustable from 21" to 29.5" (533 cm to 750 cm)
Weight	1.6 oz (45 g)
Water Resistance	3 ATM (30 m)
Battery	User-replaceable size CR2032 (3 volts)
Battery Life	Up to 4.5 years (based on average use of 1 hour per day)
Operating Temperature	23°F–122°F (-5°C–50°C)
Radio Frequency/Protocol	2.4 GHz ANT wireless communications protocol
Range	3 m
System Compatibility	System Compatibility: ANT+

The Garmin chest monitor uses ECG sensor snaps (Figure 21) which are characterized by a dual use, since they are also important to remove the monitor to change the battery or to clean the strap. For this reason, the strap must be worn next to the skin so that the electrodes can make contact. Once the heart rate monitor detects a heart rate, it sends all the information to a compatible device via ANT+ wireless protocol.

2.2.2 Parametrization and geometry definition

From the database, by searching the FCC ID of the Garmin device, it has been possible to find the details on the wireless operating frequency (including strength), external and internal photos (Figure 22 and 23), user manuals and test performance of the device. Starting from the internal photos, the device geometry model has been defined along with the parametrization of the printed circuit board and inverted-F antenna visible in Figure 23.

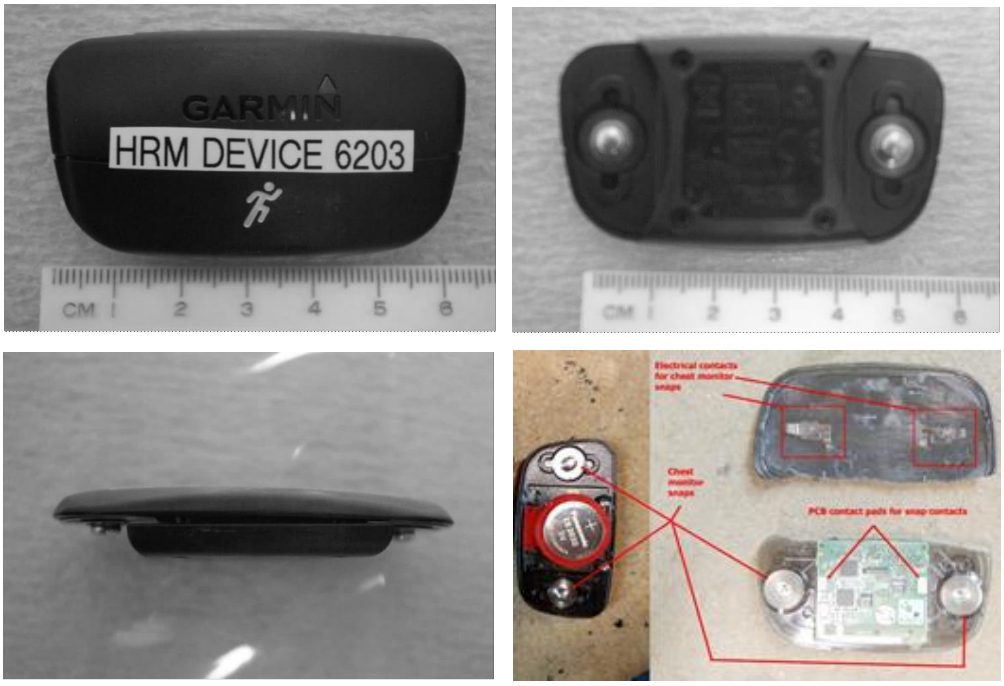

Figure 22: *Heart Rate Monitor external and internal photos and dimensions*

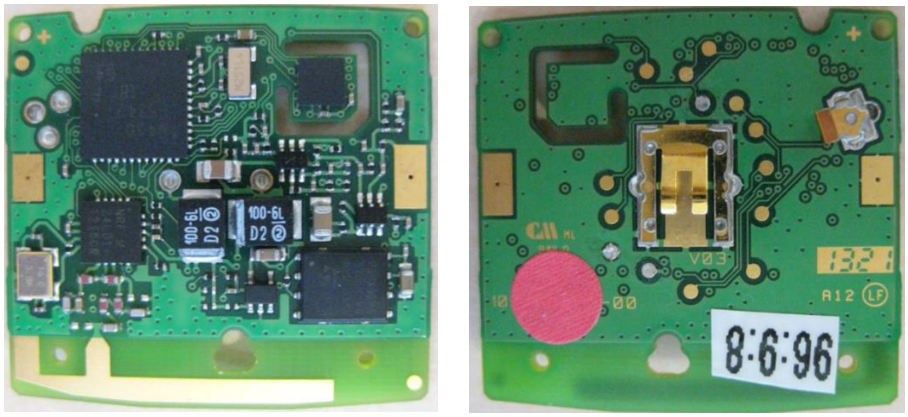

Figure 23: *Heart Rate Monitor PCB: front (left) and back (right) part*

The parametric representation is a creation of a scheme, in this case of the PCB (Figure 20), in which all the lengths are specified as parameters in order to design the model of the antenna in the FDTD domain. At each parameter a value has been found which reflected as much as possible the real dimension of the internal PC board of the device. The dimensions in cells for the parameters have been obtained through proportions from Figure 23:

- Ldx = 40, Ldy = 1, Ldz = 40
- Wm1 = 2, Wm2 = 2, Wm3 = 2
- l1 = 5, l2 = 22, l3 = 4
- ax = 1, az = 1
- d1 = l3 + Wm3 + az = 7
- d2 = Ldx - (l2 + Wm2 + Wm1 + l1 + ax) = 8

Moreover, all the points in the front and back part and the orientation of the PCB have been defined, useful for the positioning of the PCB in the FDTD space (where “u” stay for up, “d” for down and “a” for antenna) (Figure 24).

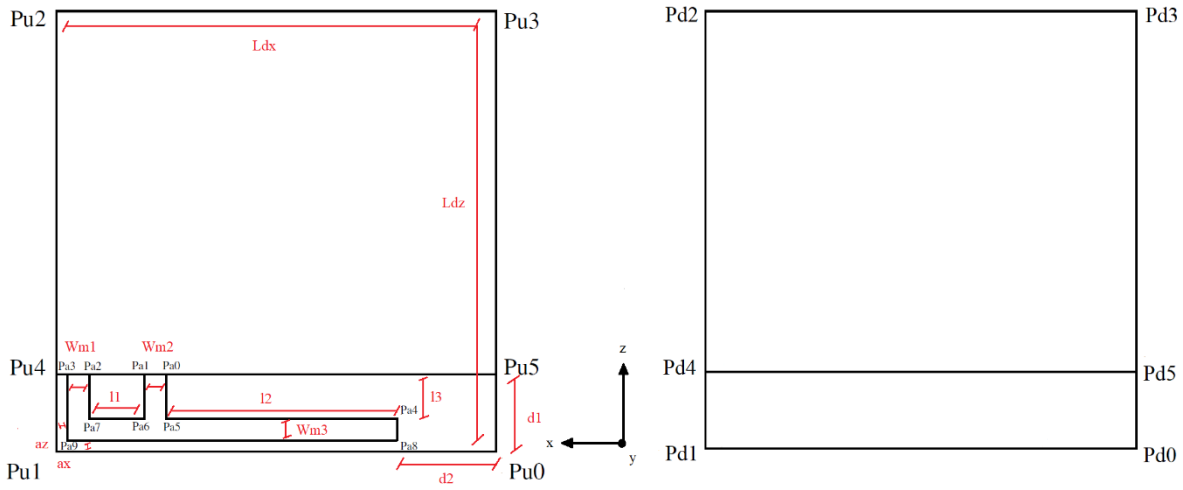

Figure 24: *Scheme of PCB with geometry parameters: front (left) and back (right) part*

The real antenna is fed by a microstrip line, which is the transmission line that connect to the coaxial cable. Therefore, in order to obtain a correct simulation result, the orientation and the dimensions of the monopole antenna have to be specified. Below are reported the dimension in cells, the orientation, and the geometric scheme of the monopole (Figure 25).

- haz = 1
- oriented in the downward direction of z axis

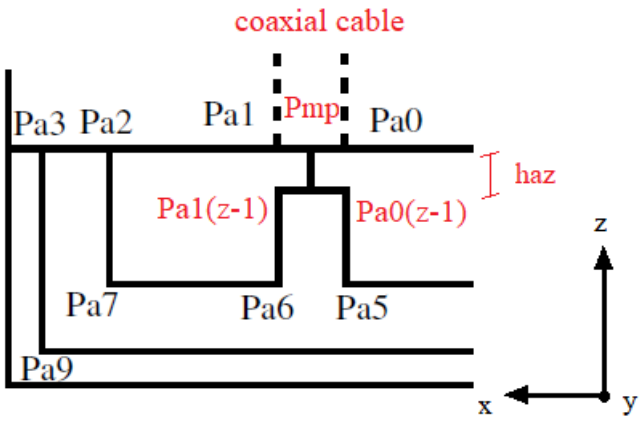

Figure 25: *Scheme of the antenna connected to the transmission line in the coaxial cable*

For a simpler and easier implementation, the model of the device does not include the external case, but only the PC board with the antenna, which represent the most relevant part for the electromagnetic characterization of the field. All the defined points with the cells number dimensions represent the model of the antenna that have to be defined in the FDTD space to perform the simulation.

2.3 FDTD Simulation

The simulation analysis of the presented antenna is carried out through FDTD technique, implemented with C programming language. Considering the weaknesses of the FDTD approach one of the limitations is the spatial discretization, which force to divide the computational domain into grids causing an approximation error in the model solution. To overcome this limitation the boundary conditions are used allowing to extend the obtained solution to an infinite domain.

For this simulation, the second order Mur's ABCs are implemented since they introduce a correction for the oblique incident wave problem typical of the first order Mur's solutions, and due to the simplicity in the implementation with respect to the Perfectly Match Layer (PML). The FDTD simulation include two steps: the first is the model validation of the antenna and the second regards the interaction of the device with the body model.

2.3.1 Antenna model simulations

To define the 3D shape of the antenna, all the points positions and dimensions are defined and translated from the PCB coordinate to the coordinate of the FDTD grid, thus 50 cells (25 at the beginning and 25 at the end) have to be added to the x, y, and z values, considering the FDTD edge

representation. Moreover, a one more cell is considered due to the last counted field which is out the edge of the domain. For instance, the monopole probe position is defined as follows:

$$\mathrm{Pmp}(x_p, y_p, z_p) \text{ where}$$

$$\begin{cases} x_p = \mathrm{EdgeFDTD}_x + (\mathrm{Ldx} - (\mathrm{ax} + \mathrm{Wm1} + \mathrm{l1} + \frac{\mathrm{Wm2}}{2})) \\ y_p = \mathrm{EdgeFDTD}_y + \mathrm{d1} \\ z_p = \mathrm{EdgeFDTD}_z + \mathrm{Ldy} \end{cases}$$

Once inserted the points, the three-dimensional representation of PCB model in the FDTD space has been specified. The ground plane configuration of the PCB has been described through six rectangle planes, which vertices are the points of the geometric scheme of the model (Figure 24). For the inverted-F antenna instead the figure has been simplified to a two-dimensional image (using three rectangle forms) whereas the coaxial cable takes the form of a cubic structure in which the monopole is connected to the transmission line. (Figure 26)

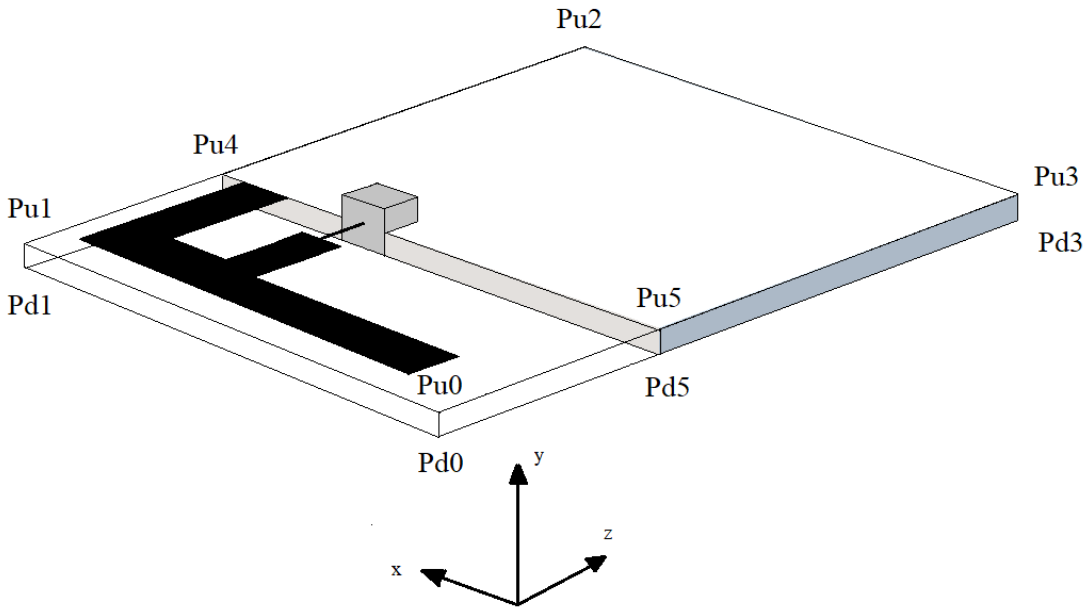

Figure 26: *PCB model in the FDTD 3D space*

The subsequent step is the definition of the substrate material which has been found in the literature and defined in terms of dielectric constant ε_r and σ. The conductivity has been obtained from the loss tangent value ($\tan\delta$) which quantified the inherent dissipation of electromagnetic energy. The definition of the $\tan\delta$:

$$\tan\delta = \frac{\varepsilon''}{\varepsilon'} \quad (4.1)$$

$$where \quad \frac{\varepsilon''}{\varepsilon'} = \frac{\sigma}{\omega\varepsilon_0\varepsilon_r} \quad (1.2)$$

Joining the two equations, the conductivity (S/m) is defined as:

$$\sigma = \tan\delta\omega\varepsilon_0\varepsilon_r \quad (1.3)$$

Two different dielectric materials have been considered which guarantee good performance at 2.45 GHz (the device radio frequency band):

- FR408HR with ε_r = 3.67, tanδ = 0.0093 and σ = 0.0044 obtain from Equation 3.1[53].
- Teflon PTFE with ε_r = 2.2, with the same conductivity σ [54].

The stability factor of the simulation allows to define the correct dielectric material for the PCB, which turned out to be Teflon. Then, another simulation has been implemented to verify if the right angle of the microstrip bend in the model geometry has to be removed as in the original antenna image (Figure 23). Since all the geometry is defined in cells on a discretized domain, only straight line can be used to segment the geometry. The new model scheme is reported in the following figure. (Figure 27)

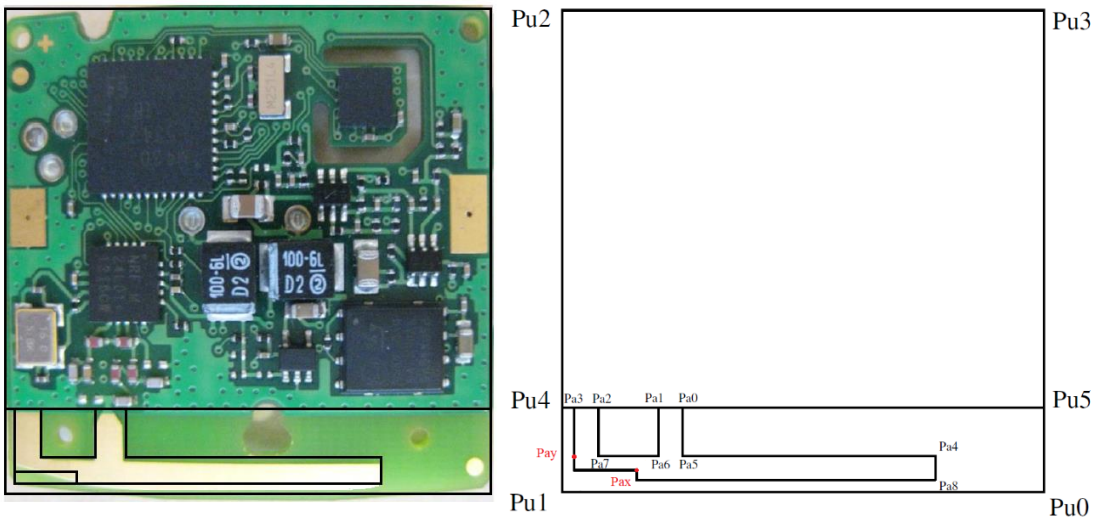

Figure 27: *PCB scheme with new geometry*

In the FDTD domain the microstrip for the new geometry is again defined as a two-dimensional image but the rectangles used for the representation are no longer three but rather four. (Figure 28)

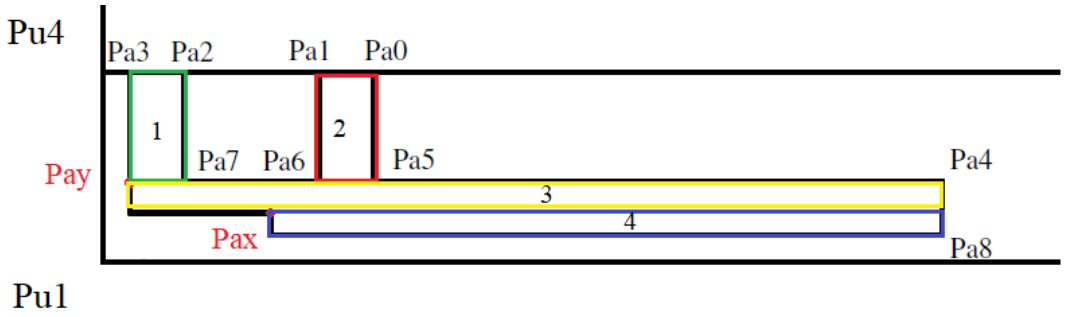

Figure 28: *Microstrip antenna rectangles definition*

Once defined the geometry and the dielectric material, the *impedance matching* has been evaluated, which means verifying if the condition of maximum power transfer is reached. The presence of a mismatch between the transmission line and the final load produces a wave reflected towards the transmitter with possible damage to the electronic circuitry, as well as a decrease in the power of the transmitted signal. Through the evaluation of the reflected signal is possible to understand if the device or lines are matched and if the model has been defined correctly in the three-dimensional space.

2.3.2 Embedded antenna simulations

Using the virtual human model and the model of the antenna, is possible to study the interaction of the device embedded on the body. To do that, the position in spatial coordinates has been defined using the "Slice view" representation of ParaView. Two different simulations have been implemented: one with only the torso part of Thelonious body and the other with the whole-body model. The cartesian coordinates of point of application of the monopole in the FDTD space domain are:

Table 4: *Point of application of the monopole antenna*

For Thelonious torso:	From the 3D map: x = 0.22 y = 0.165 z = 0.15 In the FDTD domain (cells): Pmp.i = EdgeFDTD + (Ldx - (ax + Wm1 + l1 + Wm2 / 2) - 20 + 220) Pmp.j = EdgeFDTD + (Ldy - 1 + 165) Pmp.k = EdgeFDTD + (d1 - 20 + 150)

For Thelonious body:	From the 3D map: x = 0.22 y = 0.165 z = 0.39 In the FDTD domain (cells): Pmp.i = EdgeFDTD + (Ldx - (ax + Wm1 + l1 + Wm2 / 2) - 20 + 220) Pmp.j = EdgeFDTD + (Ldy - 1 + 165) Pmp.k = EdgeFDTD + (d1 - 20 + 400)

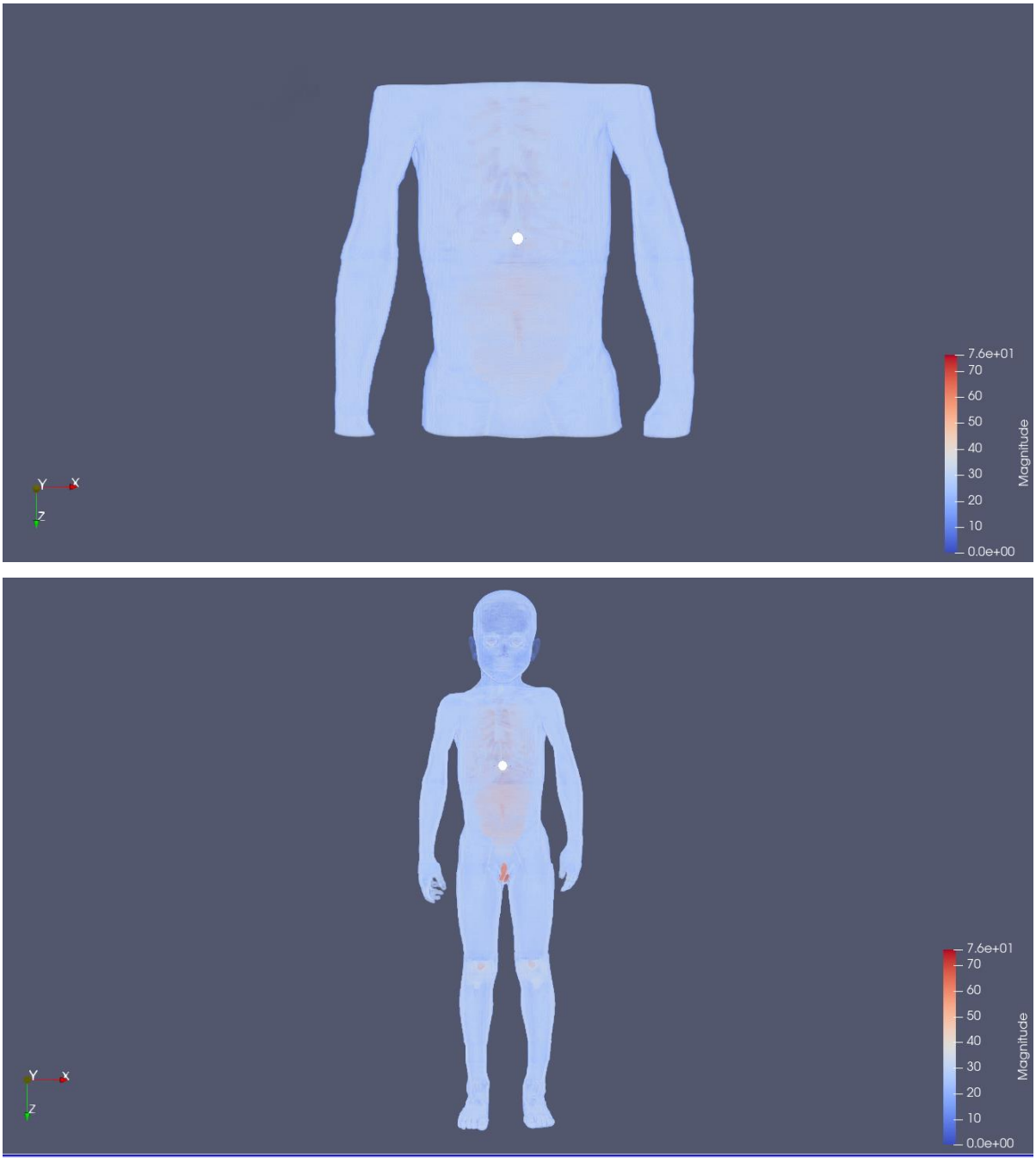

Figure 29: *Point of application of the monopole (white circle) on Thelonious torso and whole-body*

The FDTD simulation allows to calculate the values of the electric and magnetic field generated by the antenna and to evaluate the SAR in terms of dissipated power for all the tissues present in the virtual model. Since the SAR, the dielectric constant ε_r and conductivity σ values for all the tissues are studied in a specific frequency of interest, the FDTD algorithm simulation has been implemented with a ramped sinusoidal excitation at 2.45 GHz. (Figure 30) This modulated input signal stabilized over 10 periods allowing to avoid the introduction of spurious frequency around the one of interest.

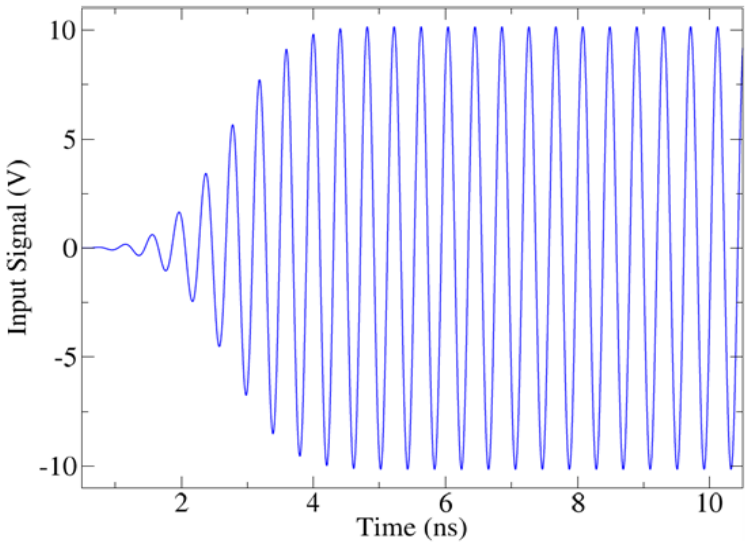

Figure 30: *Modulated sinusoidal excitation applied in input*

The algorithm computes the field inside a single cell in all the directions, then evaluate the maximum and print for all the cells the field values as output. To determine the dissipated power for the specific tissue, the SAR has been used, which can be calculated from the electric field as:

$$SAR = \frac{\sigma|E|^2}{2\rho} \ (W/kg) \qquad (1.4)$$

Since the values of the electric fields used in the simulation are not effective values, but a maximum value (or peak value) of a sinusoidal quantity, the half term is introduced in the SAR equation.
The power absorbed in a single cell of tissue is defined as power density and equal to:

$$Cell\_pot = \frac{\sigma|E|^2}{2} * V \qquad (1.5)$$

in which the volume V parameter correspond to 1 mm^3 since the cell's length, width and height are respectively 1x1x1 mm. The percentage of absorbed power for all the tissues has been obtained dividing the tissue dissipated power (which is an average of the power dissipated in all the cells of

the tissue) for the power dissipated in all the map, which is equal to the sum of each cell's power contribution:

$$Pot\_tot = \sum_{1}^{n_{cell}} \frac{\sigma |E|^2}{2} * grid\_volume \quad (1.6)$$

The percentages of the absorbed power are printed in output for all the tissues names which can be controlled to verify the correct execution of the simulation. Additionally, also the tissue occurrences are printed in output, which represent the number of cells of a particular tissue of the body model; these values are checked through a qualitative evaluation since the exact number of the tissue cells is unknown.

Eventually, the whole simulation process has been repeated using other body models and considering different points of application of the device, in order to analyse the variations in power dissipation throughout different body masses and the sensitivity to distances of the generated field.

3. Results

In this chapter are reported all the data, graphs and images relating to the simulations, the electromagnetic characterization of the antenna and its interaction with the body.

3.1 Antenna

The return loss is analysed in order to verify the matching of the device or lines at the transmitting and receiving frequencies. This dimensionless parameter is reported below for the three simulations performed on the antenna, in order to understand the correct geometry and the right dielectric material for the model design.

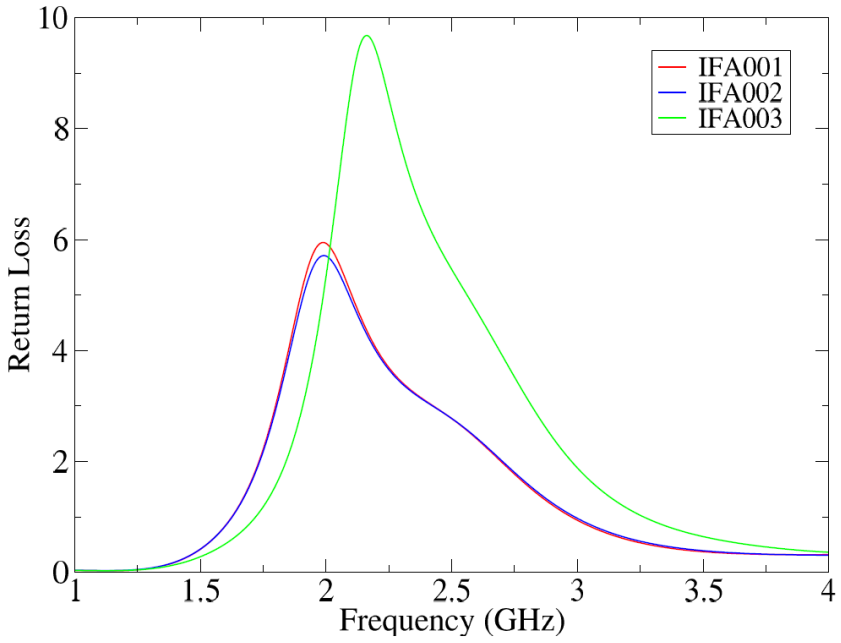

Figure 31: *Return loss for the whole geometry (red) and geometry with the clipped bend (blue) using FR408HR (ε_r = 3.67). Clipped geometry with Teflon (ε_r = 2.2) (green)*

Also, the reflected signal in a band of frequencies between [1 – 4] GHz has been evaluated in order to verify the condition of maximum power transfer. In the next figure, the reflected signals over time at three frequencies are reported: one is the working frequency (f=2.45 GHz) at the centre of the ISM band and the other two (f=1.5 GHz and f=3 GHz) are frequencies not included in the ISM band, where the antenna is mismatched.

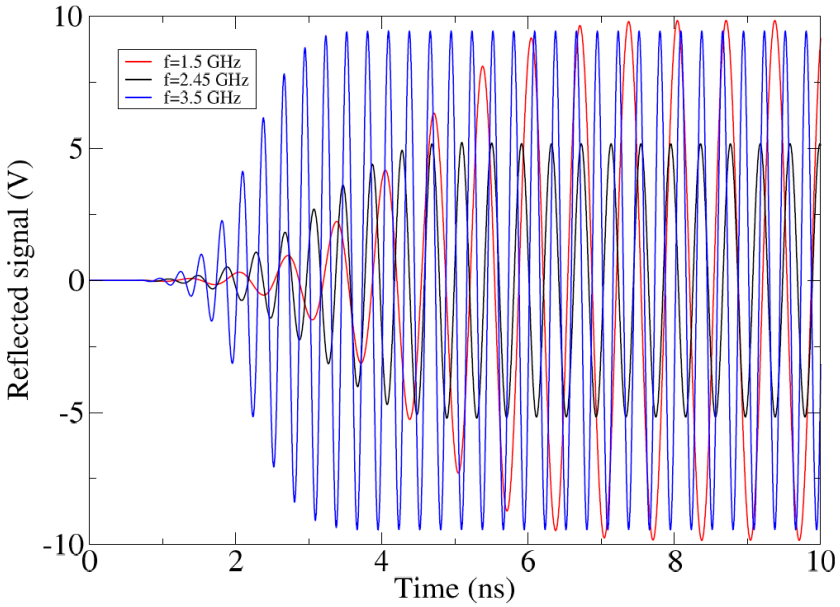

Figure 32: *Reflected signal at f=2.45 GHz (black), f=1.5 GHz (red) and f=3 GHz (blue)*

The matching of the impedance, using the 3D representation of the generated fields, can be also visualized for the three studied frequencies. The following figures are obtained with ParaView software with scale range values between [0 - 10000]. For the working frequency (f= 2.45 GHz) which represents the center of the ISM band other views are also reported.

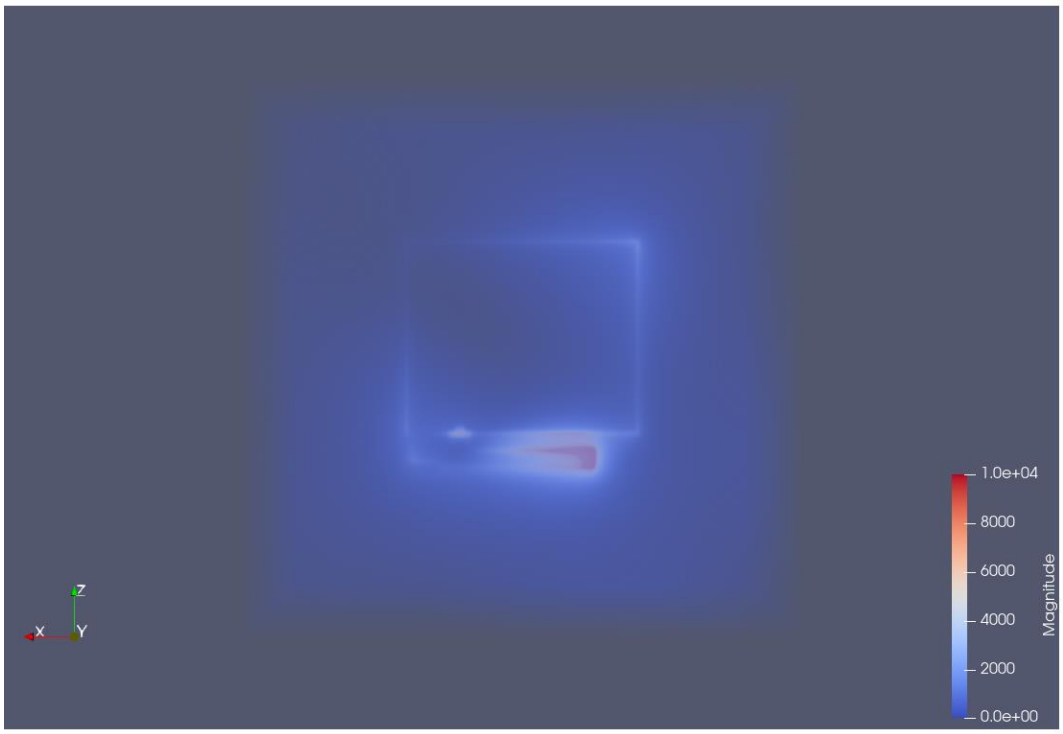

Figure 33: *Top view of the electric field magnitude at f=2.45 GHz.*

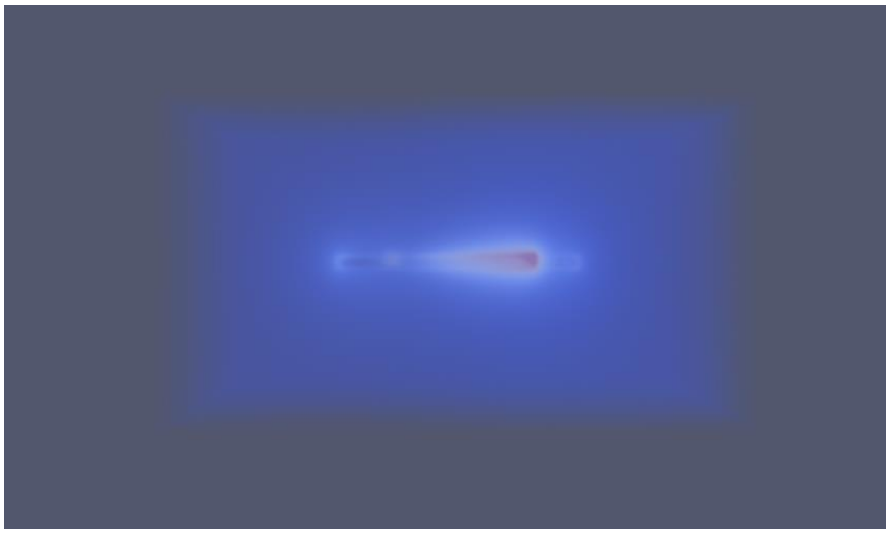

(a)

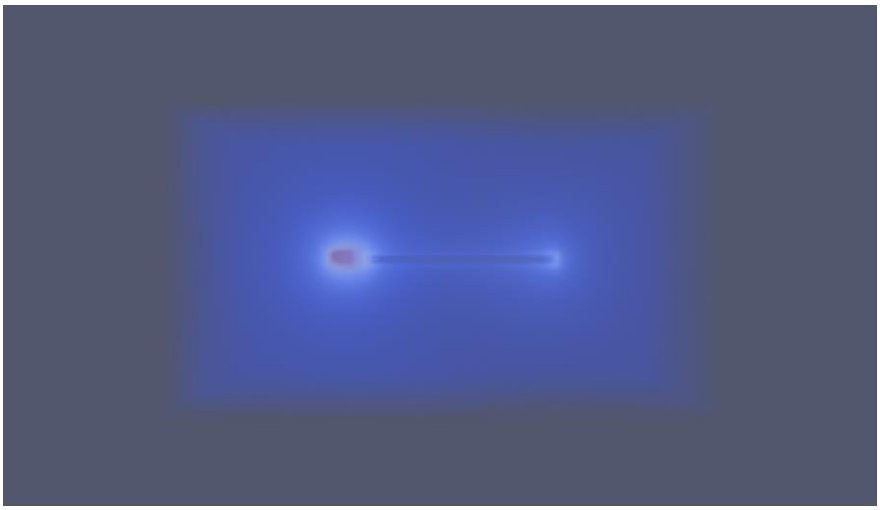

(b)

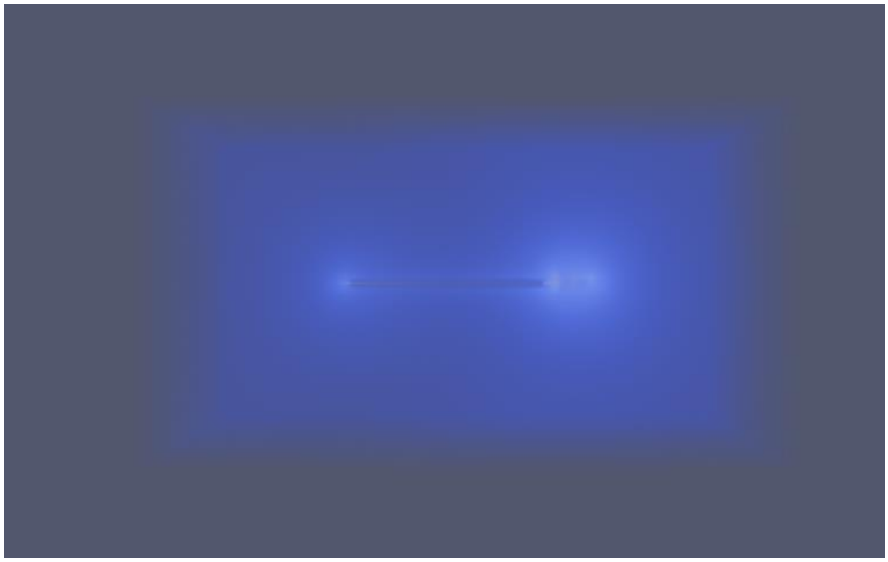

(c)

Figure 34: *Magnitude of the electric field at f= 2.45 GHz: bottom side view (a) right side view (b) and left side view (c)*

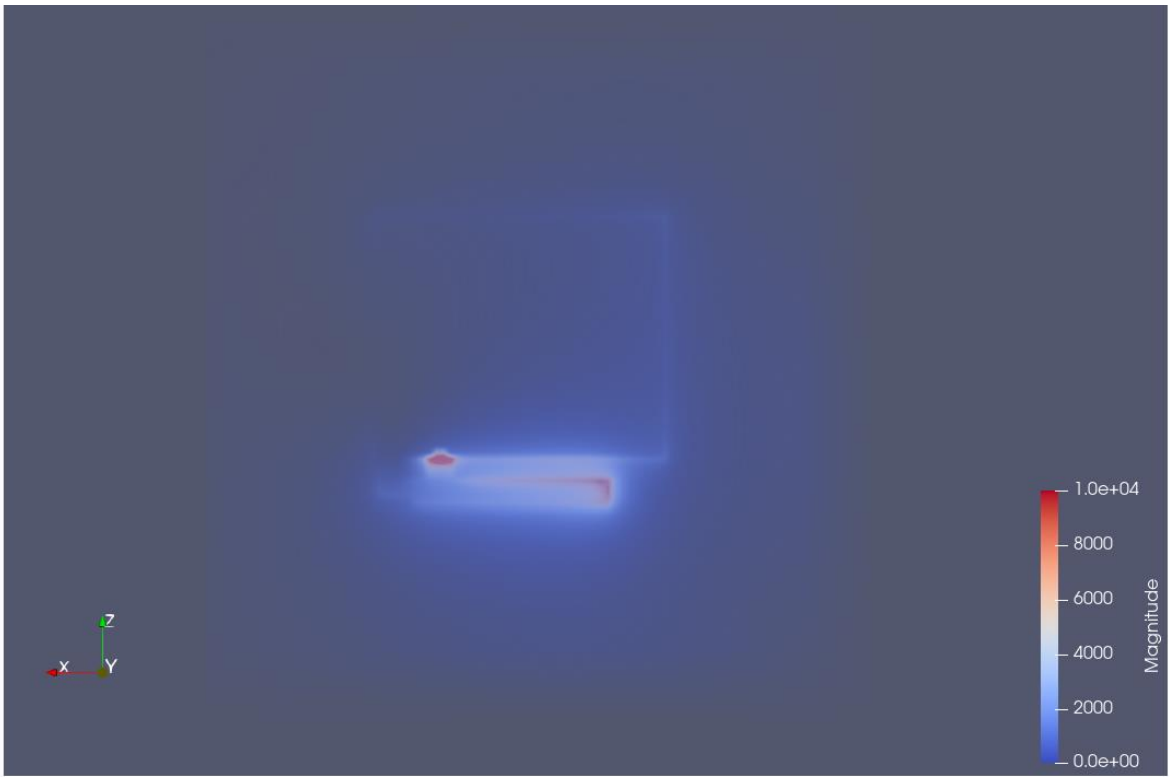

Figure 35: *Top view of the electric field magnitude at f=1.5 GHz*

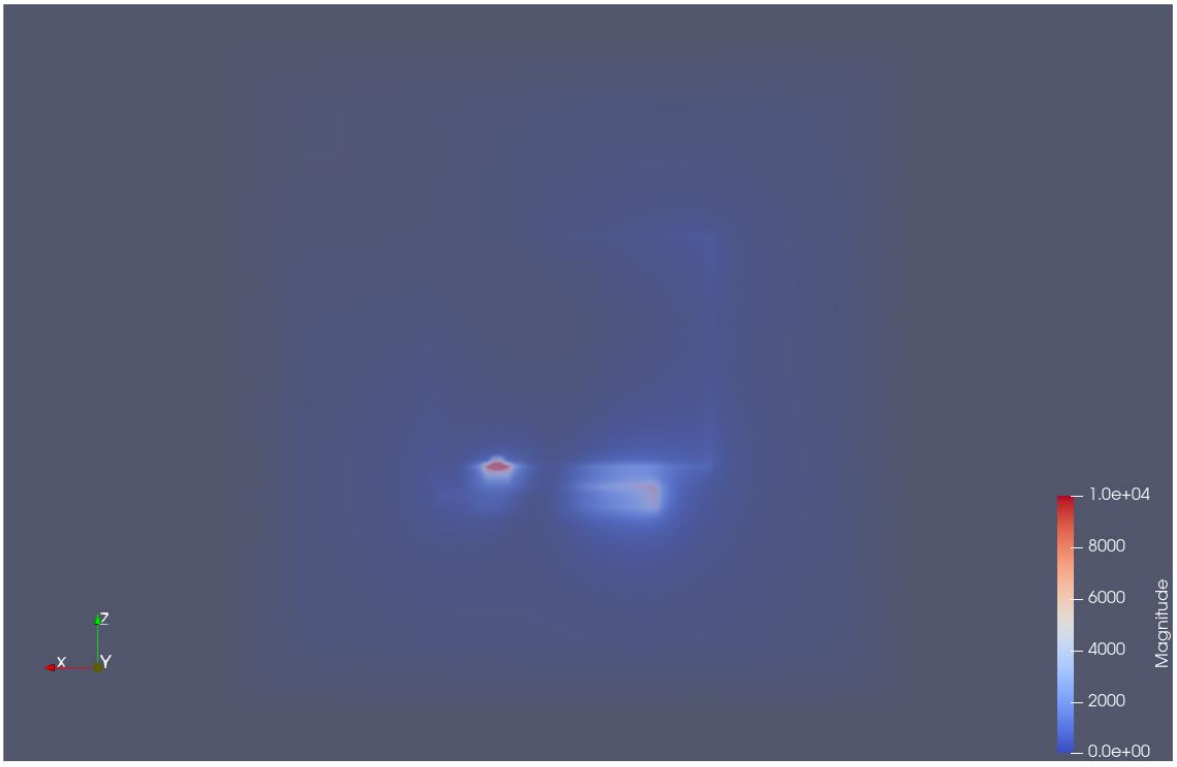

Figure 36: *Top view of the electric field magnitude at f=3 GHz*

3.2 Body-antenna interaction

In this section, the simulation results and the electromagnetic characterization of the interaction between the antenna and the body are reported.

The first two simulations are implemented using Thelonious body; in the first case only the torso model while in the second case using the whole model of the body, as already explain in the Methods section.

The maximum and the minimum values of the stability factor are also calculated for all the FDTD simulations, which, must be less than one in order to satisfy the numerical stability condition of Courant–Friedrichs–Lewy. These values are:

- Stability factor of the thorax model simulation Max – Min: 0.986586 - 0.121217
- Stability factor of the whole-body model simulation Max – Min: 0.986586 - 0.119459

The electromagnetic characterization of the embedded device is visualized on ParaView using the map model and outputs of the simulation which are the SAR and the magnitude of the field. The results for the first simulation in which is used the torso model is reported in the following figures:

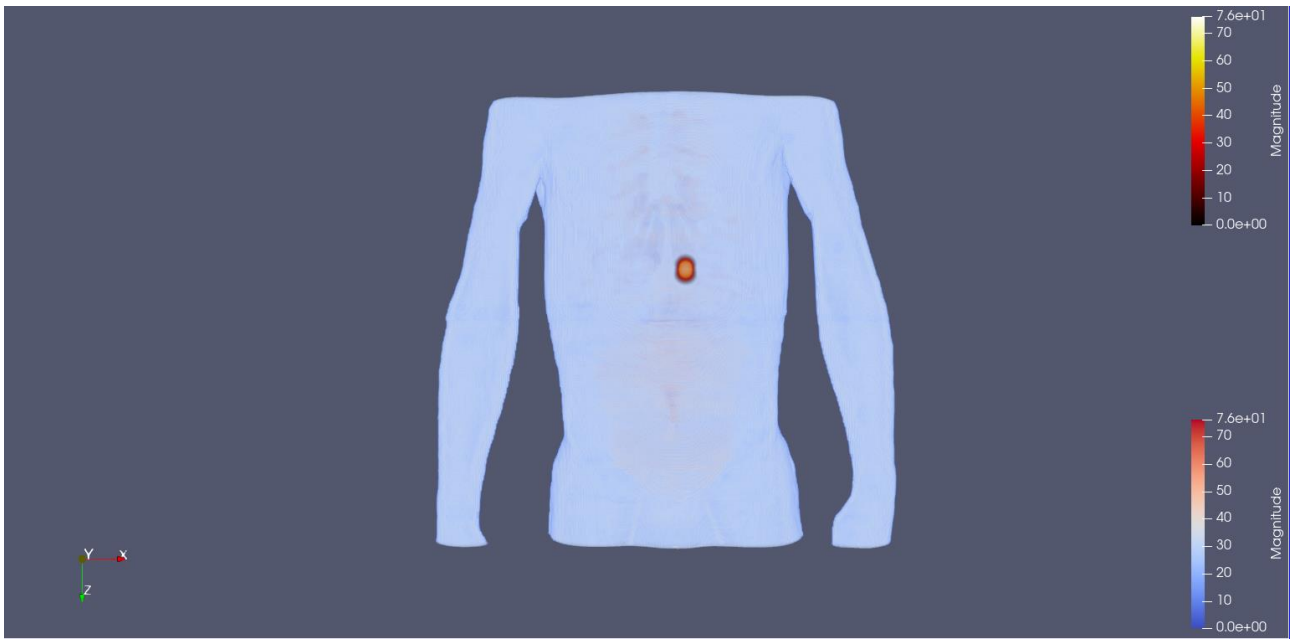

Figure 37: *Electric field magnitude generated by the embedded antenna. Body segment colour range between [0 – 76] in standard pre-set and field colour range between [0 – 76] in body-black radiation pre-set*

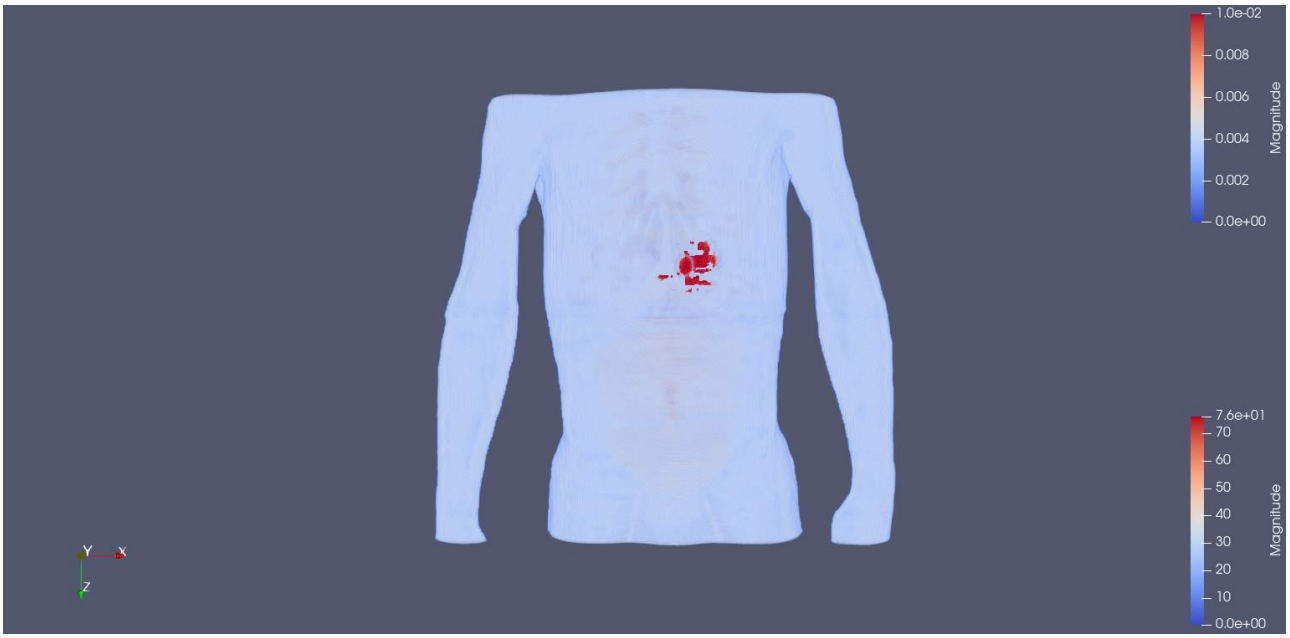

Figure 38: *Specific absorption rate (SAR) representation. Body segment colour range between [0 – 76] and SAR colour range between [0 - 0.01] in standard pre-set*

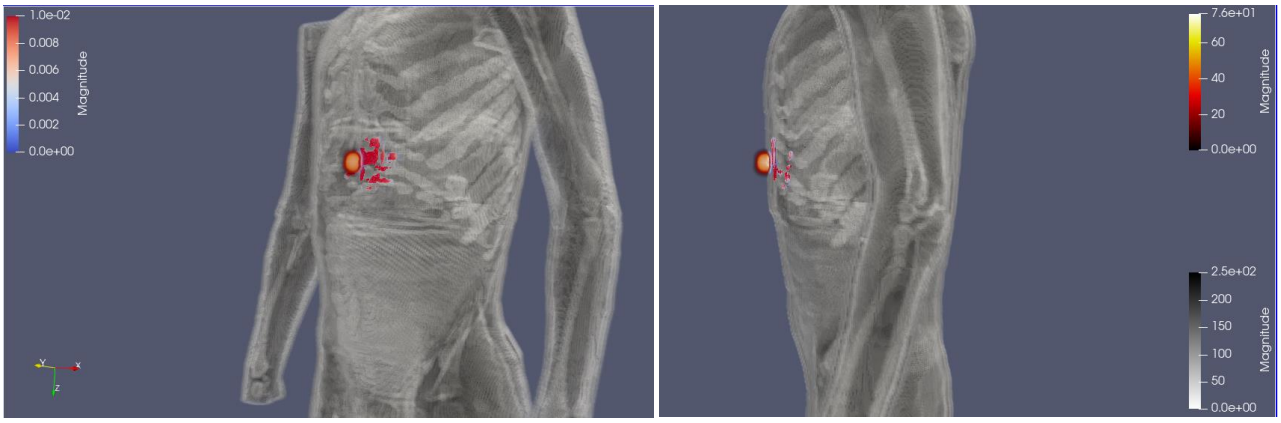

Figure 39: *Focus: SAR representation with colour range between [0 - 0.01], body colour range between [0 – 250] in x-ray pre-set using "shade" option and generated field magnitude colour range between [0 – 76] in body-black radiation pre-set*

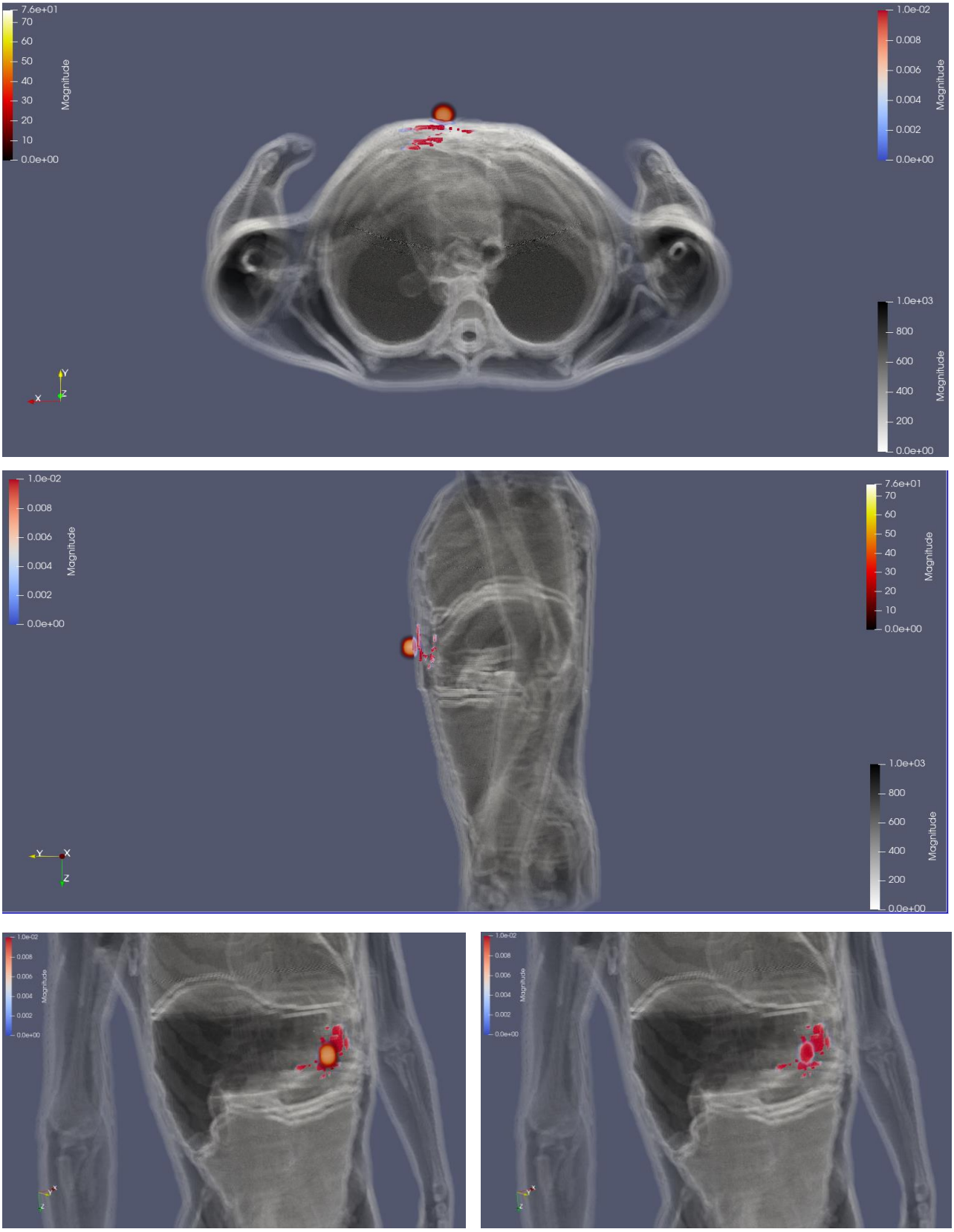

Figure 40: *Electric field magnitude and SAR representation in x-ray scale colour: body segment colour range between [0 – 1000] in x-ray pre-set and "shade" option. SAR colour range between [0 - 0.01] in standard pre-set and generated field colour range between [0 – 76] in body-black radiation pre-set. From top to bottom: transversal plane view, sagittal plane view and frontal plane view.*

In the same way the simulation has been implemented using the whole-body model of Thelonious. The results obtained from the simulation are reported below:

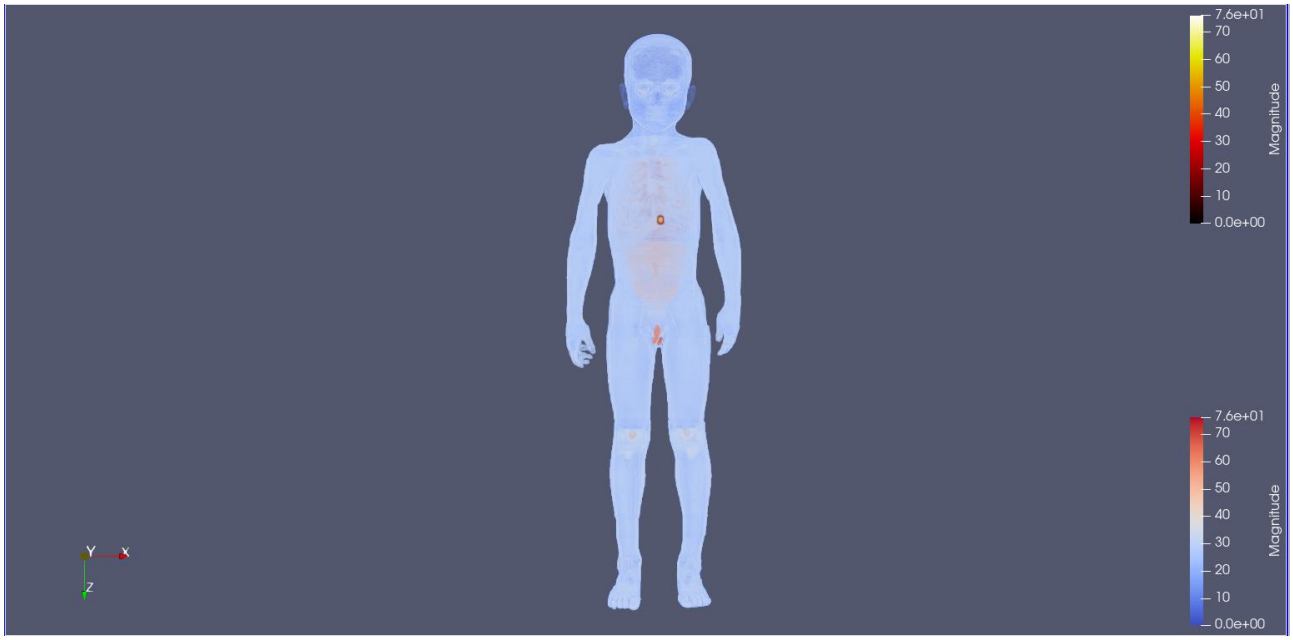

Figure 41: *Electric field magnitude generated by the embedded antenna. Body colour range between [0 – 76] in standard pre-set and generated field colour range between [0 – 76] in body-black radiation pre-set*

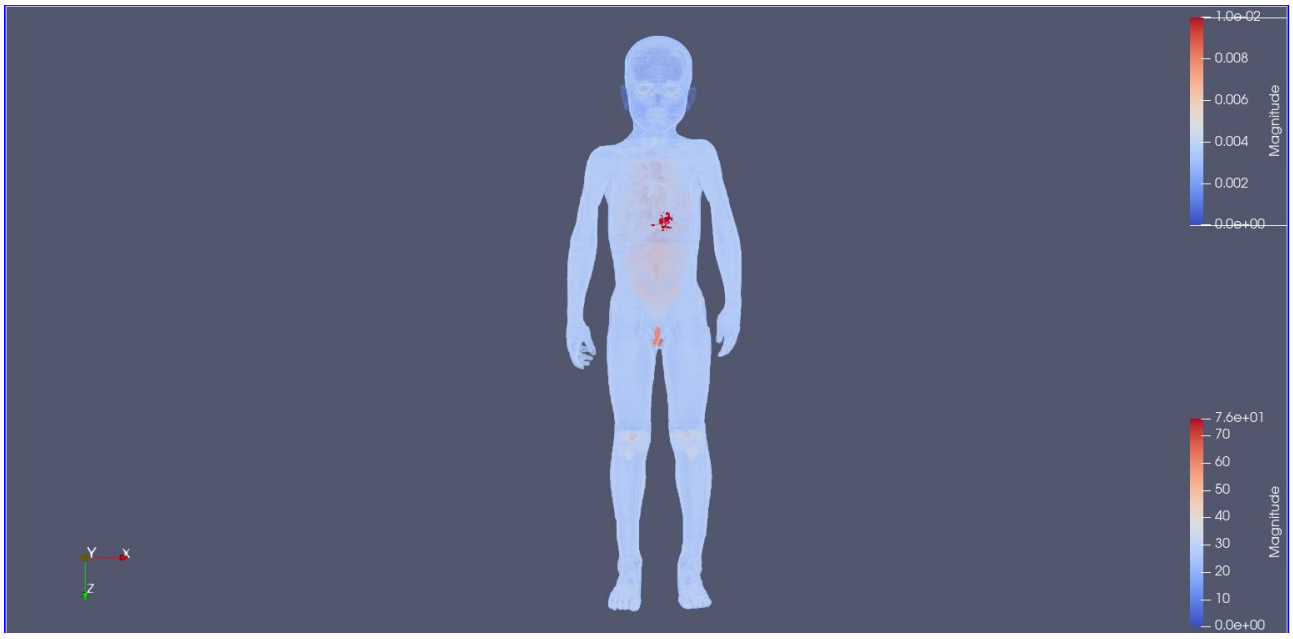

Figure 42: *Specific absorption rate (SAR) representation. Body colour range between [0 – 76] and SAR colour range between [0 - 0.01] in standard pre-set*

Figure 44: *Focus: electric field magnitude of the embedded antenna: body colour range between [0 – 76] in standard colour pre-set and generated field colour range between [0 – 76] in body-black radiation pre-set.*

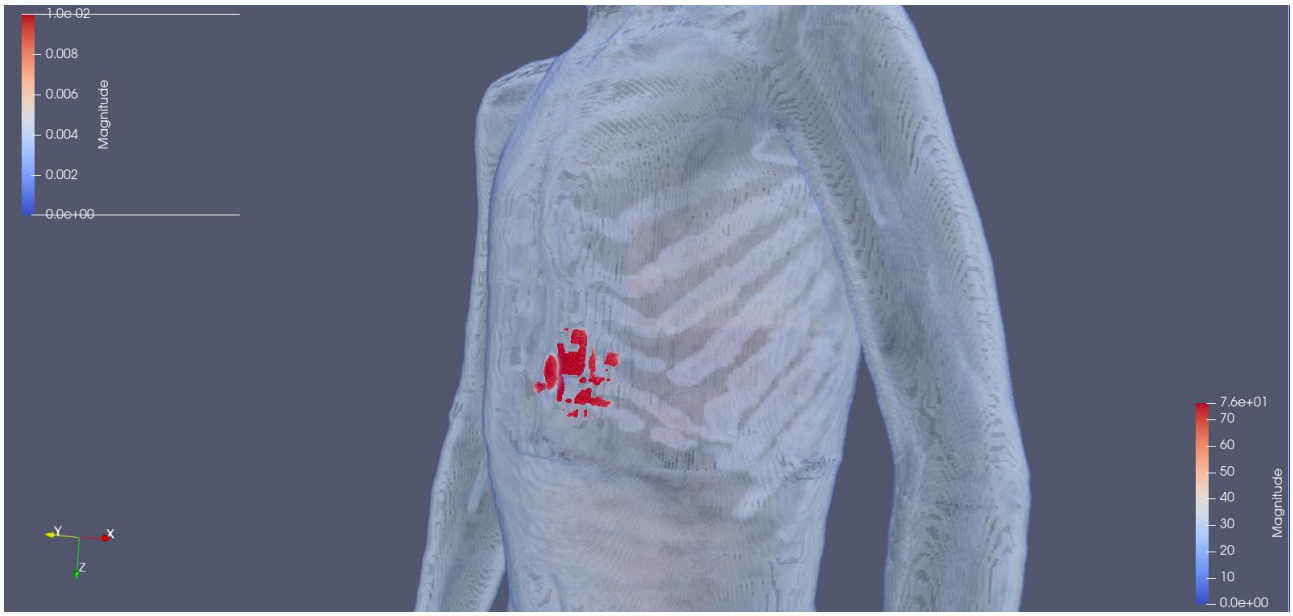

Figure 43: *Focus: SAR representation with colour range between [0 - 0.01] and body colour range between [0 – 76] in standard pre-set using "shade" option.*

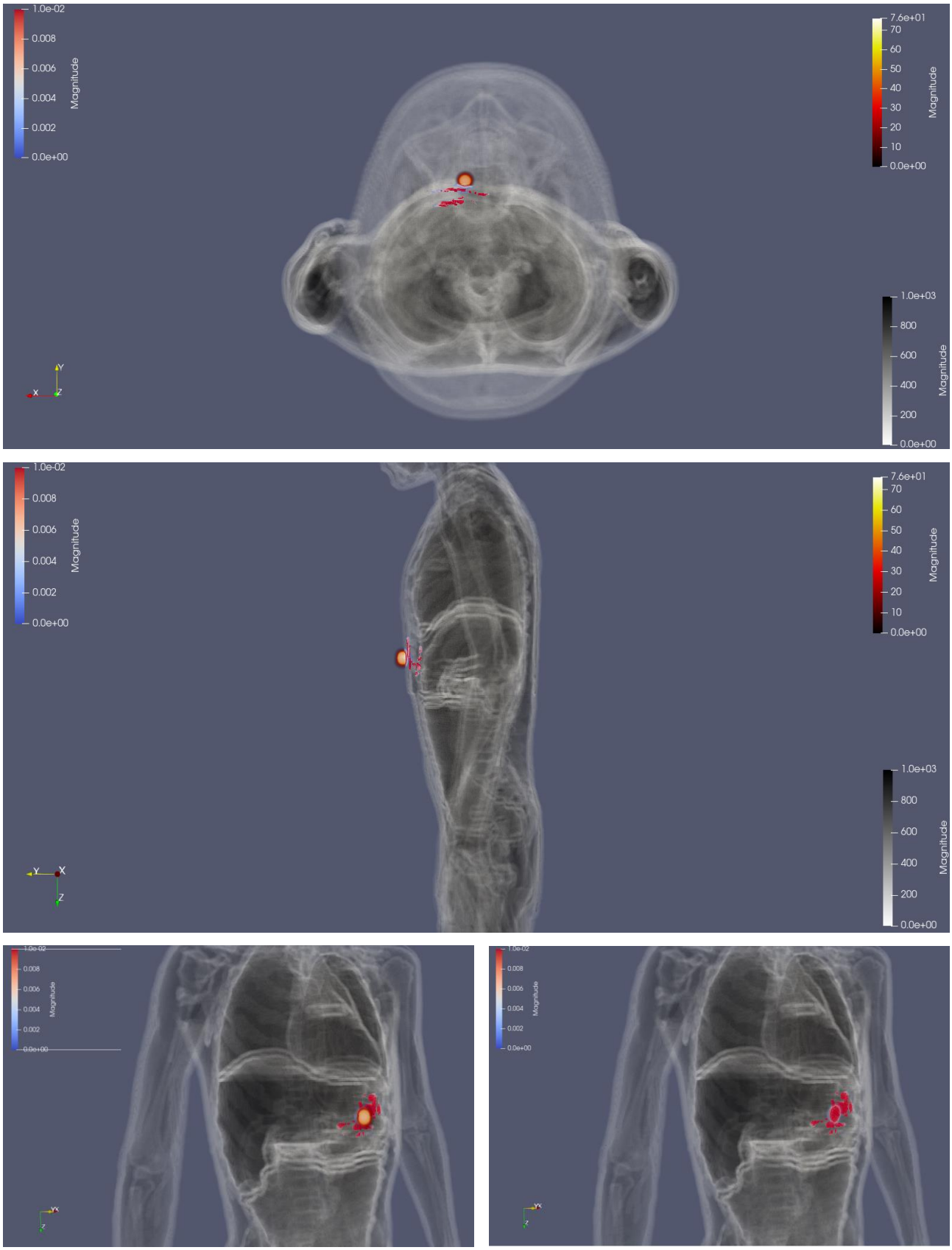

Figure 45: *Electric field magnitude and SAR representation in x-ray scale colour: body colour range between [0 – 1000] in x-ray colour pre-set and "shade" option. SAR colour range between [0 - 0.01] in standard pre-set and*

generated field colour range between [0 – 76] in body-black radiation pre-set. From top to bottom: transversal plane view, sagittal plane view and frontal plane view.

Using the "Slice" option on Paraview is possible to visualize the cut portion of the different planes. Below are reported the same slices of the transversal view in different mode visualization for the two simulations which are taken at:

- Torso segment model: xy plane at z = 0.135
- Body model: xy plane at z = 0.384

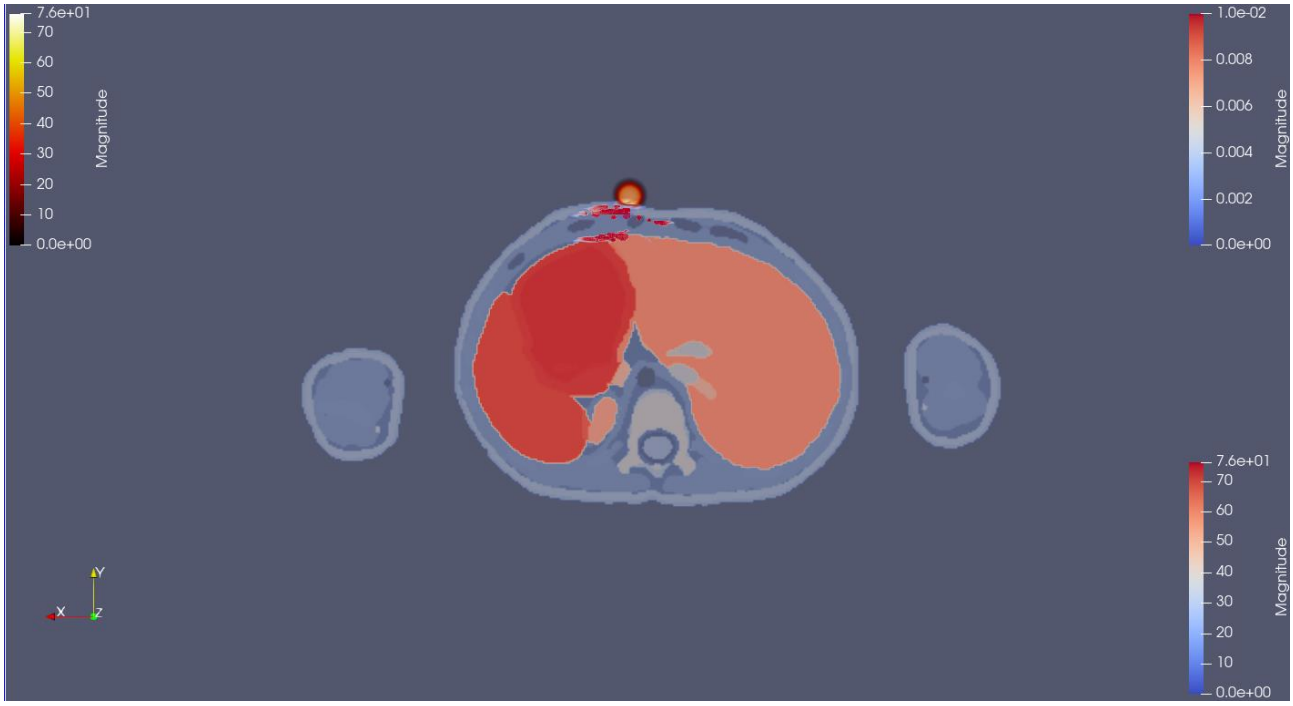

Figure 46: *Transversal slice of the thorax segment model simulation in standard visualization*

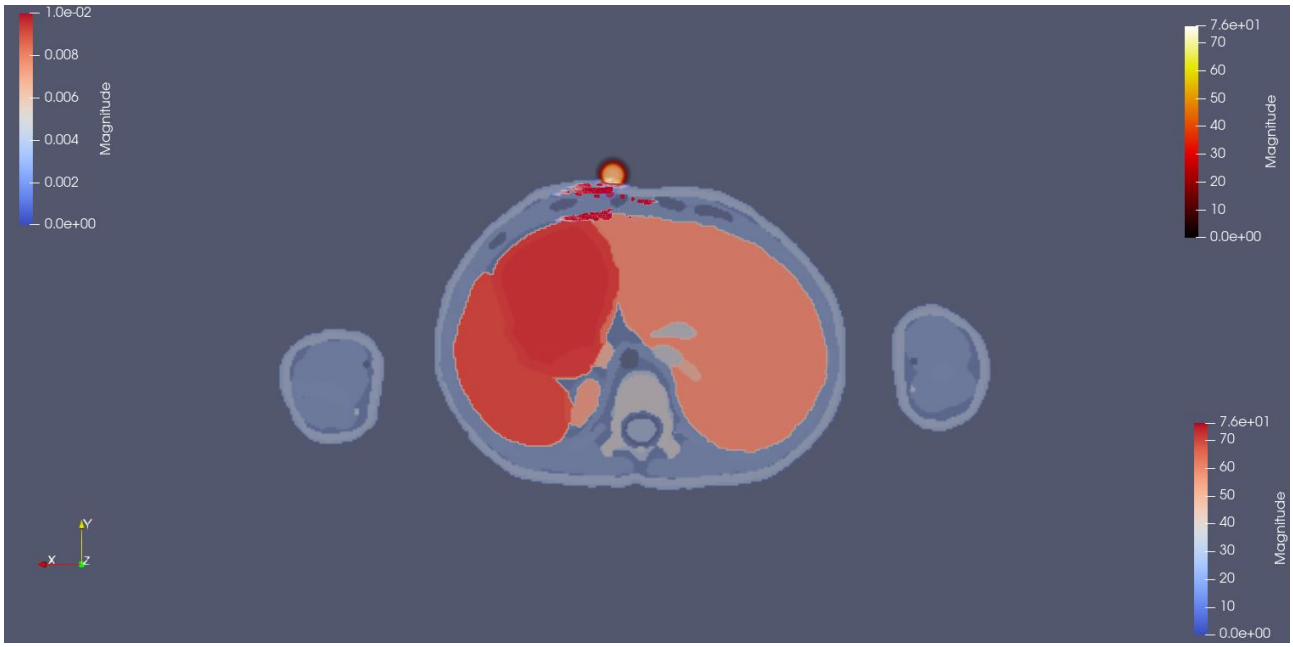

Figure 47: *Transversal slice of the whole-body model simulation in standard visualization*

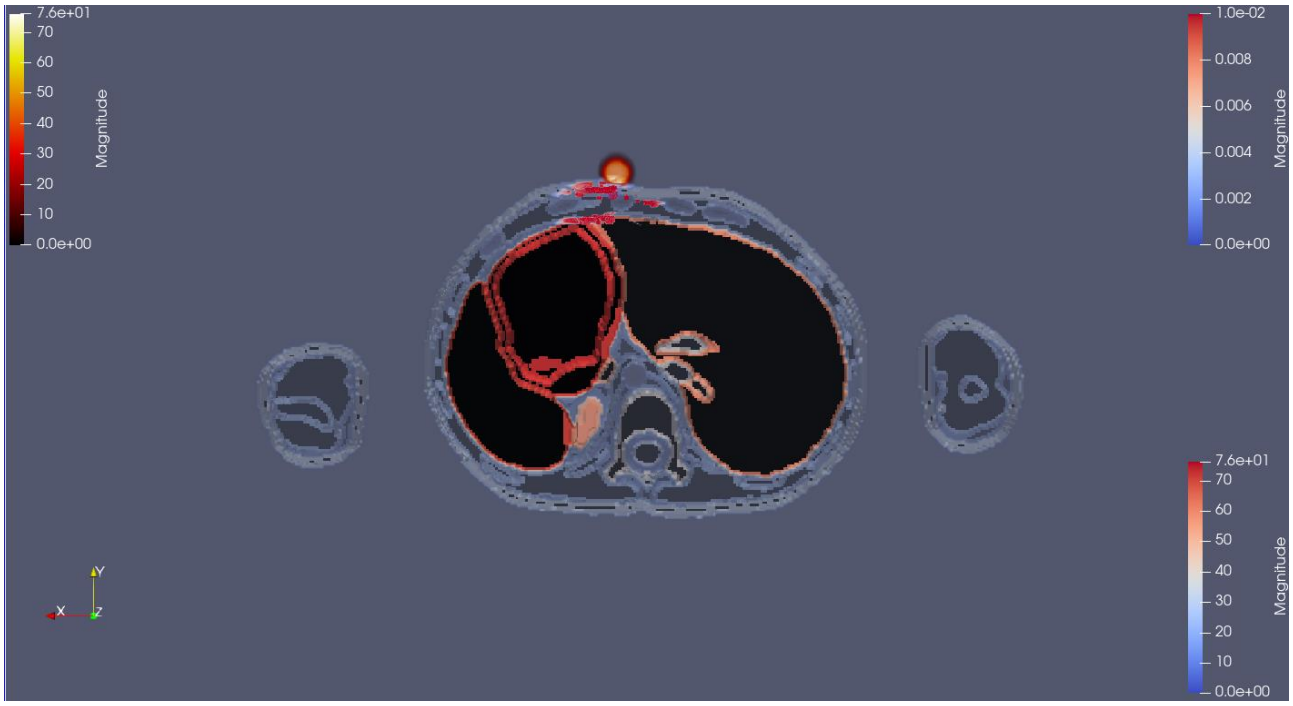

Figure 48: *Transversal slice of the thorax segment model simulation in standard visualization using "shade" mode*

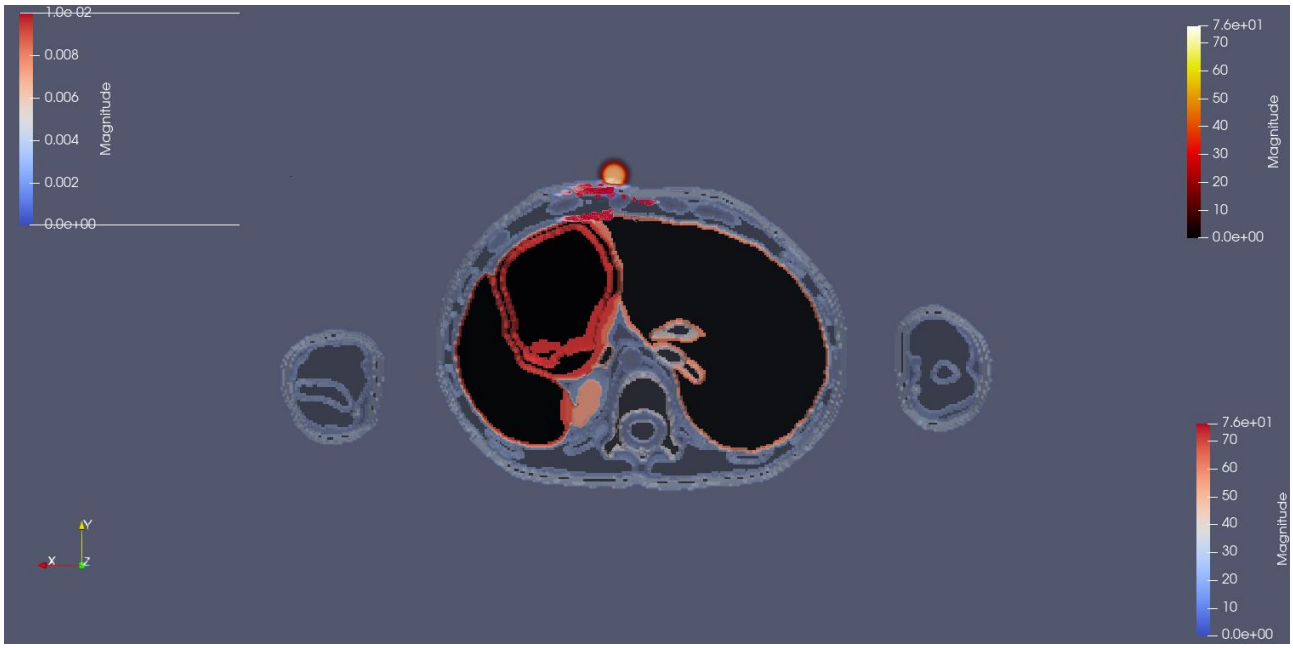

Figure 49: *Transversal slice of the whole-body model simulation. in standard visualization using "shade" mode*

In the following table are reported all the tissues names with the dielectric constant evaluated at a frequency of f = 2.45 GHz (Table 5). Moreover, in the last four columns are listed the number of present cells (occurrences) and the percentage of the power absorbed (P_abs) for each tissue.

Table 5: *Output of the simulation: number and name of the tissues, dielectric permittivity, and conductivity at 2.45 GHz. In the last columns are reported occurrence and absorbed power of the tissues for Chest model and Whole-body model.*

N°	**Tissues**	**ε_r**	**σ [S/m]**	**Occurrences** (Th. Chest)	**Occurrences** (Th. Body)	**P_abs [%]** (Th. Chest)	**P_abs [%]** (Th. Body)
00	External Air	1	0	22887215	88762950	N/C	N/C
01	Internal Air	1	1	0	48272	0	0
02	Blood	58.2636	2.54485	41558	70386	0.00110206	0.0015691
03	Blood Vessel Wall	42.5313	1.43534	1098	8497	$3.10961e^{-05}$	0.00052055
04	Brain (Grey Matter)	48.9115	1.80778	0	696143	0	0.00852496
05	Brain (White Matter)	36.1666	1.21499	0	367761	0	0.00260361
06	Cartilage	38.7702	1.75589	32372	43226	**6.26536**	**6.40419**
07	Cerebellum	44.8041	2.10148	0	151785	0	0.00020290
08	Cerebrospinal Fluid	66.2433	3.45785	19212	202358	$6.47636e^{-05}$	0.00505944
09	Connective Tissue	43.121	1.68474	0	283803	0	0.012116
10	Cartilage	38.7702	1.75589	0	3784	0	0.000125
11	Cartilage	38.7702	1.75589	0	11489	0	0.00039493
12	Esophagus	62.1584	2.21056	4044	6819	$6.26823e^{-05}$	$7.60425e^{-05}$
13	Esophagus Lumen	1	0	2546	3612	0	0
14	Eye (Vitrous Humor)	68.208	2.47809	0	9222	0	0.00121744
15	Eye (Lens)	33.9735	1.0869	0	292	0	$3.13097e^{-05}$

16	Fat	10.8205	0.267966	787150	2055491	0.323522	0.369981
17	Hippocampus	48.9115	1.80778	0	1982	0	$1.08543e^{-06}$
18	Hypophysis	57.2005	1.9679	0	279	0	$2.00854e^{-07}$
19	Hypothalamus	57.2005	1.9679	0	643	0	$2.3709\ e^{-07}$
20	Intervertebral Disc	38.7702	1.75589	64210	72897	0.00014169	0.00016701
21	Mandible	11.3809	0.394318	0	16645	0	0.00058375
22	Bone Marrow (Red)	10.3083	0.458834	0	108529	0	0.00120228
23	Midbrain	44.8041	2.10147	0	7577	0	$1.2212e^{-06}$
24	Muscle	52.7295	1.73879	2903115	6041403	**13.4452**	**14.6848**
25	Bone	11.3809	0.394318	356699	719312	0.00294505	0.00471636
26	Larynx	38.7702	1.75589	0	91	0	$7.79682e^{-06}$
27	Mucous Membrane	42.8526	1.59192	0	3087	0	0.00036828
28	Nerve	30.1454	1.08859	48069	58378	$2.03611e^{-05}$	$9.9861e^{-05}$
29	Pharynx	1	0	0	1433	0	0
30	Skin	38.0066	1.46404	483091	1342601	**62.4847**	**59.3743**
31	Skull	11.3809	0.394318	0	262595	0	0.00433279
32	Spinal Cord	30.1454	1.08859	16857	25855	$3.78151e^{-05}$	$2.29285e^{-05}$
33	SAT(Subcut. Fat)	10.8205	0.267966	816189	1880257	**6.78048**	**7.27791**
34	Tooth	11.3809	0.394318	0	5687	0	0.00036283
35	Tendon\Ligament	43.121	1.68474	25911	204561	$8.12497e^{-05}$	0.00082514
36	Thalamus	48.9115	1.80778	0	18809	0	$1.21452e^{-05}$
37	Tongue	52.6278	1.80266	0	37535	0	0.00285125
38	Trachea	39.7328	1.44881	680	4054	$1.19866e^{-05}$	0.00011407
39	Trachea Lumen	1	0	621	6095	0	0
40	Blood	58.2636	2.54485	32882	62770	0.00244499	0.00312148
41	Vertebrae	11.3809	0.394318	186924	231903	0.00013092	0.00016460
42	Pineal Body	57.2005	1.9679	0	276	0	$3.40815e^{-08}$
43	Pons	44.8041	2.10148	0	12257	0	$5.51064e^{-07}$
44	Medulla Oblangata	44.8041	2.10148	0	5272	0	$9.24698e^{-07}$
45	Eye (Cornea)	51.6149	2.29544	0	295	0	$5.8558e^{-05}$
46	Eye (Sclera)	52.6278	2.03319	0	3905	0	0.00036984
47	Commissura Anterior	36.1666	1.21499	0	40	0	$4.14701e^{-08}$
48	Commissura Posterior	36.1666	1.21499	0	6	0	$1.89906e^{-10}$
49	Urinary Bladder	18.0088	0.685329	29648	29648	0.00020911	$6.77689e^{-05}$
50	Bronchi	39.7328	1.44881	881	881	$3.82315e^{-05}$	$2.43832e^{-06}$
51	Bronchi lumen	1	0	735	735	0	0
52	Diaphragm	52.7295	1.73879	110796	110796	0.157793	0.141899
53	Adrenal Gland	57.2005	1.9676	0	2825	0.00010925	0.00012348
54	Epididymis	57.5508	2.1676	0	737	0	$9.81822e^{-06}$
55	Gallbladder	57.6337	2.05903	4260	7590	0.00024296	0.00024632
56	Heart Muscle	54.8139	2.25617	234581	234581	0.0718527	0.0853082
57	Heart Lumen	58.2636	2.54485	7562	7562	0.00027003	0.00039109
58	Kidney (Cortex)	52.7423	2.42957	80245	80245	0.00078295	0.00087751
59	Kidney (Medulla)	52.7423	2.42957	50348	50348	0.00019192	0.00021984
60	Large Intestine	5.8787	2.03839	210094	215402	0.0107947	0.00902407
61	Large Int. Lumen	52.7295	1.73879	478005	480164	0.0140816	0.00985761
62	Liver	43.0.45	1.68644	558131	558131	**5.83558**	**6.23474**
63	Lung	20.4769	0.804179	838209	907738	0.0244808	0.0301502
64	Meniscus	38.7702	1.75589	0	8782	0	$1.4581e^{-05}$
65	Pancreas	57.2005	1.9679	10604	10604	0.00652838	0.00761612
66	Patella	11.3809	0.394318	0	3085	0	$6.35288e^{-06}$
67	Penis	42.5313	1.43534	20	9125	$4.98637e^{-07}$	0.00026683
68	Prostate	57.5508	2.1676	1733	3486	$6.05038e^{-06}$	$9.37973e^{-06}$

69	Small Intestine	54.425	3.1732	56804	56804	0.0691768	0.0847942
70	Small Int. Lumen	52.7295	1.73879	22072	22072	0.00840625	0.010319
71	Spleen	52.4494	2.23807	122763	122763	0.00198136	0.00220302
72	Stomach	62.1584	2.21056	135732	135732	**2.66498**	**3.09959**
73	Stomach Lumen	52.7295	1.73879	130674	130674	**1.82391**	**2.11609**
74	Testis	57.5508	2.1676	0	3069	0	$7.07241e^{-05}$
75	Thymus	57.2005	1.9679	25926	28931	0.00239252	0.00310489
76	Ureter\Urethra	42.5313	1.43534	504	846	$2.65303e^{-06}$	$5.95212e^{-06}$

To study the variation of the power dissipation between body masses, the same simulation has been performed using Ella virtual model. Below are reported results for the second simulation with the monopole position in cell P(256, 215, 513). Moreover, since the device has been placed in different points of application, a table that reported the absorbed powers for three simulations has been created to evaluate the sensitivity to distance of the generated field and the power distribution. The three points of application are:

- Sim_E001: x= 256, y= 207 and z= 513
- Sim_E002: x= 256, y= 215 and z= 513
- Sim_E003: x= 256, y= 215 and z= 525

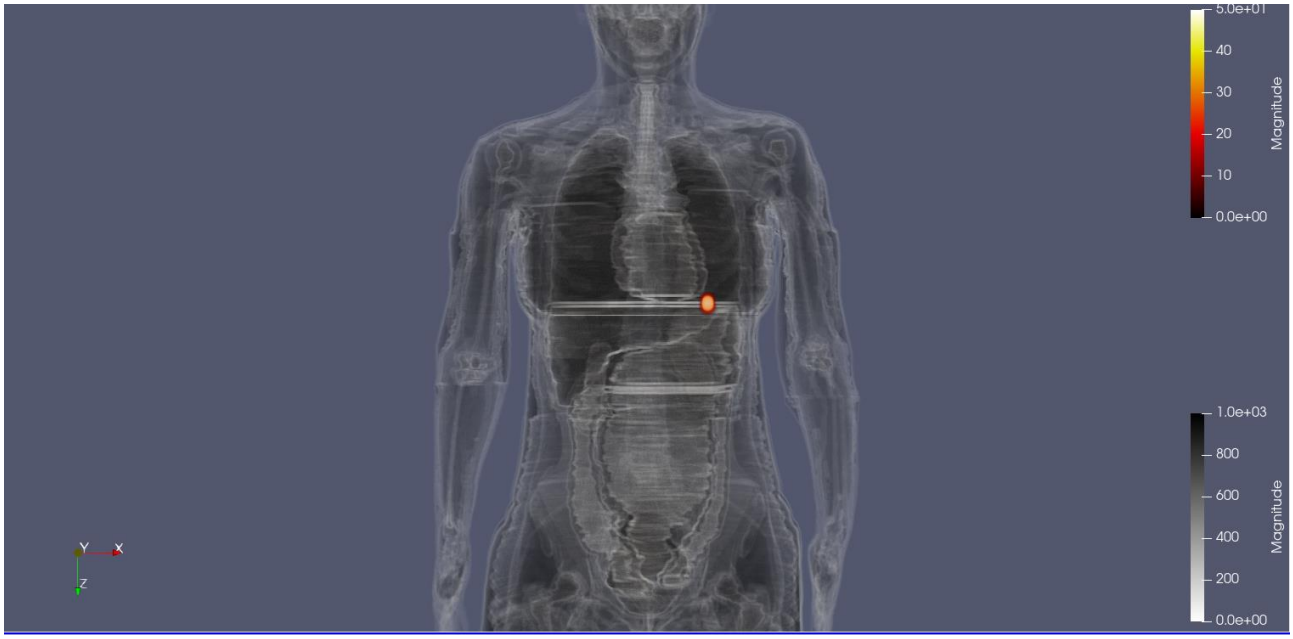

Figure 50: *X-ray visualization of the generated electric field magnitude of the embedded antenna: body colour range between [0 – 1000] in x-ray colour pre-set and "shade" option and generated field colour range between [0 – 50] in body-black radiation pre-set.*

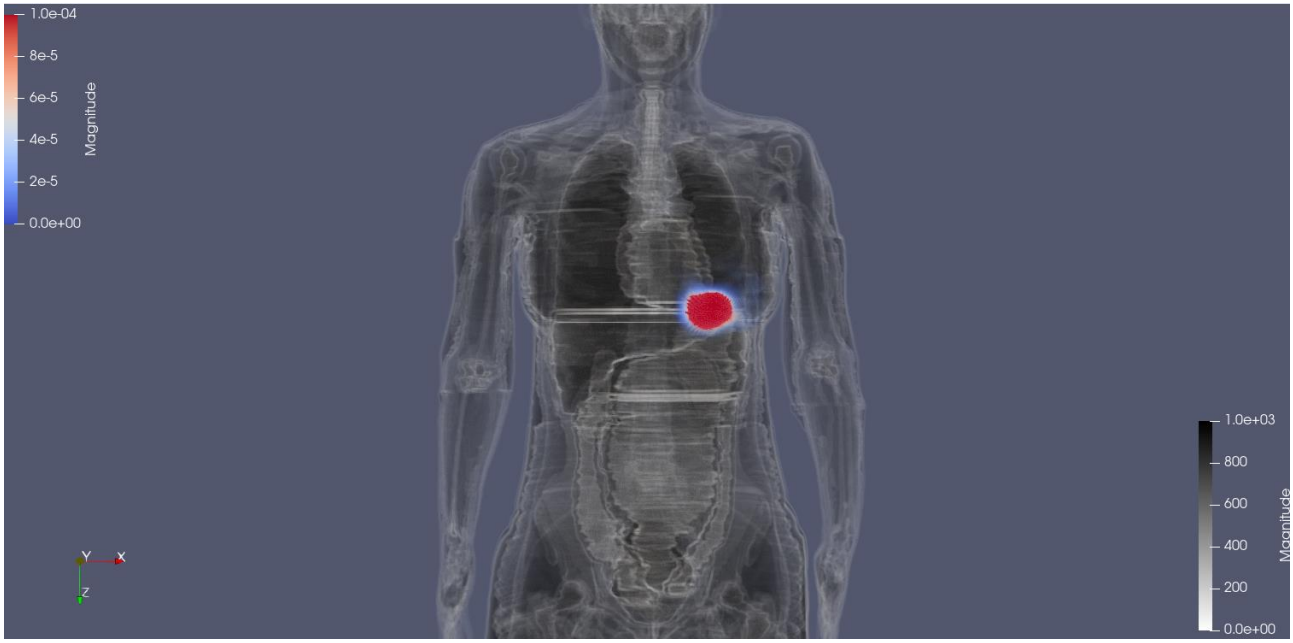

Figure 52: *SAR representation in x-ray scale colour: body colour range between [0 – 1000] in x-ray colour pre-set and "shade" option and SAR representation colour range between [0 - 0.0001] in standard colour pre-set*

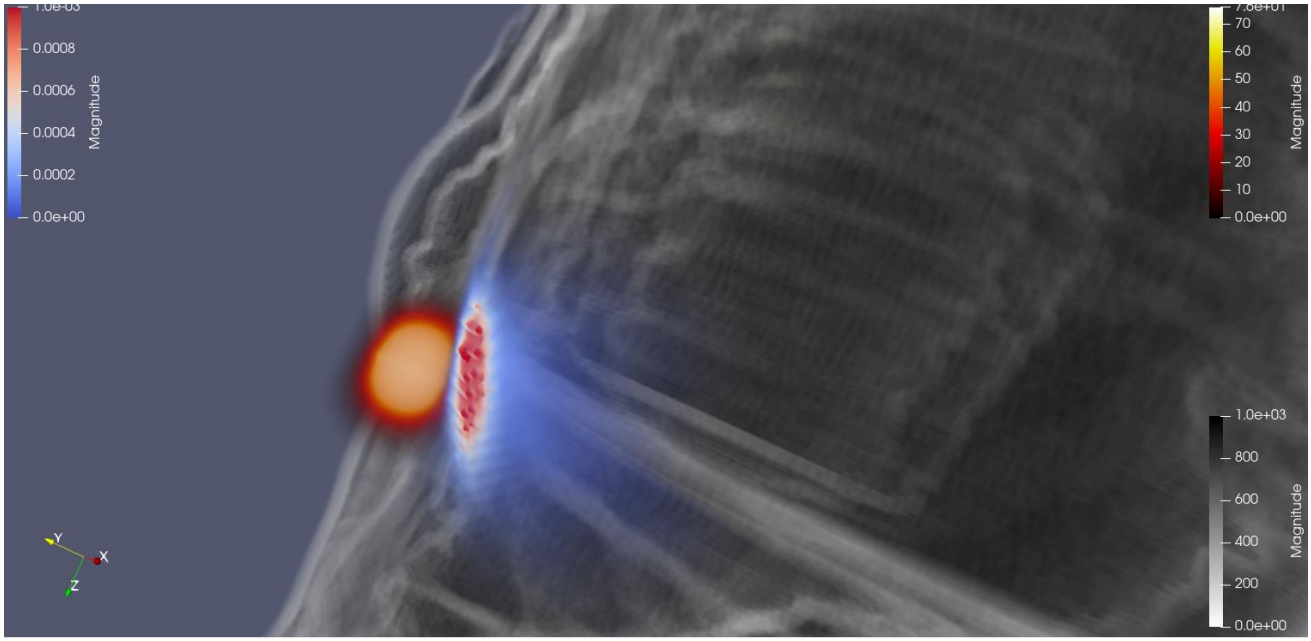

Figure 51: *Electric field magnitude and SAR representation in x-ray scale colour: body colour range between [0 – 1000] in x-ray colour pre-set and "shade" option, SAR colour range between [0 - 0.001] in standard pre-set and generated field colour range between [0 – 76] in body-black radiation pre-set.*

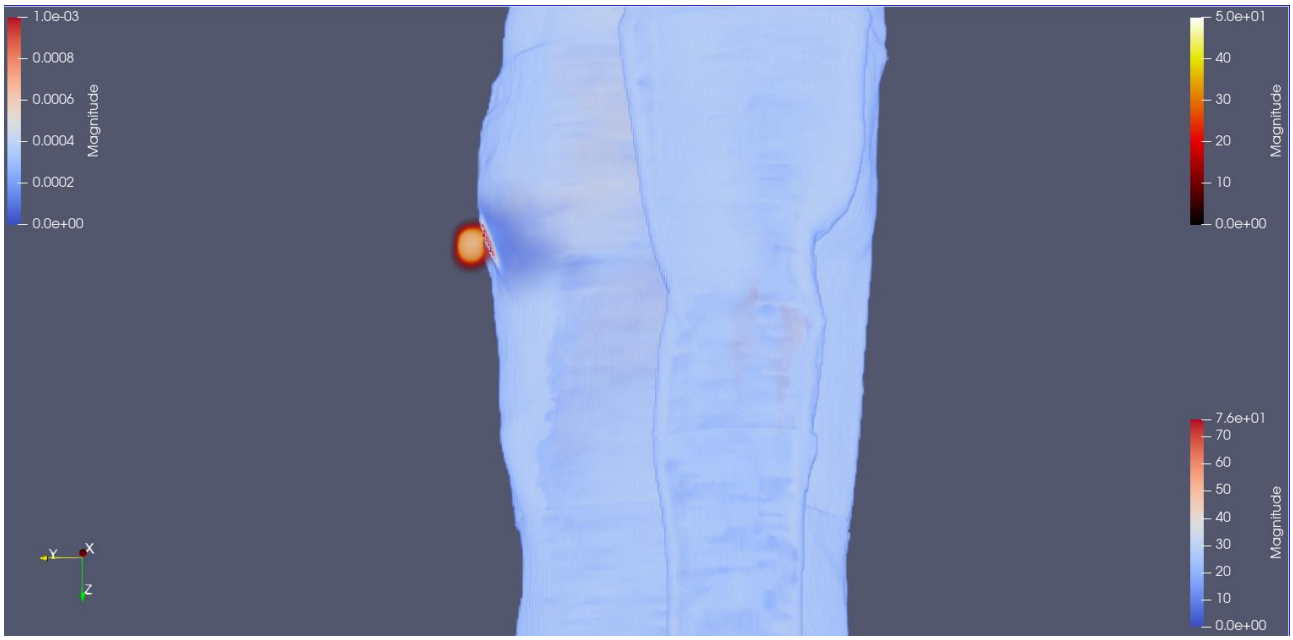

Figure 53: *Sagittal plane view of the electric field magnitude and SAR representation: body colour range between [0 – 76] in standard pre-set and "shade" option. SAR colour range between [0 - 0.001] in standard pre-set and generated field colour range between [0 – 50] in body-black radiation pre-set*

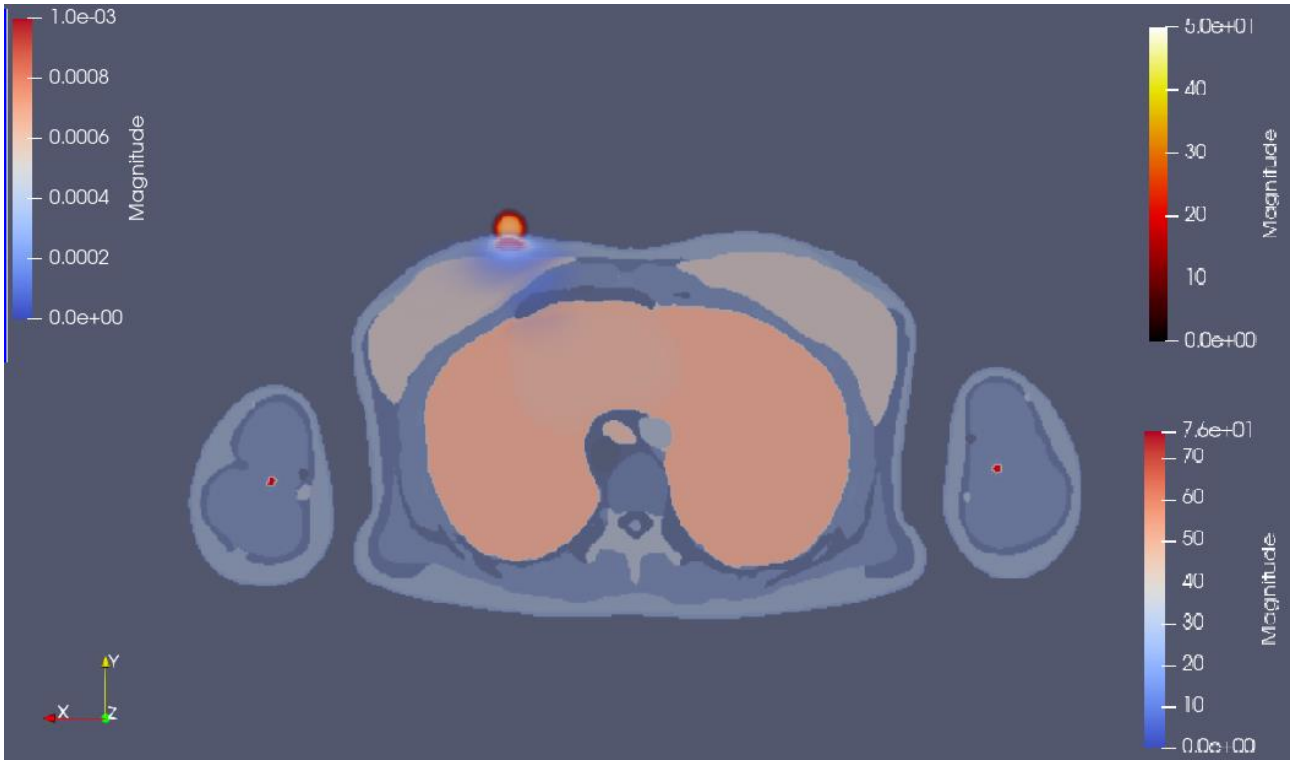

Figure 54: *Transversal slice of the body model in standard visualization:*

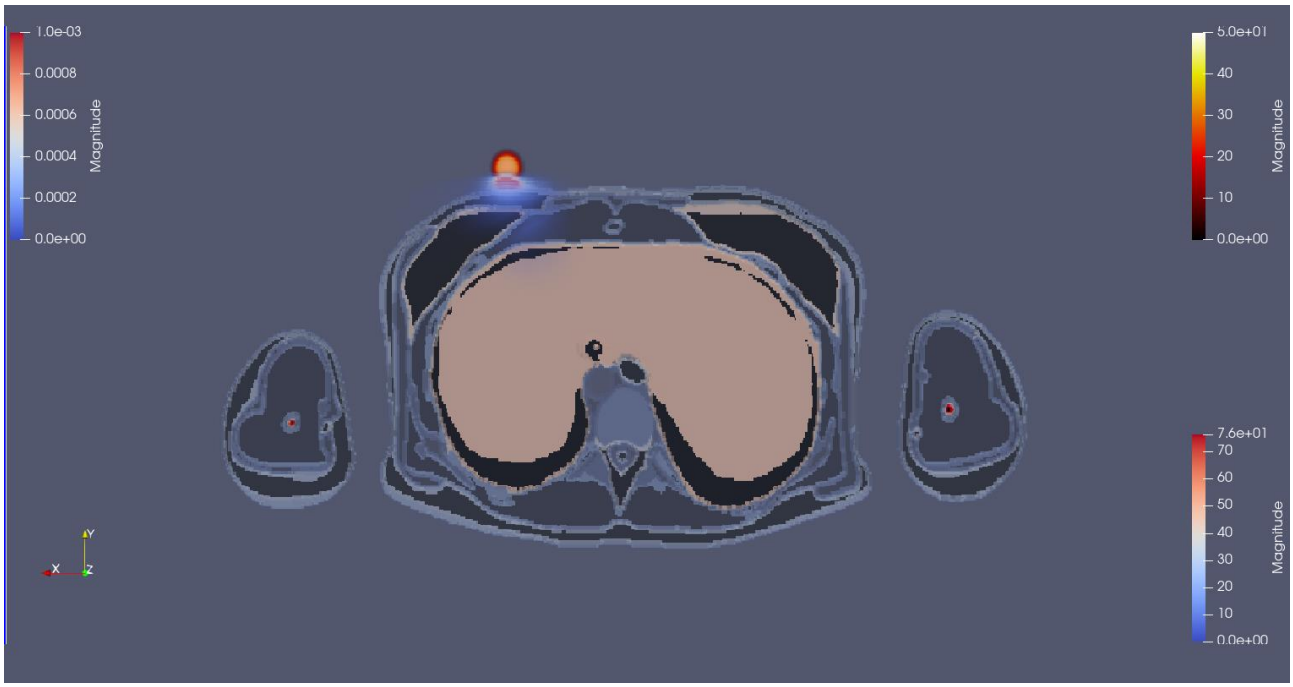

Figure 55: *Transversal slice of the body model in standard visualization using the "shade" option.*

Table 6: *Output of the simulation: number and name of the tissues and absorbed power for Sim_E001 Sim_E002 and Sim_E003*

N°	**Tissues**	**P_abs [%]** (Sim_E001)	**P_abs [%]** (Sim_E002)	**P_abs [%]** (Sim_E003)
09	Connective tissue	0.02	1.47	1.13
22	Muscle	0.21	16.37	23.31
27	Skin	98.15	33.34	28.91
30	SAT (Subcutaneous Fat)	1.34	26.64	25.60
43	Breast Fat	0.18	13.78	8.48
53	Liver	0.02	1.85	3.51

4. Discussions and conclusions

As it is possible to see from Figures 31 and 32, there is a very good matching between the load connected to the line and its characteristic impedance. Considering the return loss (Figure 31): a match is good if the return loss is high [55]. More specifically in the figure, is possible to see that the red and blue lines, which represent the result simulations where only the geometry is changed, reach values around six with an adaptation frequency of 1.9 GHz. A slight difference can be identified between the two curves; even if the geometry is more or less the same, there is a small worsening of the return loss and a bit increase of the adaptation frequency for the cropped geometry simulation. Decreasing the dielectric constant (Teflon) the return loss of the new geometry increased, reaching a value of 10 in all the ISM band centred at 2.45 GHz. Moreover, studying the reflected signal for the new geometry at frequencies not in the ISM band is possible to see that the antenna optimises at values near the frequency of adaptation since the sinusoid at 2.45 GHz (black line) seems to be characterized by a low reflection with respect to the other frequencies (Figure 32).
Also, in the 3D visualization of the electric field magnitude is possible to verify that the signal at the working frequency is not characterized by reflection, but the generated field is highly matched, especially near the ground and the transmission line connections (Figure 34 a and c). All the electric field is generated by the resonant part of the antenna which shows that the geometry and all the defined dimensions used in our simulation can be used to virtually represent our PCB.

However, the main simulation of the current work aims to study the electromagnetic characterization of the interaction between a real heart rate monitor and the human tissues. For this reason, the antenna and the virtual human models are simulated by FDTD, and their interaction is visualized in terms of distributed power (SAR W/kg) and electric field magnitude (V/m). As is possible to see (Figure 37-49) the antenna generates a hot spot of the electric field in the feeding point of the monopole, therefore the distributed power dissipates near this location reaching not so high depths in the body (Figure 39 and 40). From the x-ray representation, tissues that seem to absorb the majority of the power are the skin, the muscle, and the subcutaneous fat (SAT). In the same way, considering the percentage of the power absorbed by the tissues presented in Table 4, is possible to validate the visual analysis, since the higher values are reported for the skin, the muscle, and SAT. Moreover, also the cartilage and the tissue of the liver and stomach seems to dissipate a little part of power (Table 4) which can be explained by the position in which the device is located: both these two organs are localized in the upper portion of the abdominal cavity and are protected by the rib cage, joined by the costal cartilage to the sternum.

Even if the absorbed power on the skin or the muscle and the SAT seems to reach high percentage values, is important to consider that these quantities represent a small fraction of the power that is generated by the device (equal to 1 W in our simulations). In fact, of that power, 25% is reflected whereas the remaining quantity is dissipated in the surrounding tissues. Moreover, since the antenna of the HRM normally is not placed in contact with the body, the values of the dissipated power have to be considered lowered also due to the presence of dispersive materials between the devices and the body.

As it is possible to see, there is a visible difference in the power distribution between Ella and Thelonious, which indicates that the field and SAR strongly depend on the person's body shape and tissue distribution. Another important consideration concerns the points of application. Examining the results of Ella simulations (Table 6), where the device position is changed, there is a significant variation in the values of the absorbed power. This may suggest that the generated field and the distributed power are sensitive to the distance and therefore cannot be evaluated considering only one position. Indeed, a strategy to fully evaluate the electromagnetic interaction could be to perform several simulations in which the device position is shifted by small steps, in order to analyse this variation through statistical analysis.

Analysing the results of the two Thelonious simulations it is evident that they are analogous. This similarity is justified by the position of the device which is the same for both the simulations and by the field generated that does not bounce due to the truncation of the model. This can be a relevant factor in conditions of high computational effort, for computers that have to handle a large amount of data, since the computational costs can be lowered using a reduced torso map that can provide the same results obtained using whole-body models.

In conclusion, the field distribution and SAR values obtained through FDTD simulations are plausible and could be used to quantify the electromagnetic interaction of the real device under study.

Further studies could involve the use of a reverberation chamber to simulate a propagation environment and evaluate the exposure to a real physical antenna. Additional and more detailed studies could consider various exposure configurations, due to the strong dependence of the field distribution on the posture.

5. Bibliography

[1] K. S. Nikita, *Handbook of biomedical telemetry*. 2014.

[2] A. K. Lee, S. E. Hong, and H. Do Choi, "Is the SAM phantom conservative for SAR evaluation of all phone designs?," *ETRI J.*, vol. 41, no. 3, pp. 337–347, 2019

[3] C. Mc Caffrey, O. Chevalerias, C. O'Mathuna, and K. Twomey, "Swallowable-capsule technology," *IEEE Pervasive Comput.*, vol. 7, no. 1, pp. 23–29, 2008.

[4] P. Düking, S. Achtzehn, H. C. Holmberg, and B. Sperlich, "Integrated framework of load monitoring by a combination of smartphone applications, wearables and point-of-care testing provides feedback that allows individual responsive adjustments to activities of daily living," *Sensors (Switzerland)*, vol. 18, no. 5, pp. 1–11, 2018.

[5] G. E. Aviña, V. Newton, and C. Branda, "Real-time Data Collection through Wearable Devices to Quantify Attributes Related to Health and Performance in Extreme Conditions," pp. 2–4.

[6] S. J. Redmond *et al.*, "What Does Big Data Mean for Wearable Sensor Systems? Contribution of the IMIA Wearable Sensors in Healthcare WG," *Yearb. Med. Inform.*, vol. 9, pp. 135–142, 2014.

[7] H. W. Chow and C. C. Yang, "Accuracy of optical heart rate sensing technology in wearable fitness trackers for young and older adults: Validation and comparison study," *JMIR mHealth uHealth*, vol. 8, no. 4, 2020.

[8] J. M. Peake, G. Kerr, and J. P. Sullivan, "A critical review of consumer wearables, mobile applications, and equipment for providing biofeedback, monitoring stress, and sleep in physically active populations," *Front. Physiol.*, vol. 9, no. JUN, pp. 1–19, 2018.

[9] P. Düking, A. Hotho, H. C. Holmberg, F. K. Fuss, and B. Sperlich, "Comparison of non-invasive individual monitoring of the training and health of athletes with commercially available wearable technologies," *Front. Physiol.*, vol. 7, no. MAR, 2016.

[10] C. Perera, C. H. Liu, and S. Jayawardena, "The Emerging Internet of Things Marketplace from an Industrial Perspective: A Survey," *IEEE Trans. Emerg. Top. Comput.*, vol. 3, no. 4, pp. 585–598, 2015.

[11] J. Pan and W. J. Tompkins, "Pan Tomkins 1985 - QRS detection.pdf," *IEEE Trans. Biomed. Eng.*, vol. 32, no. 3, pp. 230–236, 1985.

[12] D. T. Weiler, S. O. Villajuan, L. Edkins, S. Cleary, and J. J. Saleem, "Wearable heart rate monitor technology accuracy in research: A comparative study between PPG and ECG

technology," *Proc. Hum. Factors Ergon. Soc.*, vol. 2017-Octob, pp. 1292–1296, 2017.

[13] D. J. Muggeridge *et al.*, "Measurement of heart rate using the polar OH1 and fitbit charge 3 wearable devices in healthy adults during light, moderate, vigorous, and sprint-based exercise: Validation study," *JMIR mHealth uHealth*, vol. 9, no. 3, 2021.

[14] S. Gillinov *et al.*, "Variable accuracy of wearable heart rate monitors during aerobic exercise," *Med. Sci. Sports Exerc.*, vol. 49, no. 8, pp. 1697–1703, 2017.

[15] T. Pattnayak and G. Thanikachalam, "AN91445 Antenna Design and RF Layout Guidelines," no. 001, pp. 1–60, 2014.

[16] A. Taflove and S. C. Hagness, "Computational Electrodynamics: The Finite-Difference Time-Domain Method, Third Edition," *Artech House*. p. 1038, 2005.

[17] C. A. Balanis, *Antenna Theory: Analysis and Design - 4th ed.* 2016.

[18] J. S. Seybold, *Introduction to RF Propagation*. 2005.

[19] Warren L. Stutzman and Gary A. Thiele, *Antenna Theory and Design - 2nd ed.* 2004.

[20] Kin-Lu Wong, "Planar Antennas for Wireless Communications." p. 157, 2003.

[21] N. Cohen, "Fractal antenna applications in wireless telecommunications," *Prof. Progr. Proc. Electron. Ind. Forum*, pp. 43–49, 1997.

[22] D. M. M. Khan, "Compact Planar Inverted F Antenna (PIFA) for Smart Wireless Body Sensor Networks," p. 8253, 2020.

[23] R. Waterhouse, *Printed Antennas for Wireless*. 2007.

[24] A. Dementyev, S. Hodges, S. Taylor, and J. Smith, "Power consumption analysis of Bluetooth Low Energy, ZigBee and ANT sensor nodes in a cyclic sleep scenario," *2013 IEEE Int. Wirel. Symp. IWS 2013*, pp. 2–5, 2013.

[25] K. S. Kunz and R. J. Luebbers, "The Finite Difference Time Domain Method for Electromagnetics," *The Finite Difference Time Domain Method for Electromagnetics*. 2018.

[26] J. Reddy, "Solutions manual for An introduction to the finite element method," *Essentials Finite Elem. Method*, p. 41, 2006.

[27] K. S. Yee, "Numerical Solution of Initial Boundary Value Problems Involving Maxwell's Equations in Isotropic Media," *IEEE Trans. Antennas Propag.*, vol. 14, no. 3, pp. 302–307, 1966.

[28] A. Taflove, "Application of the Finite-Difference Time-Domain Method to Sinusoidal Steady-State Electromagnetic-Penetration Problems," *IEEE Trans. Electromagn. Compat.*, vol. EMC-22, no. 3, pp. 191–202, 1980.

[29] J. B. Schneider, "Understanding the Finite-Difference Time-Domain Method," 2021.

[30] A. Taflove and S. C. Hagness, *The Finite-Difference Time-Domain Method Third Edition*.

2005.

[31] B. Jean-Pierre, “A perfectly matched layer for the absorption of electromagnetic waves,” *J. Comput. Phys.*, vol. 114, no. 2, pp. 185–200, 1994.

[32] V. E. Gusev, W. Lauriks, and J. Thoen, “Dispersion of nonlinearity, nonlinear dispersion, and absorption of sound in micro-inhomogeneous materials,” *J. Acoust. Soc. Am.*, vol. 103, no. 6, pp. 3216–3226, 1998.

[33] D. Uduwawala, “Gaussian vs differentiated gaussian as the input pulse for ground penetrating radar applications,” *ICIIS 2007 - 2nd Int. Conf. Ind. Inf. Syst. 2007, Conf. Proc.*, vol. 2, no. August, pp. 199–202, 2007.

[34] M. Stabin, “Nuclear medicine dosimetry,” *Phys. Med. Biol.*, vol. 51, no. 13, 2006.

[35] J. Wiart, A. Hadjem, M. F. Wong, and I. Bloch, “Analysis of RF exposure in the head tissues of children and adults,” *Phys. Med. Biol.*, vol. 53, no. 13, pp. 3681–3695, 2008.

[36] I. G. Zubal, C. R. Harrell, E. O. Smith, Z. Rattner, and G. Gindi, “Computerized three-dimensional segmented human anatomy,” *Med. Phys.*, vol. 21, no. 2, pp. 299–302, 1994.

[37] J. Sühnel and H. Berg, *Biological Effects of Electromagnetic Fields (Mechanisms, Modeling, Biological Effects, Therapeutic Effects, International Standards, Exposure Criteria)*, vol. 61, no. 1–2. 2003.

[38] R. Habash, “Biological effects of electromagnetic fields,” *Eng. Electromagn. Appl.*, vol. 416, pp. 189–210, 2006.

[39] K. B. Baker *et al.*, “Evaluation of specific absorption rate as a dosimeter of MRI-related implant heating,” *J. Magn. Reson. Imaging*, vol. 20, no. 2, pp. 315–320, 2004.

[40] C. K. Chou *et al.*, “Radio frequency electromagnetic exposure: Tutorial review on experimental dosimetry,” *Bioelectromagnetics*, vol. 17, no. 3, pp. 195–208, 1996.

[41] K. Guido and A. Kiourti, “Wireless Wearables and Implants: A Dosimetry Review,” *Bioelectromagnetics*, vol. 41, no. 1, pp. 3–20, 2020.

[42] G. Ziegelberger *et al.*, “Principles for non-ionizing radiation protection,” *Health Phys.*, vol. 118, no. 5, pp. 477–482, 2020.

[43] A. Ahlbom *et al.*, “Guidelines for limiting exposure to time-varying electric, magnetic, and electromagnetic fields (up to 300 GHz),” *Health Phys.*, vol. 74, no. 4, pp. 494–521, 1998.

[44] Federal Communication Commission, “Specific Absorption Rate (SAR) For Cell Phones: What It Means For You,” *Fed. Commun. Comm.*, pp. 1–2, 2019.

[45] N. A. and R. A. Office of the Federal Register, “86 FR 20456 - Human Exposure to Radiofrequency Electromagnetic Fields and Reassessment of FCC Radiofrequency Exposure Limits and Policies,” vol. 86, no. 74. pp. 20456–20458, 2021.

[46] C. Gabriel, S. Gabriel, and E. Corthout, “The dielectric properties of biological tissues: III. Parametric models for the dielectric spectrum of tissues,” *Phys. Med. Biol.*, vol. 41, no. 11, pp. 2271–2294, 2000.

[47] S. Gabriel, R. W. Lau, and C. Gabriel, “The dielectric properties of biological tissues: III. Parametric models for the dielectric spectrum of tissues,” *Phys. Med. Biol.*, vol. 41, no. 11, pp. 2271–2293, 1996.

[48] N. Musa, M. Y. Onimisi, and J. T. Ikyumbur, “Frequency and Temperature Dependence of Ethanol Using the Cole-Cole Relaxation Model,” *Am. J. Condens. Matter Phys.*, vol. 10(2), no. December, pp. 44–49, 2020.

[49] A. K. Lee, S. E. Hong, and H. Do Choi, “Numerical compliance testing of human exposure electromagnetic radiation from smart-watches,” *ETRI J.*, vol. 41, no. 3, pp. 337–347, 2019.

[50] K. Moreland, “The ParaView Tutorial,” 2014.

[51] K. Moreland *et al.*, “ParaView Getting Started Guide,” *Sandia Natl. Lab.*, pp. 0–66, 2015.

[52] B. Device, “Garmin HRM-Dual^{TM},” no. August, pp. 2018–2019, 2019.

[53] A. Pcr and L. Kit, “FR408HR Data Sheet,” vol. 31402, no. September 2004, pp. 0–1, 2012.

[54] Smith Metal Centres, “Technical Datasheet Low Friction , Chemical Resistant , Engineering Plastic Typical Applications PTFE (Polytetrafluoroethylene),” p. 16, 2017.

[55] T. S. Bird, “Definition and misuse of return loss,” *IEEE Antennas Propag. Mag.*, vol. 51, no. 2, pp. 166–167, 2009.

Acknowledgments

I would like to dedicate this space to those who have contributed directly and indirectly to the production of this thesis, the final result of my university career.

A special thanks go to my Supervisor Prof. Franco Moglie and Co-Supervisor Prof. Valter Mariani Primiani who made this work possible. Thank you for your constant help during my research internship and for reviewing the present manuscript. I would like also to acknowledge the Partnership for Advanced Computing in Europe (PRACE) for awarding access to Joliot-Curie KNL at GENCI@CEA, France.

Special thanks to my family and all my friends for supporting me over these years.